

UC Riverside

UC Riverside Electronic Theses and Dissertations

Title

Mapping Spatially Resolved Star Formation, Metallicity and Dust Across Galaxy Populations Over Cosmic Time

Permalink

<https://escholarship.org/uc/item/73w288x8>

Author

Jafariyazani, Marziye

Publication Date

2021

Copyright Information

This work is made available under the terms of a Creative Commons Attribution-NoDerivatives License, available at <https://creativecommons.org/licenses/by-nd/4.0/>

Peer reviewed|Thesis/dissertation

UNIVERSITY OF CALIFORNIA
RIVERSIDE

Mapping Spatially Resolved Star Formation, Metallicity and Dust Across Galaxy
Populations Over Cosmic Time

A Dissertation submitted in partial satisfaction
of the requirements for the degree of

Doctor of Philosophy

in

Physics

by

Marziye Jafariyazani

June 2021

Dissertation Committee:

Dr. Bahram Mobasher, Chairperson
Dr. Andrew B. Newman
Dr. Brian Siana

Copyright by
Marziye Jafariyazani
2021

The Dissertation of Marziye Jafariyazani is approved:

Committee Chairperson

University of California, Riverside

Acknowledgments

I am grateful to my advisor, Bahram Mobasher without his continuous advice and valuable insights, I could not accomplish this thesis. He always pushed me to seek the bests, achieve more and motivates me to never give up. I am also extremely thankful for all the opportunities he offered me. I learned from his community services a lot, and I am always amazed by his dedication to educate and inspire next generations.

I am so thankful to my co-advisor, Andrew B. Newman who advised my research in the last two years of my grad school. I owe so much to him for his always support, passion and dedication. The way that he looks at the problems always amazed me, and I learned from him everyday. I am extremely grateful for the opportunity I had to work with him.

I have a special thanks for Brian Siana who served on my dissertation committee. His insights and great questions always lead to new ideas for me. Another special thanks for Shoubaneh Hemmati who helped me with patience in my first project when I had little research experience. I also want to thank and recognize the dedication of faculties in our department who offered excellent courses and taught them with great passion, and also for all of our enlightening conversations: Laura Sales, Gillian Wilson, Gabriela Canalizo, Frederick Hamann, George Becker and Barry Barish.

I can never thank my family, my parents (Davood & Masoumeh) and my little brother (MohammadMahdi), enough for their endless love, support and encouragement. Although my choice of graduate school made us thousands of kilometers away from each other, thanks to video-calling applications, we were able to see each other every single day and have our usual everyday conversations just like before. I am sincerely grateful to my

husband, Rasoul, for his always kindness, not to mention when he chose remote working just to let me go to grad school in-person. It is lovely that we can create lots of memories together everyday. My extended family, my grandma, aunts and uncle, also always sent me love and support.

I cannot finish without mentioning my sincere thanks to all of my friends from high school, college, and grad school who made my life brighter and more exciting: Fatemeh, Motahare, Somayeh, Reyhaneh, Hoda, Arezoo, Alireza, Fahimeh, Mohsen, Maryam, Yasin, Amin, MohammadAmin, Amanda, Ali Ahmad, Najmeh and Anahita.

Lastly, I want to thank all astronomers and staffs at Carnegie Observatories who hosted me with great friendliness in the last 2 years which I performed part of my thesis research at this institution.

Chapter 3 and 4 of this thesis was supported through generous Carnegie-UCR fellowship funded by Carnegie Observatories and University of California, Riverside for which I am extremely grateful for.

Part of the data presented in chapter 3 & 4 were obtained at the W. M. Keck Observatory at Maunakea. I wish to recognize and acknowledge the very significant cultural role and reverence that the summit of Maunakea has always had within the indigenous Hawaiian community. I am most fortunate to have the opportunity to conduct observations from this mountain. Also, Part of the data in chapter 2 is based on observations taken by the MUSE-Wide Survey as part of the MUSE Consortium.

The results of Chapter 2 and 3 of this thesis have been published in the following manuscripts:

[1] Marziye Jafariyazani, Bahram Mobasher, Shoubaneh Hemmati, Tara Fetherolf, Ali Ahmad Khostovan, Nima Chartab: “Spatially resolved properties of galaxies from CANDELS+MUSE: radial extinction profile and insights on quenching”, *The Astrophysical Journal*, Volume 887, Issue 2 (2019)

[2] Marziye Jafariyazani, Andrew B. Newman, Bahram Mobasher, Sirio Belli, Richard S. Ellis, Shannon G. Patel: “Resolved Multi-element Stellar Chemical Abundances in the Brightest Quiescent Galaxy at $z \sim 2$ ”, *The Astrophysical Journal Letters*, Volume 897, Issue 2 (2020)

To my parents, Davood Jafari Yazani & Masoumeh Abdi for their endless support
and encouragement, and to my Grandmother, Tavoos Imanpour.

ABSTRACT OF THE DISSERTATION

Mapping Spatially Resolved Star Formation, Metallicity and Dust Across Galaxy Populations Over Cosmic Time

by

Marziye Jafariyazani

Doctor of Philosophy, Graduate Program in Physics
University of California, Riverside, June 2021
Dr. Bahram Mobasher, Chairperson

In this thesis, I study the integrated and spatially resolved (kilo-parsec scale) properties of star-forming and quiescent galaxies across cosmic time to understand their evolution. First, using a sample of star-forming galaxies at intermediate redshifts ($0.1 < z < 0.42$) selected from the MUSE Wide Survey, I investigate the spatial distribution of $H\alpha$ star formation rate (SFR) and the Balmer decrement using data from MUSE integral field spectrograph. For the same galaxies, I derive spatially resolved mass, SFR and dust maps from pixel-by-pixel Spectral Energy Distribution (SED) fitting on multiband photometric data from the Cosmic Assembly Near-infrared Deep Extragalactic Legacy Survey (CANDELS) taken with the Hubble Space Telescope. I find strong dependence of the radial profiles of both stellar and nebular color excesses on the integrated specific SFR of star-forming galaxies. My results support the inside-out scenario for the growth of these galaxies. Next, I investigate the chemical abundances and star formation histories of high-redshift quiescent galaxies. My sample consists of five unique gravitationally lensed galaxies at $1.95 < z < 2.64$ which includes MRG-M0138, the brightest lensed quiescent galaxy detected in the near in-

frared wavelengths. This is the only sample of quiescent galaxies at $z \sim 2$ for which we have a precise measure of stellar abundances as well as spatially resolved measurements, made possible due to strong gravitational lensing. I first analyze spectra of MRG-M0138 to measure magnesium-enhancement $[\text{Mg}/\text{Fe}]$ (only the second precise $[\text{Mg}/\text{Fe}]$ measurement at $z \sim 2$), iron abundance $[\text{Fe}/\text{H}]$ and, for the first time, their spatial gradient, as well as the stellar abundances of 6 other elements using full spectral fitting. I finally present my analysis of the other four galaxies in this sample where in addition to investigating their chemical abundances, I study their star formation histories reconstructed by fitting synthetic models to their multi-band photometric and spectroscopic data. I show these galaxies have significant Mg-enhancement which cannot be explained solely by short formation timescale as proposed by simple chemical evolution models, then I discuss new scenarios to explain chemical abundances in these galaxies.

Contents

List of Figures	xii
List of Tables	xxi
1 Introduction	1
2 Spatially Resolved Properties of Galaxies from CANDELS+MUSE: Radial Extinction Profile and Insights on Quenching	7
2.1 Introduction	7
2.2 Sample selection	10
2.2.1 CANDELS	11
2.2.2 MUSE-Wide Survey	11
2.2.3 Final sample	12
2.3 Measurement of resolved properties	14
2.3.1 Resolved photometric measurements	14
2.3.2 Resolved spectroscopic measurements	15
2.3.3 Three sample galaxies with resolved measurements	17
2.4 Results	20
2.4.1 Integrated SFR diagnostics	20
2.4.2 Radial profiles of mass, SFR and sSFR	21
2.4.3 Extinction profiles	27
2.4.4 Resolved SFR- M_* and sSFR- M_* relations	32
2.5 Summary	34
3 Resolved Multi-element Stellar Chemical Abundances in the Brightest Quiescent Galaxy at $z \sim 2$	36
3.1 Introduction	36
3.2 Data	40
3.3 Full spectral fitting	41
3.4 Results	43
3.4.1 Comparison to COSMOS-11494 and local massive ETGs	45
3.4.2 Stellar Age and Abundance Gradients	49

3.4.3	Evidence for an Interstellar Medium	50
3.5	Discussion	53
4	The stellar populations and star formation histories of quiescent galaxies at $z \sim 2$	57
4.1	Introduction	57
4.2	Data	60
4.3	Chemical abundances	63
4.4	Stellar Population Gradients	69
4.5	Star Formation Histories	75
4.6	Discussion	79
5	Conclusions	81
5.1	Spatially resolved properties of star-forming galaxies	81
5.2	High- z quiescent galaxies	84
	Bibliography	88

List of Figures

1.1	The cosmic star formation history measured from rest-frame far-UV and infrared data (Madau and Dickinson 2014).	3
1.2	Stellar abundances for a quiescent galaxy at $z = 2.1$ (black filled circle) and massive quiescent galaxies at $z \sim 1.4$ (colored symbols) compared to local early-type galaxies (plusses) and stacks of quiescent galaxies at $0.07 < z < 0.7$ (gray squares). Figure is adopted from Kriek et al. 2019.	5
2.1	My sample of 32 galaxies with MUSE detection of $H\alpha$ and $H\beta$ lines over plotted on the galaxies from the CANDELS survey at the same redshift range: $0.1 < z < 0.42$. Black dashed line is representing the main sequence of star-forming galaxies from Lee et al. 2015 for galaxies at $z \sim 0.35$. Galaxies of this sample are color-coded according to their redshift.	13
2.2	Total SFR of galaxies measured by summing up the SFRs per pixel vs. SFR measured from the integrated emission lines. Red data points are $SFR_{H\alpha}$ and black ones are dust-corrected $SFR_{H\alpha}$. Dashed line represents one-to-one relationship.	18

2.3	From left to right: spatially resolved stellar mass surface density, SFR surface density, stellar $E(B-V)$, $H\alpha$ emission and $H\beta$ emission maps for three galaxies from my sample. To allow for visually comparing <i>HST</i> and MUSE PSF, resolved SED-fitting maps (first three in each row) have <i>HST</i> quality where input seven images of SED-fitting were PSF matched to the resolution in F160W, and $H\alpha$ and $H\beta$ maps which are derived from 3D datacubes provided by MUSE-Wide Survey have their original PSF.	19
2.4	Radial profile of nebular to stellar color excess (black dashed lines) overplotted on sSFR profile (grey dotted lines) for 3 sample galaxies which their nebular $E(B-V)$ to stellar $E(B-V)$ ratio profiles closely follow their sSFR profiles. The mass, SFR, stellar $E(B-V)$, $H\alpha$ and $H\beta$ maps for these three galaxies are presented in Figure 2.3 (the top panel of figure 2.3 is corresponding to left panel of this graph).	20
2.5	Comparison between the $SFR_{H\alpha}$ and SFR_{SED} for the integrated light of galaxies. Gray dotted line represents the one-to-one relationship. Blue dashed line represents the best fit to the data with the slope = 0.819 ± 0.232 , and intercept = -0.919 ± 0.152	22
2.6	Median radial profile of Σ_{SFR} for all the galaxies in the sample. Red and black profiles represent the $SFR_{H\alpha}$, and the dust-corrected $SFR_{H\alpha}$, respectively. Shaded regions correspond to 1σ error in the data.	24

2.7	Median radial sSFR profiles for galaxies in the sample. Solid black profile presents the SED-derived sSFR and the solid blue profile shows the sSFRs calculated by dividing the dust-corrected $\text{SFR}_{\text{H}\alpha}$ by the SED-derived stellar mass in each annulus. In both profiles, shaded regions represent 1σ error in the data.	26
2.8	Median radial profiles of nebular and stellar color excess for galaxies in the sample. I divided the sample into two bins based on their integrated sSFR such that the number of galaxies in two bins are about the same. Galaxies in the left panel have integrated $\text{sSFR} < 1.25 \text{ Gyr}^{-1}$, and galaxies in the right panel have integrated $\text{sSFR} > 1.25 \text{ Gyr}^{-1}$. In each panel, red and blue profiles present the stellar and nebular color excess, respectively. In all profiles, shaded regions represent 1σ scatter in the data. In the right panel, the dotted lines correspond to the best fit model to the data where the stellar reddening is modeled with a linear relation and nebular profile is fitted by a power-law.	30

2.9	Resolved main sequence and resolved sSFR- M_* relations for galaxies in my sample. Gray data points represent individual annuli in galaxies. Two top panels are presenting resolved main sequence with two different SFR diagnostics. Left panel is based on SFR_{SED} and right panel is based on dust-corrected $SFR_{H\alpha}$. Bottom panels present sSFR- M_* relation with sSFR $_{SED}$ on the left and dust-corrected sSFR $_{H\alpha}$ on the right. Solid gray lines are the best linear fits to grey data points with the fitted parameters presented in Table 2.1. Colored pentagons are the median SFR/sSFR (top/bottom panels) in bins of stellar mass which are color-coded by the average distance from the center of the galaxies.	31
3.1	The upper right panel presents <i>HST</i> observations of the two brightest images of MRG-M0138 along with the placement of the slit on each image (reproduced from Newman et al. 2018b). Other panels show the integrated spectra of these two images observed with Keck/MOSFIRE (purple, Image 1 in the upper right panel) and Magellan/FIRE (light blue, Image 2) in J, H, and K bands. The best-fit model to each spectrum is shown in solid black or blue. Grey shaded regions are masked in the spectral fitting process. For display purposes, all spectra are smoothed to 370 km s^{-1} by taking the inverse variance weighted mean.	39

3.2	<p>Corner plot showing covariances among age, $[\text{Fe}/\text{H}]$, and the abundances of elements for which $[\text{X}/\text{Fe}]$ is measured to < 0.1 dex precision in the MOSFIRE spectrum. Black contours show results from fitting the MOSFIRE spectrum, and blue contours correspond to fitting the FIRE spectrum, which has lower S/N. These contours correspond to 1σ, 2σ and 3σ levels. Titles show the median of the marginalized posteriors obtained from the MOSFIRE spectrum</p>	42
3.3	<p>$[\text{X}/\text{Fe}]$ for different elements derived for MRG-M0138 and stacked spectra of SDSS early-type galaxies. Black diamonds represents values for MRG-M0138 derived from the MOSFIRE spectrum, and blue hexagons correspond to the FIRE spectrum. Each colored solid line represents local ETGs with a specific velocity dispersion, σ, as indicated in the legend. Abundances of most of the elements increase with increasing σ. Interestingly, $[\text{Mg}/\text{Fe}]$ is significantly higher in MRG-M0138 than is typical of local galaxies, even those with the highest σ.</p>	44

3.4	<p>Relationships among stellar mass, $[\text{Mg}/\text{Fe}]$, and $[\text{Fe}/\text{H}]$ for MRG-M0138 (black and blue diamonds, corresponding to the MOSFIRE and FIRE measurements), COSMOS-11494 at $z = 2.1$ (green circle; Kriek et al. 2016), and the centers of local massive ETGs (light blue circles; Greene et al. 2019). Red pentagons show measurements derived from the SDSS stacks of Conroy et al. 2014. The solid line in the upper left panel shows the scaling relation from Thomas et al. 2005. The $z \sim 2$ galaxies are distinct from each other and from the centers of local massive ETGs in the $[\text{Mg}/\text{Fe}]$ vs. $[\text{Fe}/\text{H}]$ plane (lower panel). A simple chemical evolution model (dot-dashed line) from Kriek et al. 2016 could plausibly explain the abundances of COSMOS-11494 with a very short formation timescale, but this model cannot account for the high $[\text{Mg}/\text{Fe}]$ and $[\text{Fe}/\text{H}]$ of MRG-M0138.</p>	46
3.5	<p>Spatially resolved age, $[\text{Mg}/\text{Fe}]$ and $[\text{Fe}/\text{H}]$ for MRG-M0138. The flux-weighted radius in each spatial bin is indicated as R/R_e. Black dotted lines represent the measured value from the integrated spectra. Solid blue line represents the fit to the resolved data in the form of $A \times \log (R/R_e) + B$, where A and B are presented in each panel. I find that age and $[\text{Mg}/\text{Fe}]$ are uniform over $0.5 - 1.4R_e$, while I detect a marginally negative gradient in $[\text{Fe}/\text{H}]$.</p>	51

3.6	Resolved spectra of MRG-M0138 in seven bins observed with Keck/MOSFIRE (grey lines) and the best-fit model to each spectrum which are shown in red. Extraction aperture (R) for each bin is specified in arcsec along the slit relative to the position of peak flux. For display purposes, all spectra are smoothed to 370 km s^{-1} by taking the inverse variance weighted mean. . .	52
4.1	Composite <i>HST</i> images of the four galaxies in the sample. The lensed quiescent galaxies are shown in boxes. MRG-M0150 has multiple images which are numbered. The images are adopted from Newman et al. 2018a.	60
4.2	Abundance patterns of high- z quiescent galaxies compared to local counterparts. Top left: [Fe/H] versus velocity dispersion (σ), top right: [Mg/Fe] versus velocity dispersion, lower left: [Mg/Fe] versus [Fe/H]. High- z quiescent galaxy sample include 4 galaxies from this work: MRG-M2129 (blue square), MRG-S1522 (maroon pentagon), MRG-M0918 (purple diamond) and MRG-M0150 (yellow-thin diamond, with only [Fe/H] measured due to lack of Mg-line in its spectrum), two galaxies from the literature: MRG-M0138 (black circle; Jafariyazani et al. 2020) and COSMOS-11494 (green filled-x; Kriek et al. 2016). Local sample include local ETGs from Conroy and van Dokkum 2012 (green stars), stacks of SDSS ETGs (red pluses; Conroy et al. 2014) and centers of local MASSIVE ETGs (light purple circles; Greene et al. 2019). .	65

4.3	Stellar population gradients for MRG-P0918. Red dash-dotted lines are based on the integrated spectra, and red dotted lines represent their 1σ errorbar. Physical radius cannot be measured for this galaxy due to lack of lens model. There is no detectable gradient in age, [Mg/Fe] and [Fe/H] in this galaxy.	66
4.4	Stellar population gradients for MRG-M0150 and MRG-M2129. Red dash-dotted lines are based on the integrated spectra, and red dotted lines represent their 1σ errorbar. Solid black lines and their surrounding shaded regions are the fit to the resolved data in the form of $A \times \log (R/R_e) + B$, where A and B are presented in each panel. Both galaxies show a relatively flat age and [Mg/Fe] gradients and a negative [Fe/H] gradient.	67
4.5	Reconstructed star formation history for MRG-M0138. Best-fit SFH model as well as the 68% and 95% Bayesian credible intervals derived from posterior distributions are presented. SFRs are demagnified by a factor of 12.5, derived from its constructed lens model.	70
4.6	Reconstructed star formation history for MRG-M0150. Best-fit SFH model as well as the 68% and 95% Bayesian credible intervals derived from posterior distributions are presented. SFRs are demagnified by a factor of 4.4, derived from its constructed lens model.	71
4.7	Reconstructed star formation history for MRG-M2129. Best-fit SFH model as well as the 68% and 95% Bayesian credible intervals derived from posterior distributions are presented. SFRs are demagnified by a factor of 4.4, derived from its constructed lens model.	72

4.8	Reconstructed star formation history for MRG-P0918. Best-fit SFH model as well as the 68% and 95% Bayesian credible intervals derived from posterior distributions are presented. SFRs are demagnified by a fiducial magnification factor of 4 due to lack of lens model.	73
4.9	Reconstructed star formation history for MRG-S1522. Best-fit SFH model as well as the 68% and 95% Bayesian credible intervals derived from posterior distributions are presented. SFRs are demagnified by a fiducial magnification factor of 4 due to lack of lens model.	74
4.10	Reconstructed star formation histories of all galaxies in the sample. All SFRs are demagnified as described in above figures.	75
4.11	Metallicity and Mg-abundance versus star-formation timescale which is defined as the duration of time in which the a galaxy increases its stellar mass from 10% to 90% of its total mass ($t_{90\%} - t_{10\%}$). The grey line represents Thomas et al. 2005 relation between $[\alpha/\text{Fe}]$ and formation timescale. I acknowledge that these two formation timescales are not exactly similar as Thomas et al. 2005 reported the width of Gaussian star formation histories as formation timescale.	78

List of Tables

2.1	Best fit values to the resolved SFR- M_* and sSFR- M_* relations	33
4.1	Available photometric data for galaxies in my sample. Total fluxes for MRG-M0150 are normalized to its Image 1. Data are adopted from Newman et al. 2018a.	61
4.2	Spectroscopic observation information for galaxies in my sample, adopted from Newman et al. 2018a. Spectrum of MRG-M0150 is from its Image 1. .	62
4.3	Photometric data for MRG-M0138. Total fluxes are normalized to its Image 1. Data are adopted from Newman et al. 2018a.	63
4.4	Age, [Mg/Fe] and [Fe/H] derived from alf	64

Chapter 1

Introduction

Galaxy formation is a multi-scale and multi parameter problem and despite many advancements in the field, there are still some fundamental questions that remain unanswered. One series of science questions that are particularly interesting and motivated this thesis are: What processes are responsible for transforming blue star-forming galaxies to red quiescent systems? What are the imprints of these processes on the spatially resolved scales of galaxies? How metals and dust are distributed in galaxies and how they affect the growth of these systems?

In the past few decades, wealth of data from imaging and spectroscopic surveys across the electromagnetic spectrum as well as many advanced theoretical and modeling tools attempted to answer these questions. These efforts led to a consistent picture of the cosmic star formation history which the star formation rate per unit volume has increased after the Big Bang, peaked approximately when the age of the universe was about 3.5 Gyr, and then declined exponentially at later times (see Madau and Dickinson 2014 for a

comprehensive review). This is nicely summarized in Figure 1.1 adopted from the same paper.

However, we are still lacking data and comprehensive explanatory models to draw a detailed picture of this evolution. One limitation is that most observational measurements and therefore models are based on integrated light of the galaxies due to the resolution limit of current instruments, so our understanding from internal processes in galaxies are very limited especially for more distant objects. However, resolved studies of local galaxies, including the Milky Way, show complex distribution of stars, gas and dust throughout galaxies (e.g., Sánchez et al. 2012; Dalcanton et al. 2012; Bundy et al. 2015). Therefore, studying the internal processes of individual galaxies at kilo-parsec scales seems crucial to have a comprehensive picture of galaxy formation and evolution processes. Moreover, there is not enough constraint even at integrated scales for more compact and fainter galaxies, for example for high redshift (z) quiescent systems.

In the first part of this thesis (Chapter 2), I investigate the distribution of star formation rate (SFR), specific SFR (sSFR), and dust attenuation across individual galaxies for a sample of 32 galaxies selected from the MUSE-Wide Survey (Herenz et al. 2017) at $0.1 < z < 0.42$. In this analysis, I take advantage of the high spatial resolution of the MUSE integral-field spectrograph to measure reliable spatially resolved $H\alpha$ and $H\beta$ emission line maps for individual galaxies. I also derive resolved stellar mass, SFR and dust maps using pixel-by-pixel Spectral Energy Distribution (SED) fitting on high resolution multi-band *HST*/ACS and *HST*/WFC3 data from the Cosmic Assembly Near-infrared Deep Extragalactic Legacy Survey (CANDELS, Grogin et al. 2011; Koekemoer et al. 2011).

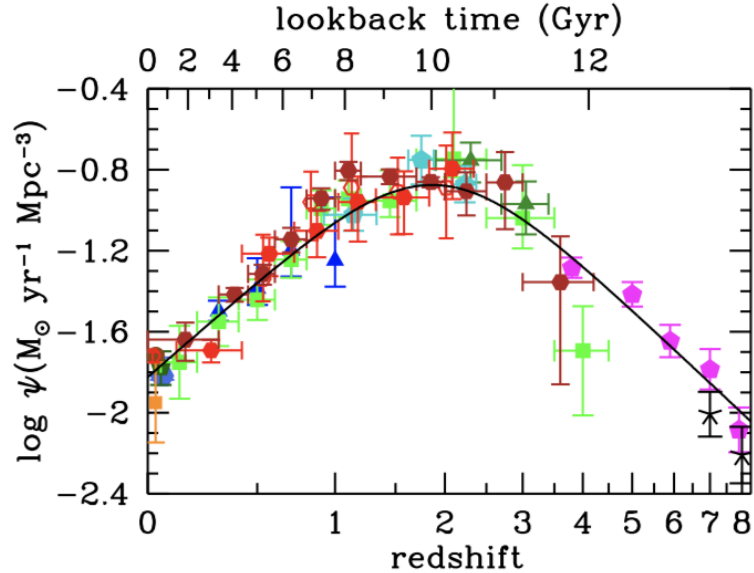


Figure 1.1: The cosmic star formation history measured from rest-frame far-UV and infrared data (Madau and Dickinson 2014).

By combining these, I analyze the radial profile of various physical parameters across these galaxies to understand how mass, star formation activity and color excess profiles are related. This will tell us about the timescale of the star formation and possible growth models for these galaxies.

In the second part of my thesis, I focus on high-redshift quiescent systems which their evolutionary path is not yet well explained. This is crucial to understand the causes of star formation quenching at cosmic noon when most galaxies were experiencing the peak of their star formation activity. Also, these rare objects are close to their epoch of quenching when the majority of merger activities had not yet occurred to pollute their stellar population. Therefore, they provide us with a perfect lab to test the physics of star formation and quenching which is needed for drawing a robust picture of growth of galaxies.

One powerful method to understand the growth of these galaxies is by measuring their stellar chemical compositions. However, such measurements are extremely challenging for quiescent galaxies at high redshifts, because they have faint stellar continua and compact sizes, making it difficult to detect absorption lines and nearly impossible to spatially resolve them. Before this thesis, there was only one quiescent galaxy at $z \sim 2$ for which integrated stellar abundances (e.g., iron, magnesium) were measured precisely (~ 0.1 dex precision, Kriek et al. 2016), and there were only a handful of galaxies with such measurements at $z \sim 1.4$ (Kriek et al. 2019). These are shown in Figure 1.2 (adopted from Kriek et al. 2019) which highlights how few data point we have from stellar abundances of high- z quiescent galaxies which are needed to understand this population.

In this context, powerful cosmic telescopes, strong gravitational lensing systems, offer us the opportunity to overcome some of these limitations, and enable us to study these galaxies with detailed spectroscopy that can be spatially resolved to investigate their internal structures. In the third chapter of this thesis, I analyze deep spectra of MRG-M0138, a lensed quiescent galaxy at $z = 1.98$ which is the brightest of its kind at this redshift range, with an H-band magnitude of 17.1. Taking advantage of full spectral fitting, I measure magnesium and iron abundance and, for the first time, the stellar abundances of 6 other elements in this galaxy. I further constrained, also for the first time in a $z \sim 2$ galaxy, radial gradients in stellar age, magnesium abundance and iron abundance. My measurements show a very unusual chemical abundances for MRG-M0138 even compared to the centers of local massive early-type galaxies which are believed to be descendants of this population. This observation challenges simple galactic chemical evolution models and shows the need for

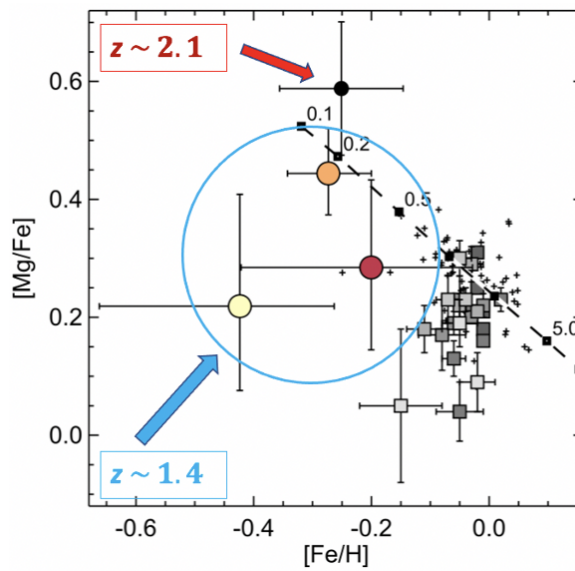


Figure 1.2: Stellar abundances for a quiescent galaxy at $z = 2.1$ (black filled circle) and massive quiescent galaxies at $z \sim 1.4$ (colored symbols) compared to local early-type galaxies (plusses) and stacks of quiescent galaxies at $0.07 < z < 0.7$ (gray squares). Figure is adopted from Kriek et al. 2019.

more observations and elaborate models. This motivated the analysis of the next chapter of this thesis (chapter 4) to understand if this galaxy is representative of high redshift quiescent galaxy populations, what other constraint we can put on their evolution processes using other probes, and what models are needed to explain their evolution.

In chapter 4, I study four other high- z gravitationally lensed quiescent galaxies at $1.95 < z < 2.64$. Besides investigating their chemical abundances at integrated and spatially resolved scales, I examine their evolutionary path by another independent probe which is their star formation histories reconstructed by fitting stellar population synthesis models to their multi-band photometric and spectroscopic data.

I conclude this thesis by a summary followed by ongoing projects and possible future directions in Chapter 5.

Chapter 2

Spatially Resolved Properties of Galaxies from CANDELS+MUSE: Radial Extinction Profile and Insights on Quenching

2.1 Introduction

Over the past decades, great deal of work has been done to understand the physical properties of galaxies over a wide range of cosmic time. However, most of these studies are based on measurements of the integrated light of galaxies and most information about the behavior of galaxies at small scales (kpc level) are ignored. Resolved studies of local galaxies, including the Milky Way, show complex distributions of metallicities, stars, gas, dust, and

star formation activity (e.g., Sánchez et al. 2012; Dalcanton et al. 2012; Bundy et al. 2015). This suggests that to draw a comprehensive picture of how galaxies evolve, what processes are involved, and how such processes occur requires that we study galaxies at high spatial resolution scales to understand the internal mechanisms that drive the underlying galaxy’s evolution.

A relatively inexpensive and accurate method, widely used to measure physical parameters for large samples of galaxies, is to fit their Spectral Energy Distribution (SED) using multi-waveband photometric data. The shape of the SED of a galaxy depends on all physical properties including the star-formation history, metal content, dust properties, interstellar medium (ISM) properties, etc. Therefore by fitting stellar population models to observed SEDs, we can extract these parameters (see Conroy 2013 for a review on SED modeling). This method is recently extended to measure these properties at the resolution element of galaxies, providing pixel-by-pixel estimates and therefore, high resolution maps (e.g., Wuyts et al. 2012a; Hemmati et al. 2014; Guo et al. 2018). However, relying solely on SED-derived parameters is problematic due to potential degeneracies and uncertainties associated with the SED-fitting process. Stellar mass is known to be the most reliable output from SED-fitting, since it is measured by the normalization of the SED, while properties such as star formation rates (SFR), color excess, age, etc. rely on a wide range of assumptions. For instance, SED-derived SFR is highly degenerate with age, dust, and metallicity and is dependent on the assumed star formation history (SFH) and initial mass function (IMF) (Conroy 2013). Furthermore, physical properties should be derived from independent methods rather than deriving all from SED-fitting to properly study their correlations

with each other without being worried about model-dependent correlations. Hence, using spectroscopic information besides photometry seems to be required to break degeneracies and obtain more robust results.

Another challenge in measuring physical properties of galaxies, both at integrated and resolved scales, is estimating the effect of dust on the measured properties. It is known that SED color excess is seriously affected by age - dust - metallicity degeneracy, and it only measures reddening toward the stellar light which can be different from reddening toward nebular emission lines (Calzetti 1997). This different level of attenuation toward nebular and stellar regions is explained to some extent by two-component dust model proposed by Charlot and Fall 2000. In this model, old stars which are distributed all over the galaxies become redder due to the attenuation only from the diffuse interstellar medium (ISM), while young, short-lived massive stars formed in cold molecular clouds tend to ionize their surrounding regions, and are subject to attenuation from ionized gas as well. Therefore, it is important to measure both forms of reddening not only to correct their effect on other physical parameters, but also to better understand the geometry of stars and dust inside galaxies. This also requires spectroscopy to directly measure diagnostic lines sensitive to extinction (i.e. Balmer decrement: $H\alpha/H\beta$) to estimate the attenuation toward nebular regions.

In recent years, spatially-resolved spectroscopy of local galaxies became feasible thanks to the integral field spectroscopy (IFS) surveys, such as SAMI (Croom et al. 2012; Scott et al. 2018), CALIFA (Sánchez et al. 2012), and MaNGA (Bundy et al. 2015). For this work, I needed IFS data in a field with available high spatial resolution multi-waveband

photometry, so I take advantage of MUSE-Wide Survey (Urrutia et al. 2019a) which also allowed us to go further than previous studies by examining the resolved properties of galaxies at lower masses and higher redshifts. I focus on studying radial profiles of SFR, sSFR and dust attenuation in a sample of 32 galaxies with high S/N detection of $H\alpha$ and $H\beta$ at $0.1 < z < 0.42$ and average stellar mass of $10^{8.71} M_{\odot}$. The aim is to evaluate the effect of dust on measured properties, study the radial gradient in nebular and stellar reddening, and constrain quenching mechanisms based on radial profile of the SFR and sSFR for this sample.

The chapter is organized as follows. In §2 I present the sample and its selection criteria. §3 provides my methodology in analyzing the photometric and spectroscopic data from the Cosmic Assembly Near-infrared Deep Extragalactic Legacy Survey (CANDELS) and MUSE-Wide Survey respectively at kpc scale. I discuss my results from resolved analysis of SFR, sSFR and dust distribution in galaxies in §4. In §5 I summarize the main points of this work and discusses future directions.

Throughout this chapter, I adopt a cosmology with a matter density parameter $\Omega_M = 0.3$, a cosmological constant $\Omega_{\Lambda} = 0.7$ and a Hubble constant of $H_0 = 70 \text{ kms}^{-1}\text{Mpc}^{-1}$. All magnitudes are in the AB system.

2.2 Sample selection

Accurate measurement of the physical properties of galaxies at kpc-scales requires a sample with high-spatial resolution multi-waveband photometry and integral field spectroscopy. With extensive dataset currently available for galaxies in the GOODS-South field,

this provides an ideal sample as it combines the deepest and highest resolution multi-band *HST* data from the CANDELS survey with integral field spectroscopic data of high spectral and spatial resolution from the MUSE-Wide Survey. In this section I briefly explain the two parent samples followed by my sample selection strategy.

2.2.1 CANDELS

CANDELS (Grogin et al. 2011; Koekemoer et al. 2011) is the largest single project carried out by the Hubble Space Telescope (*HST*), with 902 orbits of observing time. CANDELS consists of five fields (GOODS-South, GOODS-North, EGS, UDS, COSMOS) with the optical imaging data from the Advanced Camera for Surveys (ACS) and infrared data from Wide Field Camera 3 (WFC3). The catalog is selected in WFC3 H-band (F160W) and contains 18000 galaxies to a 5σ limiting magnitude of ~ 27 . *HST* images, multi-wavelength photometric catalogs and catalogs of integrated physical properties for CANDELS galaxies are now available in all five fields (for details see, Guo et al. 2013, Galametz et al. 2013; Mobasher et al. 2015; Nayyeri et al. 2017; Stefanon et al. 2017).

2.2.2 MUSE-Wide Survey

MUSE-Wide Survey is a blind 3D spectroscopic survey of sub-areas in the CANDELS-DEEP and CANDELS-COSMOS regions with 1-hour exposure time per 1 arcmin² pointing. It has been done using the the MUSE instrument on the Very Large Telescope (VLT) in the wide field mode, which provides medium resolution spectroscopy at a spatial sampling of 0.2'' per spatial pixel. The extended wavelength range was used, covering 4750-9350 Å, with ~ 2.5 Å resolution. The final survey will cover 100 fields each covering an area of 1

arcmin². This analysis uses data from 24 MUSE fields in the GOODS-S deep area (Herenz et al. 2017). The data from these fields provided the preprocessed datacubes for a total of 831 emission line galaxies with redshifts in the range $0.04 < z < 6$.

2.2.3 Final sample

The main goal of this work is to measure the kpc scale distribution of SFR, sSFR, and dust in galaxies and relate them to the integrated physical properties. Recent star formation activity is measured using H α emission line, and dust distribution is estimated from Balmer decrement (H α /H β) which provides a measure of the extinction correction. Therefore, I select the sample such that H α and H β emission lines both fall in the observed wavelength range covered by the spectrograph to enable measurements of both lines simultaneously. This restricts the redshift range of the sample to $0.1 < z < 0.42$. Finally, I omit galaxies for which their H α and/or H β lines could not be fitted properly due to low S/N or being at the edge of the field of view, such that the whole galaxy was not covered. Only 32 galaxies (out of a sample of 831) satisfy my selection criteria with the stellar mass spanning the range $10^{7.7}$ to $10^{10.3} M_{\odot}$ and average mass of $10^{8.71} M_{\odot}$.

Figure 2.1 shows my final sample on the SFR- M_{*} relation, compared to all the galaxies observed in the CANDELS GOODS-S field at the same redshift range ($0.1 < z < 0.42$) which shows the properties of the galaxies in this sample compared to the overall population of galaxies at this redshift range. Stellar mass and SFR in this plot are derived from SED-fitting with details explained in section 3.1. The dashed black line represents the main sequence of star-forming galaxies at $z \sim 0.35$ from Lee et al. 2015. These galaxies are typically towards the upper part of the “main sequence”, suggesting we are looking at the

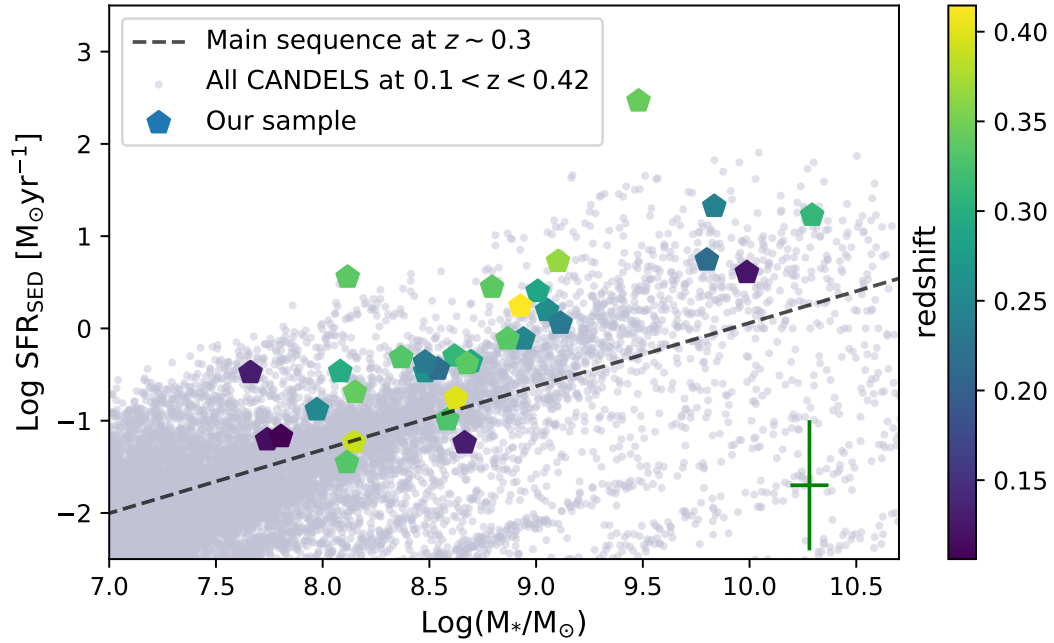


Figure 2.1: My sample of 32 galaxies with MUSE detection of $\text{H}\alpha$ and $\text{H}\beta$ lines over plotted on the galaxies from the CANDELS survey at the same redshift range: $0.1 < z < 0.42$. Black dashed line is representing the main sequence of star-forming galaxies from Lee et al. 2015 for galaxies at $z \sim 0.35$. Galaxies of this sample are color-coded according to their redshift.

more active population of star-forming galaxies which is expected on $\text{H}\alpha$ selected samples (e.g. Nelson et al. 2016; Emami et al. 2019). Despite small sample size, the galaxies in this study cover ~ 3 orders of magnitude in stellar mass.

2.3 Measurement of resolved properties

2.3.1 Resolved photometric measurements

In this section I describe techniques in measuring resolved photometric properties of galaxies. Following Hemmati et al. 2014, I perform pixel-by-pixel SED fitting using *HST* imaging data in seven pass bands. The *HST* imaging data consist of four optical bands from the ACS (F435W, F606W, F775W, and F850LP) and three near-infrared bands from WFC3 (F105W, F125W, and F160W) from the CANDELS GOODS-S survey. An automated pipeline is developed to perform high spatial resolution measurements. First I make a 100×100 pixel cutout around each source and produce a segmentation map of that galaxy. The goal of the segmentation map, is to simply define edges for the galaxy with 0 and 1 values for pixels not corresponding and corresponding to the galaxy respectively. Multiplying the segmentation map to each of the cutouts removes the surrounding objects and background pixels. I then perform PSF matching to degrade HST images to the MUSE resolution (~ 1.1 arcsec) at $H\alpha$ wavelength. A multi-waveband catalog is then generated for each galaxy with each row corresponding to a resolution element with magnitudes in seven pass bands and their associated RMS errors. The spectroscopic redshift for each galaxy is also listed.

Model SEDs are generated covering a wide range in parameter space. The model template library includes SEDs for stars from the PICKLES library (Pickles 1998), AGN and normal galaxies. For quasars, I use synthetic and composite quasar libraries available in the LePhare package (Arnouts et al. 1999; Ilbert et al. 2006), and for galaxies I build a unique and inclusive library using Bruzual and Charlot 2003 stellar population synthe-

sis models. I assume a Chabrier 2003 initial mass function, exponentially declining star formation histories with τ in the range 0.05 to 20 Gyr, and the metallicity to be 40% Solar.

SED-fitting on the resolved elements is then performed using the LePhare SED-fitting code, which finds the closest match from the model templates to the observed SED corresponding to each resolution element based on χ^2 minimization. The redshifts are fixed to their spectroscopic values to fit for the physical parameters including stellar mass, SFR, and extinction. LePhare code enables us to add the contribution of emission lines including Ly α , H α , H β , [OII], [OIII]4959, and [OIII]5007 based on Kennicutt relations (Kennicutt 1998) and incorporate Calzetti dust attenuation law (Calzetti et al. 2000). Figure 2.3 shows resolved stellar mass and SFR surface density as well as stellar E(B–V) maps for three sample galaxies. For visualization purposes, these maps show results of resolved SED-fitting on *HST* quality data where images from seven photometric bands were PSF matched to the resolution in F160W. Overall the observed trends are not affected by degrading the *HST* images to MUSE resolution.

2.3.2 Resolved spectroscopic measurements

Spatially resolved spectroscopic measurements are performed using data products from the MUSE-Wide Survey. I use 3D reduced datacubes for all galaxies in the sample with their detailed reduction procedure presented in Herenz et al. 2017. To produce emission line maps, I first fit the stellar continuum with a low-order polynomial and subtract it from each spaxel. Then the emission line fluxes are measured by fitting the spectra by a Gaussian, weighted by the variances of the spectrum for every spaxel. In measuring the integrated emission line fluxes, I do not account for any possible effect by kinematics due to both the

relatively low stellar masses and the exclusion of inclined galaxies (axial ratio $b/a < 0.5$) from the sample.

Using emission line maps, I then measure $H\alpha/H\beta$ to estimate the effect of dust. From quantum physics, we know that the flux ratio of two nebular Balmer emission lines is constant for a fixed electron temperature, and deviation from the theoretical value can be due to the dust extinction. I measure Balmer decrement pixel-by-pixel for the spaxels where both $H\alpha$ and $H\beta$ have $S/N > 3$ to produce a reliable map for each galaxy. In this process, pixels which have an observed value of $F(H\alpha)/F(H\beta) < 2.86$, which is the theoretical threshold for Case B recombination at $T = 10000$ K in the absence of dust (Osterbrock 1989), are assigned zero extinction.

$SFR_{H\alpha}$ is computed using calibration from Kennicutt 1998 for individual pixels, and to be consistent with my SFR_{SED} measurements, I adjusted them to account for my SED-fitting assumptions compared to Kennicutt 1998 assumptions: Chabrier 2003 IMF instead of Salpeter 1955 IMF, and 40% Solar metallicity instead of Solar. Balmer color excess, $E(H\beta-H\alpha)$, is computed following Equation 2.1 using Balmer decrement maps. Then $A(H\alpha)$, attenuation toward HII regions, is measured for each pixel following Equation 2.2. In this Equation, $k(H\alpha)$ and $k(H\beta)$ are the amount of extinction at the $H\alpha$ and $H\beta$ wavelengths, assuming a Calzetti et al. 2000 dust attenuation law. Finally, SFRs per pixel are corrected for extinction using Balmer decrement.

$$E(H\beta - H\alpha) = 2.5 \log_{10} \frac{(H\alpha/H\beta)_{obs}}{2.86} \quad (2.1)$$

$$A(H\alpha) = \frac{E(H\beta - H\alpha)}{k(H\beta) - k(H\alpha)} \times k(H\alpha) \quad (2.2)$$

As a sanity check, I examined if SFR computed from the integrated emission line of the galaxies are equivalent to the sum of the SFRs of their pixels, as shown in Figure 2.2 for the case of observed and dust-corrected $\text{SFR}_{H\alpha}$. I find that the measurements are in good agreement such that both independent approaches are consistent. The only concern is that incorporating lower signal to noise $H\beta$ measurements significantly increased the error bars and scatter between the two SFRs.

2.3.3 Three sample galaxies with resolved measurements

For visualization purposes, I bring spatially resolved mass, SFR, stellar $E(B-V)$, $H\alpha$ and $H\beta$ maps for three sample galaxies in Figure 2.3, following by their radial profile of nebular to stellar $E(B-V)$ and sSFR in Figure 2.4. These maps are examples of how distribution of physical properties can be so diverse and non-Gaussian, and allow visual inspection of how resolved structures of galaxies affecting the radial profile of sSFR and nebular to stellar reddening.

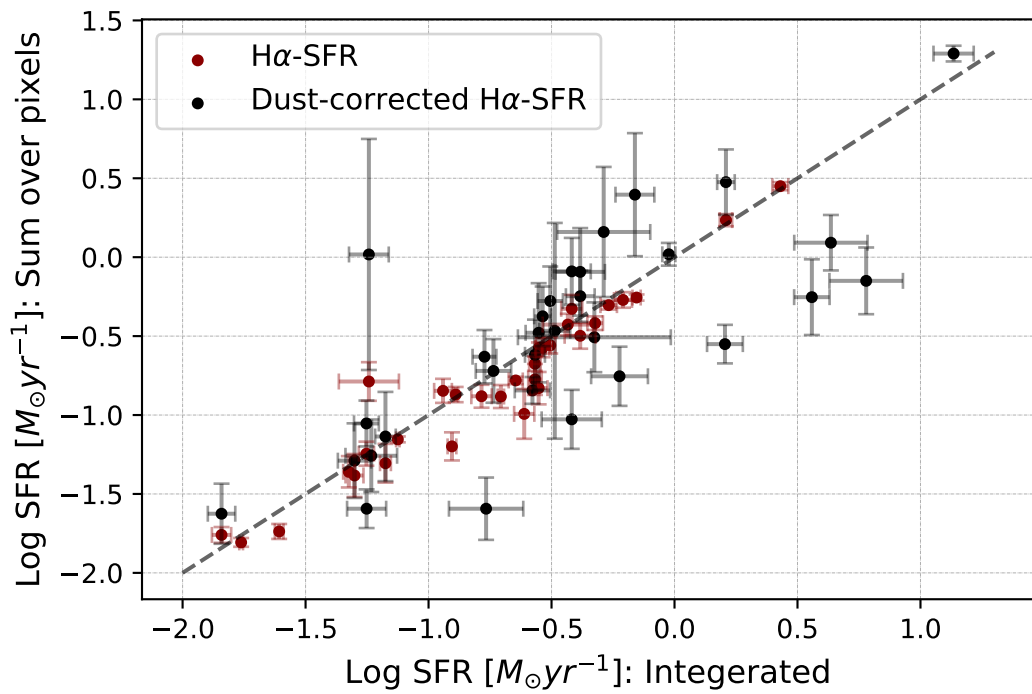


Figure 2.2: Total SFR of galaxies measured by summing up the SFRs per pixel vs. SFR measured from the integrated emission lines. Red data points are $SFR_{H\alpha}$ and black ones are dust-corrected $SFR_{H\alpha}$. Dashed line represents one-to-one relationship.

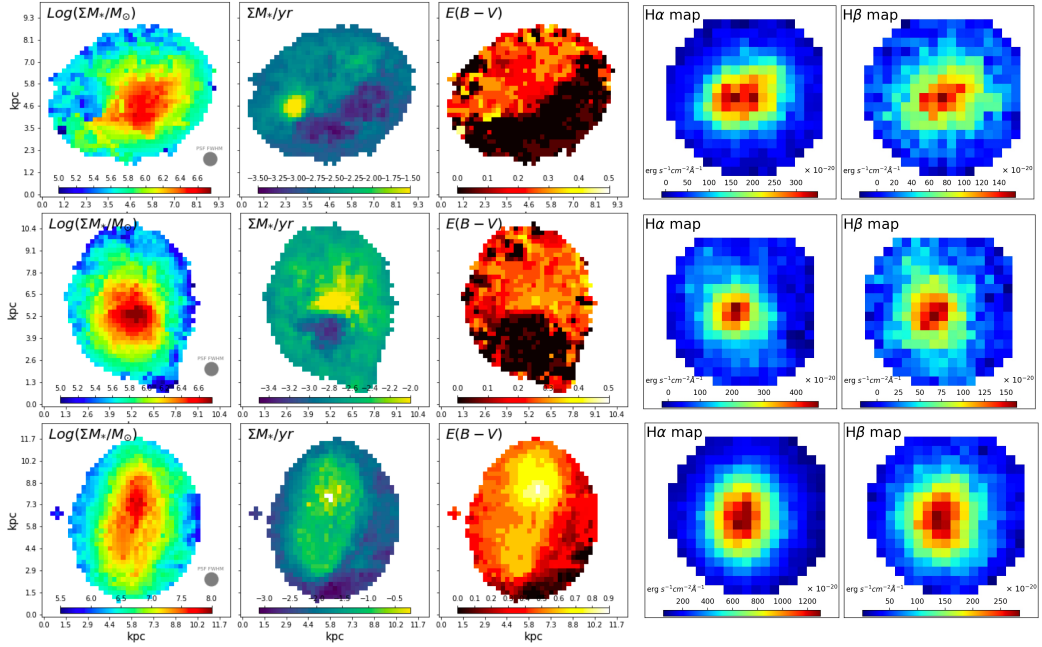


Figure 2.3: From left to right: spatially resolved stellar mass surface density, SFR surface density, stellar $E(B-V)$, $H\alpha$ emission and $H\beta$ emission maps for three galaxies from my sample. To allow for visually comparing *HST* and MUSE PSF, resolved SED-fitting maps (first three in each row) have *HST* quality where input seven images of SED-fitting were PSF matched to the resolution in F160W, and $H\alpha$ and $H\beta$ maps which are derived from 3D datacubes provided by MUSE-Wide Survey have their original PSF.

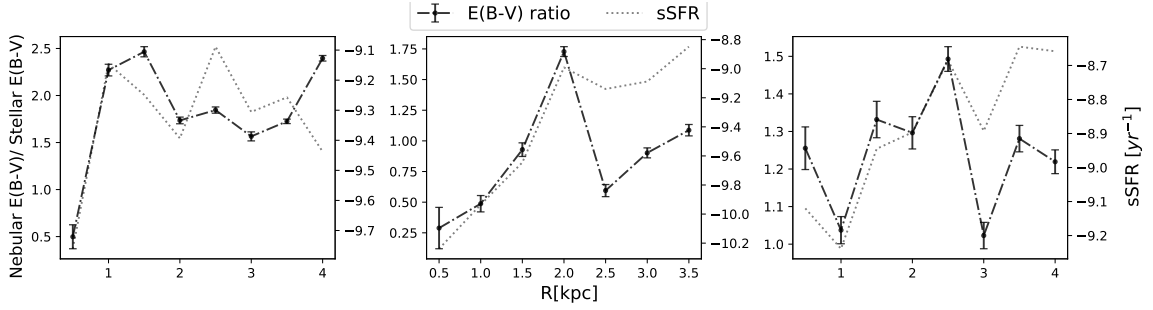


Figure 2.4: Radial profile of nebular to stellar color excess (black dashed lines) overplotted on sSFR profile (grey dotted lines) for 3 sample galaxies which their nebular $E(B-V)$ to stellar $E(B-V)$ ratio profiles closely follow their sSFR profiles. The mass, SFR, stellar $E(B-V)$, $H\alpha$ and $H\beta$ maps for these three galaxies are presented in Figure 2.3 (the top panel of figure 2.3 is corresponding to left panel of this graph).

2.4 Results

2.4.1 Integrated SFR diagnostics

I start by comparing the dust-corrected $SFR_{H\alpha}$ and SFR_{SED} for the integrated light of galaxies in my sample. $SFR_{H\alpha}$ is tracing the ionizing radiation from massive stars ($> 10M_{\odot}$) which provides a relatively instantaneous measure of the SFR ($< 10Myr$) (Kennicutt 1998) whereas SFR_{SED} is measuring the average SFR of the galaxy over its lifetime based on the assumed SFH. Despite tracing different star formation timescales and large errors in SFR_{SED} , these two diagnostics are well-correlated (p-value= 0.0004) as shown in Figure 2.5. The blue dashed line in Figure 2.5 shows the best-fit linear relationship, where the slope is 0.819 ± 0.232 and the intercept is -0.919 ± 0.152 . The slope of this relation is close to unity for lower SFRs with deviation from unity at higher SFR values. This is consistent with

the results from Shivaei et al. 2016 who found a near unity relation between dust-corrected $\text{SFR}_{\text{H}\alpha}$ and SFR_{SED} (UV-to-FIR) for a sample of $z \sim 2$ galaxies. I note that, while the $\text{SFR}_{\text{H}\alpha}$ is reliably corrected for dust attenuation by the Balmer decrement, not including the FIR data in the SED fitting might produce slight underestimation of SFR_{SED} at larger SFR values where more dust attenuation is expected (e.g., Reddy et al. 2010; Casey et al. 2014b; Shivaei et al. 2016). This increases the deviation of the two measures at higher SFRs (decreasing the slope).

My sample of emission line galaxies are residing on or above the main sequence of star forming galaxies (e.g., Noeske et al. 2007; Elbaz et al. 2011), with more massive objects having higher average SFR values (see Figure 2.1). The deviation of the two SFR diagnostics (probing different SFR timescales) at larger SFRs, is hence suggestive of the quenching process starting in the more massive objects in my sample (the so called mass quenching; Peng et al. 2010). In the following subsections I look into resolved distribution of SFR, sSFR, and dust to further learn about the quenching mechanism.

2.4.2 Radial profiles of mass, SFR and sSFR

To combine and compare the resolved spectroscopic and photometric products, I transform pixel measurements to radial profiles by taking the median value of all the pixels in each annulus. I then use the bootstrap method to estimate the standard error of the sample median. While this technique loses some information (e.g. smooths out clumps present in galaxies), the strategy facilitates the interpretation of the results as we avoid complexity and uncertainties of matching pixels between two sets of data.

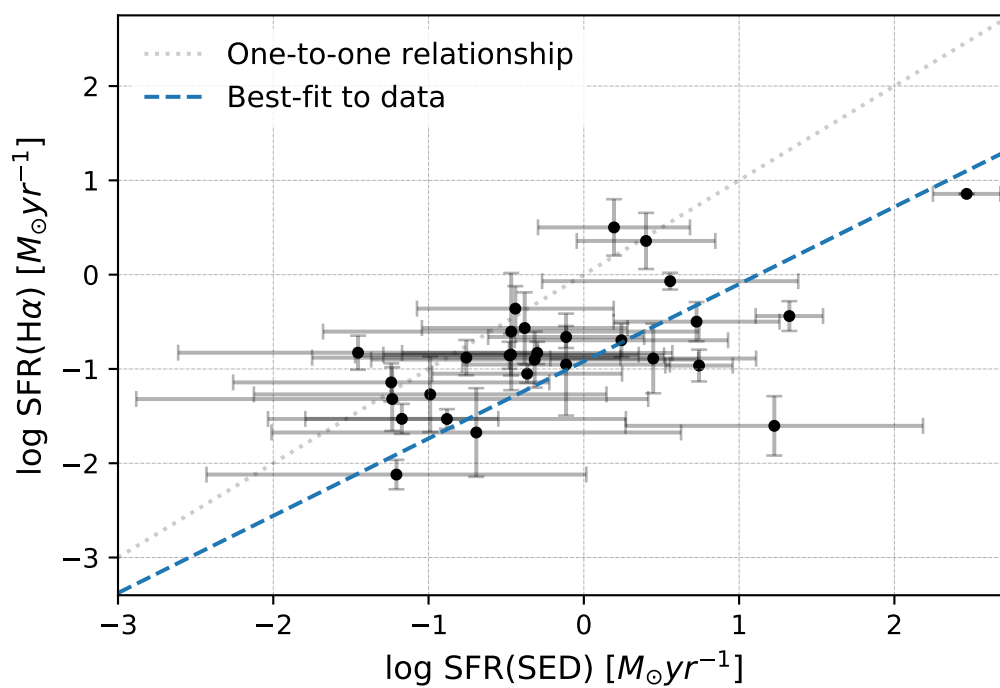


Figure 2.5: Comparison between the $\text{SFR}_{\text{H}\alpha}$ and SFR_{SED} for the integrated light of galaxies. Gray dotted line represents the one-to-one relationship. Blue dashed line represents the best fit to the data with the slope = 0.819 ± 0.232 , and intercept = -0.919 ± 0.152 .

The radial profile of the stellar mass surface density declines smoothly from the most inner regions outwards to the disk, consistent with previous studies (e.g., Wuyts et al. 2012b; Hemmati et al. 2015) at similar redshifts. The radial profile of the SFR also declines towards outer parts of galaxies, but not as smooth as the mass density. In Figure 2.6 I show the radial profile of the median SFR surface density (Σ_{SFR}) over all the galaxies in the sample out to 4.5 kpc radius. Shaded regions in this figure represent the standard deviation over the full sample. Red profile shows the observed $\text{SFR}_{\text{H}\alpha}$ (uncorrected for dust), increasing towards the inner regions of galaxies with a relatively shallow slope. However, the increased SFR in the central regions become clearer when $\text{SFR}_{\text{H}\alpha}$ is corrected for dust using the Balmer decrement (black profile). This also suggests that dust is more centrally concentrated, and decreases towards the outskirts, consistent with previous results (e.g., Hemmati et al. 2015; Nelson et al. 2016).

Nelson et al. 2016 used resolved measurements of $\text{H}\alpha$ and $\text{H}\beta$ emission lines for ~ 600 galaxies at $z \sim 1.4$ to study the radial distribution of $\text{SFR}_{\text{H}\alpha}$ and dust attenuation. They found high central SFRs and steeper dust attenuation gradients with increasing stellar mass of galaxies, such that $\text{H}\alpha$ attenuation ($A_{\text{H}\alpha}$) in the center of galaxies with the average mass of $\log M_*/M_\odot = 10.2$ is up to 2 magnitudes. However, for galaxies with $\log M_*/M_\odot = 9.2$ they observed little dust attenuation at all radii, whereas according to Figure 2.6, dust obscures the SFR by a factor of ~ 3 at the very center of the galaxies in my sample with the average mass of $M_* = 10^{8.71} M_\odot$. In the next subsection I look in more detail into the distribution of dust inside galaxies in this sample.

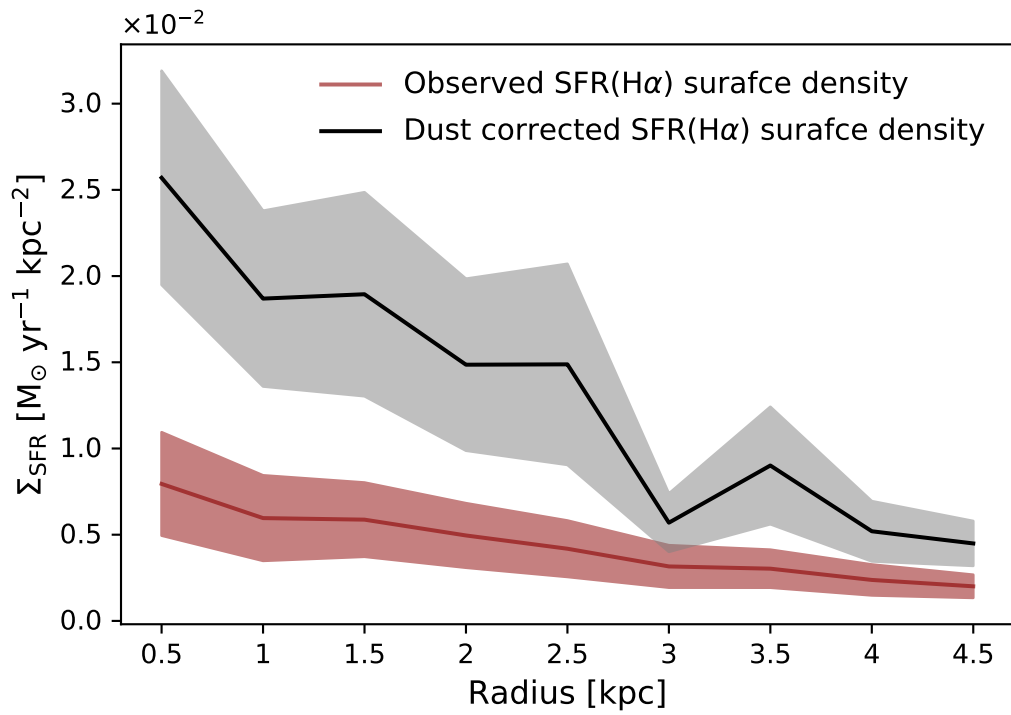


Figure 2.6: Median radial profile of Σ_{SFR} for all the galaxies in the sample. Red and black profiles represent the $\text{SFR}_{\text{H}\alpha}$, and the dust-corrected $\text{SFR}_{\text{H}\alpha}$, respectively. Shaded regions correspond to 1σ error in the data.

To better investigate the mass build up in these galaxies, I also present the radial profile of the specific star formation rate (sSFR) in Figure 2.7. Here, resolved sSFRs are estimated both by pixel-by-pixel SED-fitting (grey line/ shaded region) and dividing the dust-corrected $\text{SFR}_{\text{H}\alpha}$ by the SED-derived stellar mass (blue line/shaded region). In the second approach, the median mass and median SFR of the pixels inside a ring is used to estimate the sSFR per annulus. The shaded regions in this Figure represent the standard deviation of sSFRs at different radii in this sample. As expected, standard deviation is much larger for the sSFR_{SED} profile at all radii which is due to uncertainties associated with SFR_{SED} . The radial profile of the sSFR_{SED} is almost flat throughout the galaxy; however, $\text{sSFR}_{\text{H}\alpha}$ shows ~ 0.8 dex increase in median sSFR from center out to 4.5 kpc radii.

Nearly flat trend for SED-based sSFR was previously observed by Liu et al. 2018 for star forming galaxies with the mass ranging from 10^9 to $10^{10} M_{\odot}$, whereas they found an increasing sSFR profile for galaxies in their most massive bin ($M_{*} > 10^{10.5} M_{\odot}$). Belfiore et al. 2018 also found a mostly flat sSFR profile based on $\text{H}\alpha$ measurements from MaNGA survey for the lowest mass galaxies in a sample of star forming main sequence and green valley galaxies (10^9 to $10^{9.5} M_{\odot}$), and an increasing sSFR profile for higher mass galaxies. However, Figure 2.7 suggests that $\text{sSFR}_{\text{H}\alpha}$ profile is not necessarily flat in this sample with the average mass of $M_{*} = 10^{8.71} M_{\odot}$. This increase of sSFR with radius implies that the central regions of these galaxies formed at earlier times such that they are less gas rich compared to the outer regions, which suggests an inside-out growth scenario for the formation of these galaxies. I note that the sample size here is small and the scatter among the galaxies

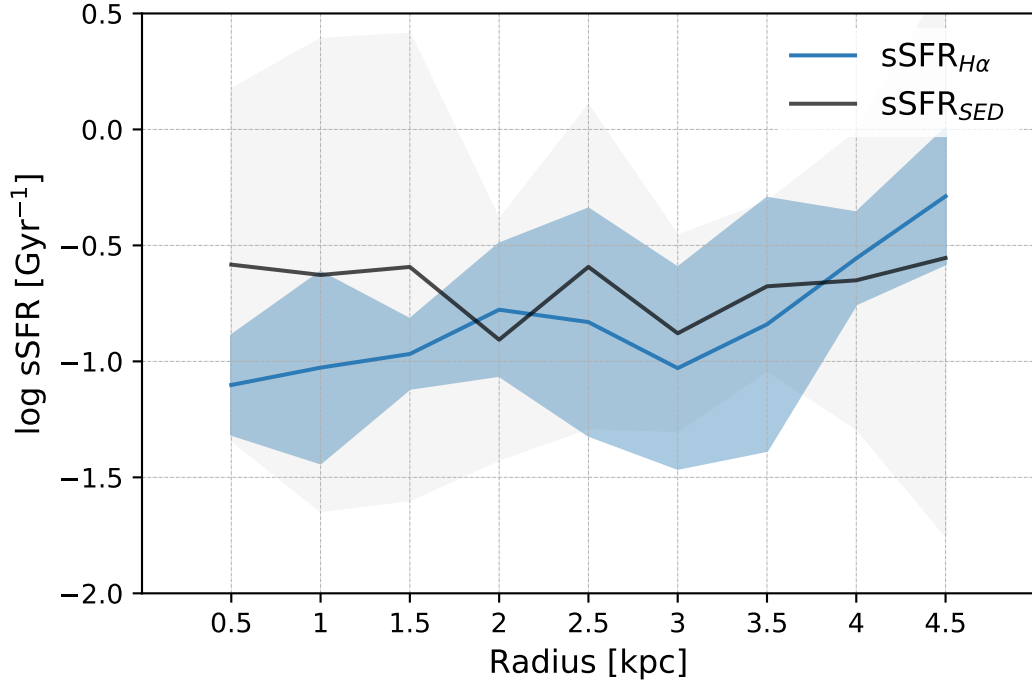


Figure 2.7: Median radial sSFR profiles for galaxies in the sample. Solid black profile presents the SED-derived sSFR and the solid blue profile shows the sSFRs calculated by dividing the dust-corrected $\text{SFR}_{\text{H}\alpha}$ by the SED-derived stellar mass in each annulus. In both profiles, shaded regions represent 1σ error in the data.

(visible from the shaded regions in Figure 2.7) is large to draw strong conclusions. However, the flatness of sSFR_{SED} compared to the decline of the $\text{sSFR}_{\text{H}\alpha}$ towards the central parts of the galaxy, also suggests an inside-out quenching of star formation. This is again due to the different timescales of SFR that $\text{H}\alpha$ and SED are probing, where per unit stellar mass, there is less recent SFR compared to the longer timed average SFR in inner regions of galaxies compared to outer regions in the disk.

2.4.3 Extinction profiles

In this subsection I present the radial profiles for the stellar and nebular extinctions. For this purpose, resolved stellar $E(B-V)$ is estimated through pixel-by-pixel SED-fitting and nebular $E(B-V)$ is measured from the $H\alpha$ and $H\beta$ emission lines in every pixel following Equation 2.3:

$$E(B-V)_{\text{gas}} = \frac{2.5}{k(H\beta) - k(H\alpha)} \log_{10}\left(\frac{H\alpha/H\beta}{2.86}\right) \quad (2.3)$$

where $k(H\alpha)=3.326$ and $k(H\beta)=4.598$, are values of extinction curve at the wavelength of these two lines computed based on Calzetti extinction curve (Calzetti et al. 2000), and 2.86 is the intrinsic Balmer decrement for Case B recombination at $T = 10000$ K and electron density of 10^4 cm^{-3} . The median $E(B-V)$ in each annulus is used to produce radial dust profiles in individual galaxies. I then extracted reddening profile of the sample by taking the median $E(B-V)$ at each annulus over all the galaxies. The radial profiles of both nebular and stellar dust vary from galaxy to galaxy in this sample, so defining one dust profile shape for the whole sample is not valuable. However, integrated properties of galaxies are known to be correlated with dust inside galaxies (e.g., Reddy et al. 2015). I therefore, study the dependence of the reddening profiles on integrated physical properties including stellar mass, SFR and sSFR and found that the profiles are most significantly dependent on the integrated sSFRs.

Figure 2.8 presents the nebular and stellar $E(B-V)$ profiles when I divided the sample into two sSFR bins with similar number of galaxies in each bin. At the lower sSFR bin (left panel of Figure 2.8), the Pearson correlation coefficients between $E(B-V)$ and

radius is within the range of 0 and -0.5 showing a weak radial dependence of both stellar and nebular reddening which can be explained by low values of extinction at all radii for these galaxies. On the contrary, in the higher sSFR bin (right panel of Figure 2.8), the correlation coefficient of both nebular and stellar reddening and radius are less than -0.8, indicative of a strong relation between $E(B-V)$ and radius. I fitted a power-law to the nebular profile as $E(B-V) = Ar^b$ where $A = 0.22 \pm 0.02$ and $b = -0.85 \pm 0.10$ (blue dotted line in Figure 2.8), and a linear relation to the stellar reddening as $E(B-V) = mr + c$ where $m = -0.03 \pm 0.01$ and $c = 0.19 \pm 0.02$ (red dotted line in Figure 2.8).

Clear from Figure 2.8 and as already seen in section 2.4.2, the highest attenuation by dust occurs in the central regions of the galaxies with the exception of stellar $E(B-V)$ in low integrated sSFR galaxies. These plots also indicate that sSFR is affecting both nebular and stellar $E(B-V)$ profiles such that galaxies with higher integrated sSFR, have higher values of both types of reddening at all radii. Also, galaxies in the higher sSFR bin tend to have steeper profiles, showing higher nebular and stellar reddening toward the center of these galaxies.

Another essential notion to examine in this sample is the extra attenuation towards nebular emission lines compared to the stellar light. The ratio of nebular to stellar reddening for the integrated light of galaxies has been extensively studied (e.g., Calzetti et al. 2000; Reddy et al. 2010; Wild et al. 2011; Koyama et al. 2019), there is however a large scatter in this relation. Reddy et al. 2015 related this scatter to physical properties such as sSFR and stellar mass based on observations of star-forming galaxies at $z \sim 2$. Hemmati et al. 2015 presented the nebular to stellar ratio at kpc-scales in a small sample of emission line galaxies

at $z \sim 0.4$, and also found extra reddening towards the nebular emission lines, increasing with the mass surface density. This is consistent with the overall trend seen in this sample, visible in Figure 2.8 where the blue shaded region sits above the red one in inner regions of galaxies with higher mass surface densities.

While the trends of nebular and stellar dust reddening over the whole sample agrees with what has been suggested before, the nebular to stellar reddening ratio in individual galaxies seems unique for every single galaxy. This is expected given the sensitivity of the profiles to the patchiness of dust and the distribution of clumps in galaxies, so a unified trend is not observed for individual galaxies at kpc-scales. Also, the observed ratio of nebular to stellar reddening varies significantly among the galaxies. However, I find that the nebular to stellar color excess profile is closely following the sSFR radial profile such that for the younger parts of the galaxy with higher current SFR (high sSFR), nebular to stellar color excess is increasing significantly. Figure 2.4, presents the radial profile of the nebular $E(B-V)$ to stellar $E(B-V)$ for three sample galaxies over plotted on their sSFR profiles. These are the same galaxies as the resolved kpc-scale maps in Figure 2.3 (galaxies from left to right in Figure 2.4 correspond to those from top to bottom in Figure 2.3). This figure allows visual inspection of correlations between the shape of reddening profiles and the resolved structures inside galaxies, such as the position of star forming clumps (e.g., galaxy on top panels of Figure 2.3) or the non-central mass distribution (e.g., galaxy on bottom panels of Figure 2.3).

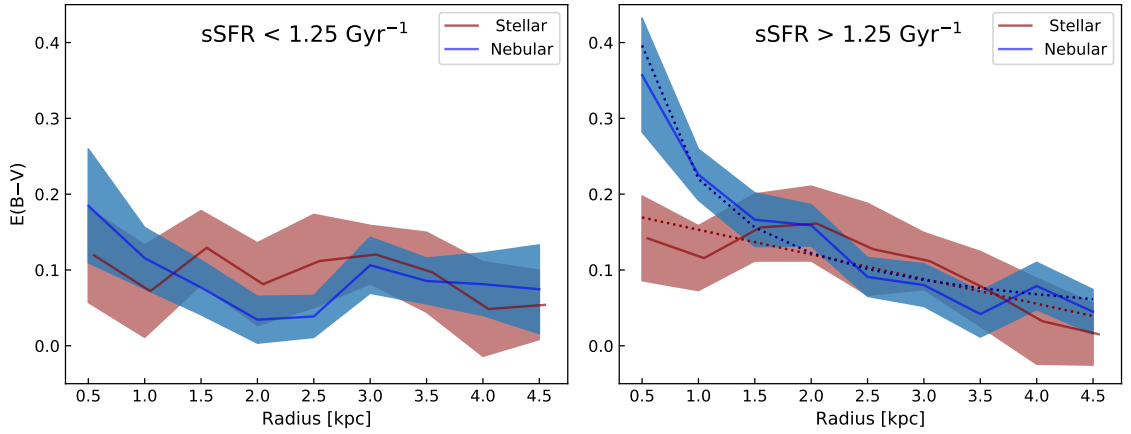


Figure 2.8: Median radial profiles of nebular and stellar color excess for galaxies in the sample. I divided the sample into two bins based on their integrated sSFR such that the number of galaxies in two bins are about the same. Galaxies in the left panel have integrated $\text{sSFR} < 1.25 \text{ Gyr}^{-1}$, and galaxies in the right panel have integrated $\text{sSFR} > 1.25 \text{ Gyr}^{-1}$. In each panel, red and blue profiles present the stellar and nebular color excess, respectively. In all profiles, shaded regions represent 1σ scatter in the data. In the right panel, the dotted lines correspond to the best fit model to the data where the stellar reddening is modeled with a linear relation and nebular profile is fitted by a power-law.

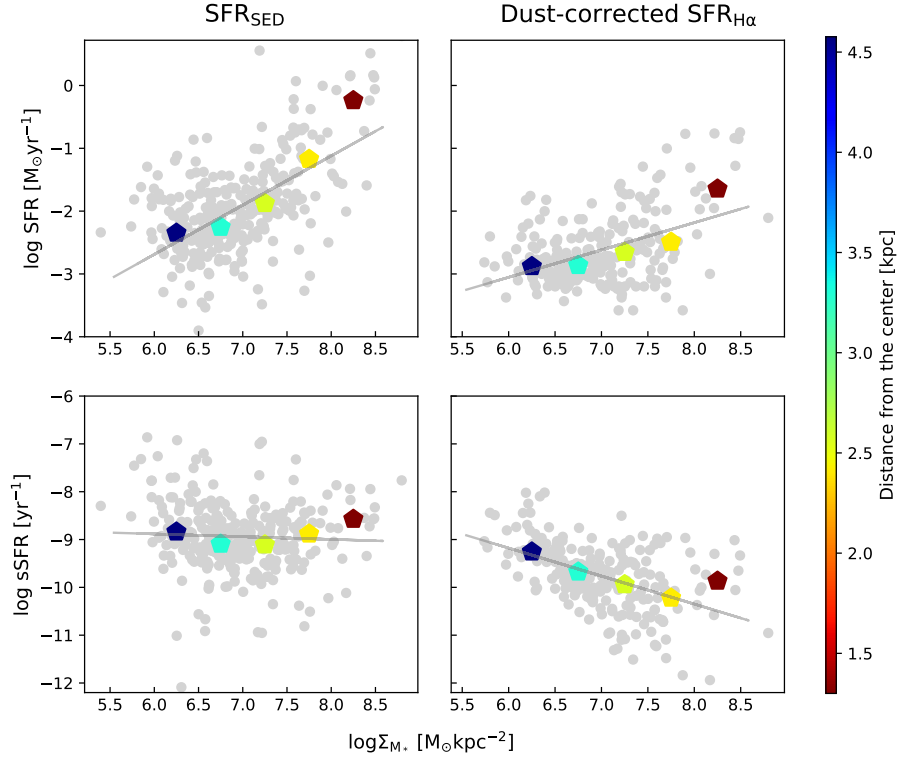


Figure 2.9: Resolved main sequence and resolved sSFR- M_* relations for galaxies in my sample. Gray data points represent individual annuli in galaxies. Two top panels are presenting resolved main sequence with two different SFR diagnostics. Left panel is based on SFR_{SED} and right panel is based on dust-corrected $\text{SFR}_{\text{H}\alpha}$. Bottom panels present sSFR- M_* relation with sSFR_{SED} on the left and dust-corrected $\text{sSFR}_{\text{H}\alpha}$ on the right. Solid gray lines are the best linear fits to grey data points with the fitted parameters presented in Table 2.1. Colored pentagons are the median SFR/sSFR (top/bottom panels) in bins of stellar mass which are color-coded by the average distance from the center of the galaxies.

2.4.4 Resolved SFR- M_* and sSFR- M_* relations

The main sequence of star forming galaxies is a well studied relation between integrated SFR and stellar mass of galaxies (e.g. Noeske et al. 2007; Speagle et al. 2014; Renzini and Peng 2015). This relation can also be studied at resolved scales to reveal how kpc-scale properties are related to unresolved measurements (e.g. Wuyts et al. 2013; Hemmati et al. 2014; Ellison et al. 2018). Studying the sSFR- M_* relation also reveals information about the star-formation history of galaxies. At small scales, this relation can be used to infer when different stellar populations were formed and to differentiate between galaxy growth scenarios using the radial gradient in sSFR- M_* relation.

In Figure 2.9 I present the resolved main sequence, where the top panels show the resolved SFR versus mass surface density and bottom panels showing resolved sSFR versus mass surface density for all the galaxies in the sample. On the left panels, SFR is calculated from SED fitting and right panels are based on dust-corrected $\text{SFR}_{\text{H}\alpha}$. Each grey data point on these plots represents an annulus of a galaxy with the width of 1 kpc, where the median value of the Σ_{M_*} , Σ_{SFR} and sSFR of the pixels are assigned to that annulus. Colored pentagons in these plots show the median SFR/sSFR in mass bins with the width of 0.5 dex, color coded by the distance from the center. I perform least square regression to grey data points shown as solid gray lines with the best fitted parameters presented in table 2.1. In all panels, the best fit line is a good representation of the median SFR/sSFR in each mass bin (colored pentagons) except for the highest mass bin which is most likely due to poor statistics.

The top two panels confirm that linear relation between SFR and M_* (so-called main sequence) exists at resolved scales with different slopes and normalization depending on the SFR diagnostics. This slope is much steeper when SFRs are derived from SED-fitting (0.78 in compare to 0.43) suggesting that massive regions of galaxies have already built up their stellar mass through forming stars over their lifetime. Recent star formation traced by $\text{SFR}_{\text{H}\alpha}$ is relatively lower in these massive regions. I also infer that the position of different parts of galaxies on this plot is strongly dependent on their radial distance such that inner regions (redder points) have higher Σ_{M_*} and Σ_{SFR} .

Table 2.1: Best fit values to the resolved SFR- M_* and sSFR- M_* relations

Relation	Slope	y-intercept	RMSE
$\text{SFR}_{\text{SED}}-M_*$	0.78	-7.39	0.09
$\text{SFR}_{\text{H}\alpha}-M_*$	0.43	-5.66	0.05
$\text{sSFR}_{\text{SED}}-M_*$	-0.05	-8.55	0.09
$\text{sSFR}_{\text{H}\alpha}-M_*$	-0.59	-5.67	0.07

The bottom panels indicate that the sSFR_{SED} results in a shallower trend compared to $\text{sSFR}_{\text{H}\alpha}$ (-0.05 vs. -0.59) which means that the radial gradient in recent SFR traced by $\text{H}\alpha$ is higher in comparison with average SFR traced by SED-fitting. In other words, massive regions which are already quenched show less evidence for recent star formation activity. Also, inner parts of the galaxies (redder points) have higher Σ_{M_*} and lower sSFR, implying that these parts contain the bulge of the galaxy and formed their stars before the outer regions (i.e. disks), which is again an evidence for inside-out growth of these galaxies.

2.5 Summary

In this work, I investigate the resolved photometric and spectroscopic properties of 32 galaxies at $0.1 < z < 0.42$ with stellar masses ranging from $10^{7.7}$ to $10^{10.3} M_{\odot}$. Following are the main points of this study:

- I observe a linear relationship between SFR_{SED} and dust-corrected $\text{SFR}_{\text{H}\alpha}$ with a near unity slope at lower SFRs, and deviation from unity at higher SFR values which can be explained by the effect of dust and/or quenching mechanisms which start in the more massive galaxies of the sample.
- I measure an increase of ~ 0.8 dex in the median $\text{SFR}_{\text{H}\alpha}$ from center to 4.5 kpc radii for galaxies in the sample. This suggests that sSFR is not necessarily constant with radius in relatively low-mass galaxies ($M_{*} < 10^{10} M_{\odot}$) and inside-out growing is a possible scenario for the evolution of these galaxies.
- I find that radial profile of stellar and nebular $E(B-V)$ are strongly dependent on the integrated sSFR of the galaxy. Radial profile of $E(B-V)$ in galaxies with lower sSFR, are weakly dependent on radius; however, in galaxies with high sSFR, both stellar and nebular reddening have significantly higher values of extinction in inner parts of galaxies. I also study the radial profile of the ratio of nebular $E(B-V)$ to stellar $E(B-V)$ which found to be patchy and unique for individual galaxies with no specific trend with radius in this sample.
- I show that the slope and normalization of the resolved $\text{SFR}-M_{*}$ and $\text{sSFR}-M_{*}$ relations are highly dependent on the SFR diagnostics (SFR_{SED} vs. $\text{SFR}_{\text{H}\alpha}$). Also, the

position of different regions of galaxies on these two plots is determined by their radial distance from the center in a way that central regions have higher Σ_{M_*} and Σ_{SFR} and lower sSFR, which implies that these parts formed their stars before the outer parts and is another evidence for inside-out growth of these galaxies.

I developed the methodology of studying resolved properties of galaxy samples with combined *HST*+MUSE data. In future work, I will incorporate the upcoming data from the completed MUSE-Wide Survey, which include ~ 4 times the sample discussed here to build upon my current analysis (data for 44 out of 100 fields of this survey is now available at <https://musewide.aip.de/project/>). Clearly, next generation telescopes and instruments will also allow us to study the spatially resolved properties of large and diverse samples of intermediate and high redshift galaxies with unprecedented detail.

Chapter 3

Resolved Multi-element Stellar

Chemical Abundances in the

Brightest Quiescent Galaxy at $z \sim$

2

3.1 Introduction

Chemical abundances in early-type galaxies have been one of the main tools for studying their formation history. Specifically the α -enhancement (α -element-to-iron abundance ratio compared to the solar abundance ratio, e.g., $[\text{Mg}/\text{Fe}]$), is sensitive to the timescale of star formation because of the different lifetimes of the stars that produce these elements in supernovae (SNe). SN Type II (core-collapse) release mostly α -elements

including oxygen, magnesium, silicon, etc. (Woosley and Weaver 1995) whereas SN Type Ia mostly release iron and other iron peak elements. This implies that galaxies with more extended star formation histories (SFHs) are expected to have a lower $[\alpha/\text{Fe}]$ and higher $[\text{Fe}/\text{H}]$.

The α -enhancement, as a timescale diagnostic, has been extensively used to infer the formation histories of early-type galaxies in the local universe (e.g., Thomas et al. 2003b; Greene et al. 2019). However, these archaeological studies can reconstruct the formation history of the stars currently in the galaxy, and if there has been a significant amount of merging, then those stars were born in a range of different progenitor galaxies with potentially different formation histories. Therefore, to study conditions in the main progenitors of today's ellipticals, including highly star-forming dust-obscured galaxies at $z > 3$ (e.g., Toft et al. 2014; Casey et al. 2014a; Valentino et al. 2020), we need to observe quiescent galaxies closer to the epoch of quenching, before the majority of merger activity had occurred and polluted the population. At high redshifts, nearly all chemical studies have focused on the gas-phase metallicity, measured using nebular emission lines, which traces the current composition of the interstellar medium (ISM) and is affected by inflows and outflows. Stellar abundances requiring absorption line measurements are more challenging, but they provide complementary information by tracing the composition of ISM when the stars were forming. Furthermore, stellar abundances are the only chemical probe available for quiescent galaxies that lack bright emission lines and may be gas-poor. However, the faintness of high- z quiescent galaxies makes spectroscopic observations extremely challenging.

In recent years, several authors have attempted to extend stellar chemical abundance studies to higher redshifts using a single or stacked spectra of a handful of quiescent galaxies (e.g., Onodera et al. 2015; Lonoce et al. 2015; Kriek et al. 2019; Lonoce et al. 2020). Currently, there is only one quiescent galaxy at $z \sim 2$ for which [Fe/H] and [Mg/Fe] have been measured to ~ 0.1 dex precision (COSMOS-11494, Kriek et al. 2016). This galaxy is the most Mg-enhanced massive galaxy ever observed and is thus believed to have had a very short star formation timescale compared to that inferred from local samples. Results from this unique object suggested that the chemical composition of massive galaxies may have evolved substantially after they quenched, likely through mergers. However, more observations are needed to confirm this scenario.

In this work, I analyze the spectra of MRG-M0138, a gravitationally lensed quiescent galaxy at $z = 1.98$ discovered by Newman et al. 2018a. I measure its detailed stellar abundance pattern and compare it to COSMOS-11494 and local massive galaxies that are representative of its descendant. Moreover, for the first time for such a distant quiescent galaxy, I measure the gradient in age, α -enhancement and iron abundance to investigate the uniformity of the star formation history. In Section 3.2 I briefly present my data, in Section 3.3 I explain the full spectral fitting process, models and assumptions, and in Section 3.4 I present my results, the measured age and chemical abundances of 8 elements. I discuss the implication of my results in Section 3.5. Where necessary I assume a flat Λ CDM cosmology with $\Omega_m = 0.3$ and $H_0 = 70 \text{ km s}^{-1}$.

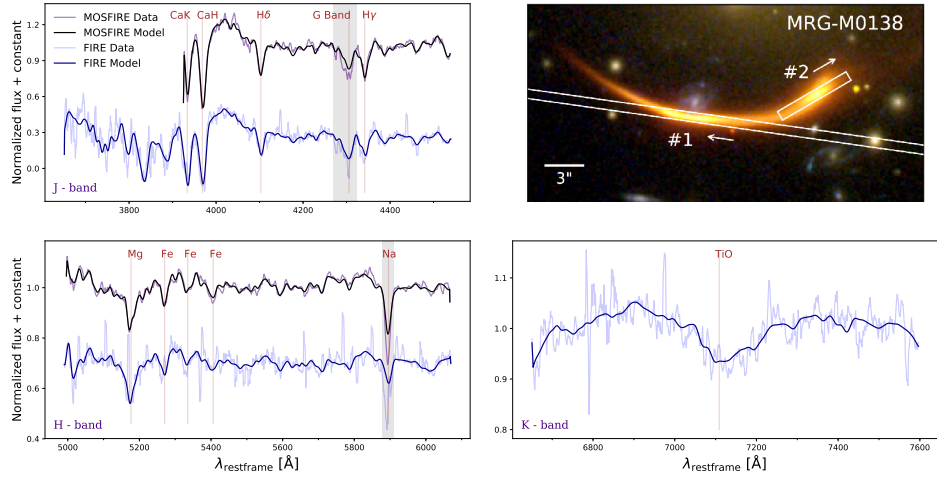


Figure 3.1: The upper right panel presents *HST* observations of the two brightest images of MRG-M0138 along with the placement of the slit on each image (reproduced from Newman et al. 2018b). Other panels show the integrated spectra of these two images observed with Keck/MOSFIRE (purple, Image 1 in the upper right panel) and Magellan/FIRE (light blue, Image 2) in J, H, and K bands. The best-fit model to each spectrum is shown in solid black or blue. Grey shaded regions are masked in the spectral fitting process. For display purposes, all spectra are smoothed to 370 km s^{-1} by taking the inverse variance weighted mean.

3.2 Data

MRG-M0138 is a gravitationally lensed galaxy with five different images. Two spectroscopic observations have been made of this galaxy, one of its brightest image ($H=17.1$) taken with the near-infrared spectrograph MOSFIRE (McLean et al. 2010, 2012) at the Keck 1 telescope in the J and H bands, and the other of the second-brightest image taken with the near-infrared echellete FIRE (Simcoe et al. 2013) at the Magellan Baade telescope. The MOSFIRE spectrum has a signal-to-noise ratio (S/N) of 137 per velocity dispersion element (~ 300 km/s) in H band, which is by far the most detailed spectrum of a quiescent galaxy at a similar redshift. The FIRE spectrum covers a wider wavelength range with a lower S/N=77 and is mainly used as a cross-check in this analysis. Details about these observations and data reduction processes can be found in Newman et al. 2018a.

I also have resolved spectra in a series of seven bins along the MOSFIRE slit, which I use to derive age and metallicity gradients across this object (for details about these spectra see Newman et al. 2018b). Also, using the resolved rotation curve of this galaxy (Newman et al. 2018b), I am able to remove rotation from the two-dimensional spectrum. After this derotation, the galaxy spectral features are aligned vertically while the sky emission lines are tilted. By extracting a one-dimensional spectrum using inverse variance weighting, I then obtain a remarkably clean integrated spectrum that is virtually free of the sky line residuals that normally affect near-infrared spectra.

The wavelength ranges used for the fitting process in this work are 3925 - 4540 Å and 4995 - 6070 Å for the MOSFIRE spectrum and 3650 - 4540 Å, 4990 - 6070 Å and 6650 - 7600 Å for the FIRE spectrum. In both spectra, I mask the region between 4270 and

4325 Å where there is evidence for residual telluric absorption. I also mask the Na D line, which I found to be too strong to be a purely stellar feature and thus requires additional absorption by an interstellar medium (see Section 3.4.3). The two brightest images of the MRG-M0138 and our integrated spectra are shown in Figure 3.1.

3.3 Full spectral fitting

I analyze our spectra using *alf* (Conroy and van Dokkum 2012; Conroy et al. 2018), which is an absorption line fitter of near-infrared and optical spectra of stellar systems older than 1 Gyr. This code uses a Markov Chain Monte Carlo (MCMC) algorithm to fit the data to combined libraries of empirical and synthetic stellar spectra covering a wide range of parameter space (Sánchez-Blázquez et al. 2006; Choi et al. 2016; Villaume et al. 2017). I run *alf* in full mode, which fits for 46 parameters as described by Conroy et al. 2018, including velocity, velocity dispersion, age, abundances of O, C, N, Na, Mg, Si, K, Ca, Ti, V, Cr, Mn, Co, Ni, Cu, Sr, Ba and Eu, along with various nuisance parameters. I note that the S/N of our spectra is not sufficient to meaningfully constrain all of the abundance ratios, but I identify 8 elements whose abundance is measured to < 0.1 dex precision from the MOSFIRE spectrum and confine my analysis in the rest of this chapter to these species: Fe, Mg, Ca, Si, Ni, C, Mn and Cr. I should note that although the MOSFIRE spectrum formally constrained the Ti abundance to 0.1 dex precision, the spectrum does not cover the strong TiO absorption features, so I exclude it from my results. In the fitting process, errors are rescaled by a jitter term to ensure they are realistic, which is useful in the near-infrared where systematic errors in the data reduction can be significant.

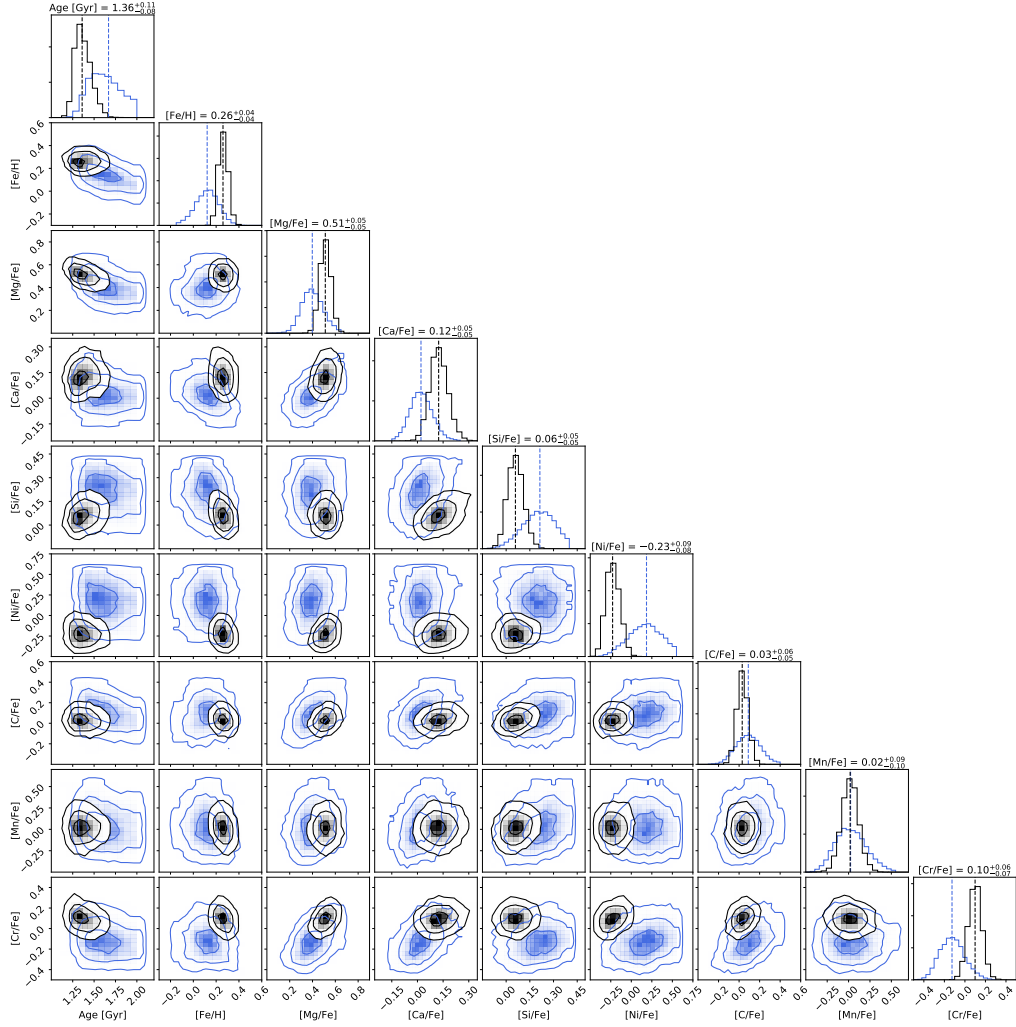


Figure 3.2: Corner plot showing covariances among age, $[\text{Fe}/\text{H}]$, and the abundances of elements for which $[\text{X}/\text{Fe}]$ is measured to < 0.1 dex precision in the MOSFIRE spectrum. Black contours show results from fitting the MOSFIRE spectrum, and blue contours correspond to fitting the FIRE spectrum, which has lower S/N. These contours correspond to 1σ , 2σ and 3σ levels. Titles show the median of the marginalized posteriors obtained from the MOSFIRE spectrum

In the modeling, I assume a single age population and a Kroupa IMF (Kroupa 2001). I allow the abundance of individual elements ($[X/H]$) to vary from -0.3 to 1. I also perform following robustness tests: changing the degree of the polynomial fitted to the continuum, fixing the abundances of poorly constrained elements to values typical of local massive early-type galaxies (ETGs), allowing the response function, which determine the change in the spectrum due to a change in the abundance of a single element, to vary with metallicity (rather than using response functions calculated at solar metallicity, our default procedure), and restricting the fit to $\lambda > 4000 \text{ \AA}$ to exclude the Ca HK lines. Results from all of these tests are well within the error-bar of the final reported values.

I followed the same procedure for each of the 7 resolved spectra. However, due to their lower S/N, I focus only on the age, $[Fe/H]$, and $[Mg/Fe]$ derived from these spectra.

Moreover, in order to compare the properties of this high- z quiescent galaxy with local counterparts, I also perform the fitting process with exactly the same models and assumptions on six stacked spectra of SDSS (Sloan Digital Sky Survey) early-type galaxies from Conroy et al. 2014. These high S/N spectra are from the inner $0.5 R_e$ of passive galaxies, and are binned by their velocity dispersion spanning from 100 to 320 km s^{-1} . The only difference is the wavelength range of the fit, which is from 4000 - 7300 \AA and 8000 - 8850 \AA for SDSS spectra.

3.4 Results

Figure 3.1 presents the best-fit models to each spectrum, which provide excellent fits. In Figure 3.2, corner plots show the derived values of age, $[Fe/H]$, and the abundances

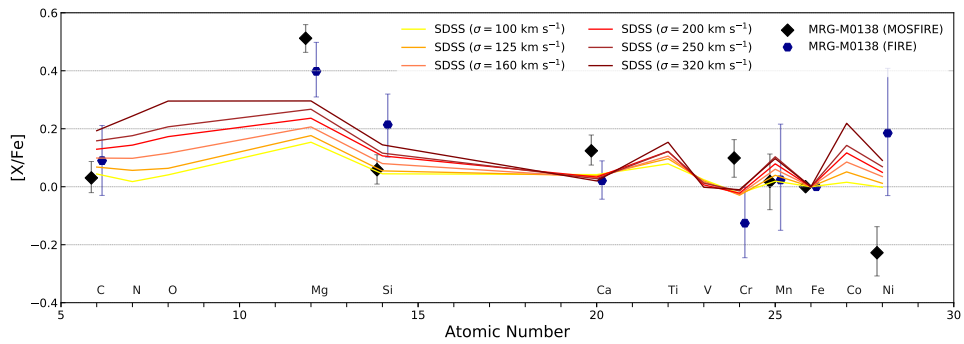


Figure 3.3: $[X/Fe]$ for different elements derived for MRG-M0138 and stacked spectra of SDSS early-type galaxies. Black diamonds represents values for MRG-M0138 derived from the MOSFIRE spectrum, and blue hexagons correspond to the FIRE spectrum. Each colored solid line represents local ETGs with a specific velocity dispersion, σ , as indicated in the legend. Abundances of most of the elements increase with increasing σ . Interestingly, $[Mg/Fe]$ is significantly higher in MRG-M0138 than is typical of local galaxies, even those with the highest σ .

of 7 elements (Mg, Ca, Si, Ni, C, Mn, Cr) that have < 0.1 precision from the MOSFIRE fit, which is unique for a $z \sim 2$ galaxy. Purple contours show results from the MOSFIRE data, and blue contours show results from the FIRE spectrum. Posteriors from the two spectra overlap and I assess the consistency between the two sets of parameters using the Q_{DM} statistic which follows a χ^2 distribution (Equation 49, Raveri and Hu 2019). I derive a p -value of 0.04 that indicates marginal tension at the $\sim 2\sigma$ level between two sets of parameters. This might reflect small residual systematics in the spectra, or the fact that they probe different light-weighted radii in the galaxy due to the lens mapping. I also found that excluding [Ni/Fe] from the comparison removed the tension ($p = 0.13$) and implied full consistency.

The estimated age of the galaxy is 1.37 ± 0.11 Gyr from the MOSFIRE spectrum (corresponding to $z_{\text{form}} = 3.3 \pm 0.2$) and 1.67 ± 0.23 Gyr from the FIRE spectrum ($z_{\text{form}} = 3.8 \pm 0.5$).

3.4.1 Comparison to COSMOS-11494 and local massive ETGs

I compare the abundances of different elements in this unique high- z quiescent galaxy with the chemical abundances of local ETGs in Figure 3.3. In this figure, solid lines represent [X/Fe] derived from stacked spectra of the inner regions of SDSS early-type galaxies. It is known that the star formation history of passive galaxies is well correlated with their velocity dispersion (e.g., Graves et al. 2010), and that is why these galaxies are binned by this parameter. Figure 3.3 shows that the abundance of some elements, such as calcium, does not depend on the velocity dispersion, whereas for some other elements,

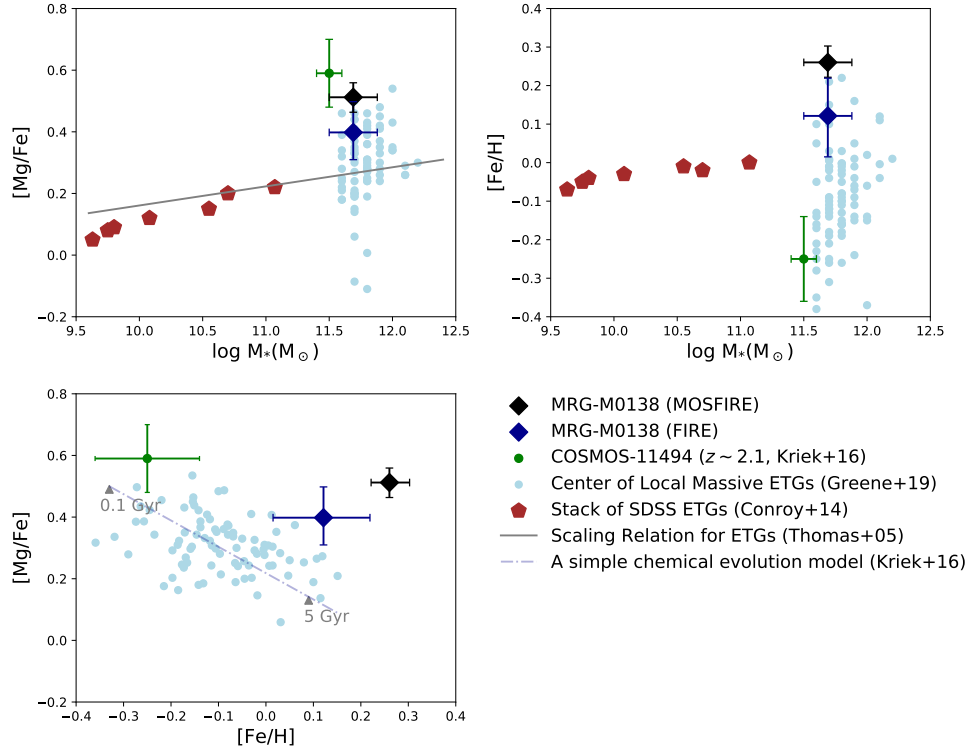


Figure 3.4: Relationships among stellar mass, $[Mg/Fe]$, and $[Fe/H]$ for MRG-M0138 (black and blue diamonds, corresponding to the MOSFIRE and FIRE measurements), COSMOS-11494 at $z = 2.1$ (green circle; Kriek et al. 2016), and the centers of local massive ETGs (light blue circles; Greene et al. 2019). Red pentagons show measurements derived from the SDSS stacks of Conroy et al. 2014. The solid line in the upper left panel shows the scaling relation from Thomas et al. 2005. The $z \sim 2$ galaxies are distinct from each other and from the centers of local massive ETGs in the $[Mg/Fe]$ vs. $[Fe/H]$ plane (lower panel). A simple chemical evolution model (dot-dashed line) from Kriek et al. 2016 could plausibly explain the abundances of COSMOS-11494 with a very short formation timescale, but this model cannot account for the high $[Mg/Fe]$ and $[Fe/H]$ of MRG-M0138.

such as magnesium and carbon, the abundance is a strong function of velocity dispersion (Conroy et al. 2014). The abundance ratios of MRG-M0138 and this local sample of ETGs are relatively consistent, except for $[\text{Mg}/\text{Fe}]$, which is significantly (~ 0.2 dex) higher for MRG-M0138 even compared to local ETGs at the highest velocity dispersion bin (320 km s^{-1}). The only other $z \sim 2$ quiescent galaxy with a comparably precise measurement is COSMOS-11494 (Kriek et al. 2016), which also shows a strong Mg-enhancement.

I then present the relation between $[\text{Mg}/\text{Fe}]$, $[\text{Fe}/\text{H}]$ and stellar mass (M_*) for MRG-M0138 and COSMOS-11494 in Figure 3.4. To allow for comparison between the stellar populations of quiescent galaxies at the present time and $z \sim 2$, I also show the abundances of a sample of local ETGs from the MASSIVE survey (Ma et al. 2014). Considering the high stellar mass of MRG-M0138 ($\log M_* = 11.69 \pm 0.12$), this galaxy is likely the progenitor of a very massive local elliptical, and the MASSIVE survey is an integral field spectroscopic survey of the most massive early-type galaxies within ~ 108 Mpc, thus providing a perfect comparison sample. Chemical abundances and masses of this sample are adopted from Greene et al. 2019; I use abundances measured in the inner 2 kpc. Additionally, I added the sample of the stacked spectra of SDSS galaxies from Conroy et al. 2014 to the first two panels of Figure 3.4, to show the stellar mass dependence of $[\text{Mg}/\text{Fe}]$ and $[\text{Fe}/\text{H}]$ over a wide range of stellar mass.

As predicted from local samples, $[\text{Mg}/\text{Fe}]$ is increasing with stellar mass, but both massive $z \sim 2$ galaxies lie noticeably away from the simple scaling relation based on local ETGs adopted from Thomas et al. 2005. Even considering the scatter among local ETGs in the MASSIVE sample, COSMOS-11494 has higher ratio of $[\text{Mg}/\text{Fe}]$ than any of the local

ETGs, and MRG-M0138 is comparable to the most Mg-enhanced galaxies in this sample. In contrast to the relatively similar behavior of MRG-M0138 and COSMOS-11494 in the $[\text{Mg}/\text{Fe}]-M_*$ parameter space, these two galaxies are completely distinct from each other when looking at the $[\text{Fe}/\text{H}]-M_*$ relation. Generally, $[\text{Fe}/\text{H}]$ is not a strong function of stellar mass, and in the high mass regime, local ETGs from MASSIVE sample span a relatively wide range of $[\text{Fe}/\text{H}]$, with values as low as -0.36 to a maximum of $+0.15$. In this parameter space, MRG-M0138 with $[\text{Fe}/\text{H}]$ of $+0.26 \pm 0.04$ is more iron-rich than any of these local galaxies, whereas COSMOS-11494 with $[\text{Fe}/\text{H}] = -0.25 \pm 0.11$ is among the galaxies with the lowest $[\text{Fe}/\text{H}]$ ratio. This is also emphasized in the last panel of Figure 3.4, which shows that both $z \sim 2$ galaxies are distinct from the local sample but with different abundance patterns, which implies significant differences in the enrichment histories of these galaxies.

Furthermore, the $[\text{Ca}/\text{Fe}]$ ratio is also significantly different in MRG-M0138 and COSMOS-11494. MRG-M0138 has $[\text{Ca}/\text{Fe}] = +0.12 \pm 0.05$, comparable to local ETGs, whereas COSMOS-11494 is very Ca-enhanced ($[\text{Ca}/\text{Fe}] = +0.59 \pm 0.07$; Kriek et al. 2016). Its very high $[\text{Ca}/\text{Fe}]$ ratio is surprising, since local ETGs show almost no Ca-enhancement. In MRG-M0138, on the other hand, the abundance of Ca does not follow Mg, which is consistent with previous studies that showed a different behavior of these two elements, specifically the underabundance of Ca relative to other α -elements (e.g., Worthey 1998; Thomas et al. 2003a; Smith et al. 2009). Figure 3.3 shows one aspect of the dissimilar behavior of Mg and Ca: $[\text{Mg}/\text{Fe}]$ increases with increasing velocity dispersion, whereas $[\text{Ca}/\text{Fe}]$ is almost constant.

3.4.2 Stellar Age and Abundance Gradients

I present my unique measurement of the spatially resolved age, [Mg/Fe], and [Fe/H] for MRG-M0138 in Figure 3.5. The best-fit model to each spectra is shown in Figure 3.6. In each spatial bin, I take the light-weighted radial position from Newman et al. 2018b. I fit our resolved data with a functional form of $A \times \log(R/R_e) + B$, where A and B are presented on each panel of Figure 3.5.

I do not detect an age gradient ($A = 0.03 \pm 0.15 \text{ Gyr dex}^{-1}$) or a gradient in [Mg/Fe], which suggests that the star formation history was fairly uniform across this galaxy. However, I find a marginally negative gradient for [Fe/H] with a slope of -0.35 ± 0.27 . These gradients are comparable to those seen in local early-type massive galaxies. For example, Greene et al. 2015 found gentle gradients in age ($A = -0.35 \pm 0.11 \text{ Gyr dex}^{-1}$, see their Table 1) and [Fe/H] ($A = -0.46 \pm 0.11$) and no gradient in [Mg/Fe] for the galaxies in the highest velocity dispersion bin ($\sigma > 290 \text{ km s}^{-1}$) of the MASSIVE survey. The small metallicity gradient in MRG-M0138 ($-0.040 \pm 0.028 \text{ dex/kpc}$) is comparable to the gas metallicity gradients in high- z massive star-forming galaxies, and based on simulations, seems to require strong feedback mechanisms during the star-forming phase to mix the gas throughout the disk of this galaxy (e.g., Gibson et al. 2013; Leethochawalit et al. 2016; Ma et al. 2017).

Fairly uniform stellar age and a uniformly high [Mg/Fe] imply that star formation must have stopped abruptly and relatively uniformly across the disk around $z \sim 3.3$. This is consistent, at least qualitatively, with the short gas depletion times and disky kinematics observed in many high- z submillimeter galaxies proposed as progenitors of galaxies like

MRG-M0138 (Hodge et al. 2012; Aravena et al. 2016; Jiménez-Andrade et al. 2020).

Another issue of key theoretical importance is the link between quenching and bulge formation. Suggested by compaction models, violent disk instabilities funnel gas into galaxy centers, leading to nuclear star formation just prior to galaxy-wide quenching via gas consumption and outflows (e.g., Dekel and Burkert 2014; Zolotov et al. 2015; Tacchella et al. 2016; Wu et al. 2020). However, some observation of quiescent galaxies at $z \sim 2$ reported no indication of a bulge (Toft et al. 2017), calling into question the generality of this model. In this context, although MRG-M0138 has a small bulge-like structure resolved in *HST* imaging ($R_e = 800$ pc) that contains 26% of the light (Newman et al. 2018a), our ground-based spectroscopy cannot reach within $0.5R_e = 2.4$ kpc, which is necessary to investigate the bulge stellar populations and thereby test compaction or other related quenching models. These further investigations will become possible with future *JWST* observations.

3.4.3 Evidence for an Interstellar Medium

Na D absorption is very strong in MRG-M0138. If we interpret the absorption as entirely photospheric, my alf fits imply an unreasonably high $[\text{Na}/\text{H}] \sim 2.5$. This strongly suggests that an interstellar medium (ISM) is responsible for some of the Na D absorption. To place a lower limit on the column density of ISM, I assume a maximum stellar $[\text{Na}/\text{H}] = +1$, consistent with observations of local ETGs (Conroy et al. 2014), and measure the equivalent width (EW) of Na D for a model with the age of MRG-M0138. In this model, $\text{EW}(\text{NaD}) = 3.57 \text{ \AA}$, and the measured value in the MOSFIRE spectrum, is $\text{EW}(\text{NaD}) =$

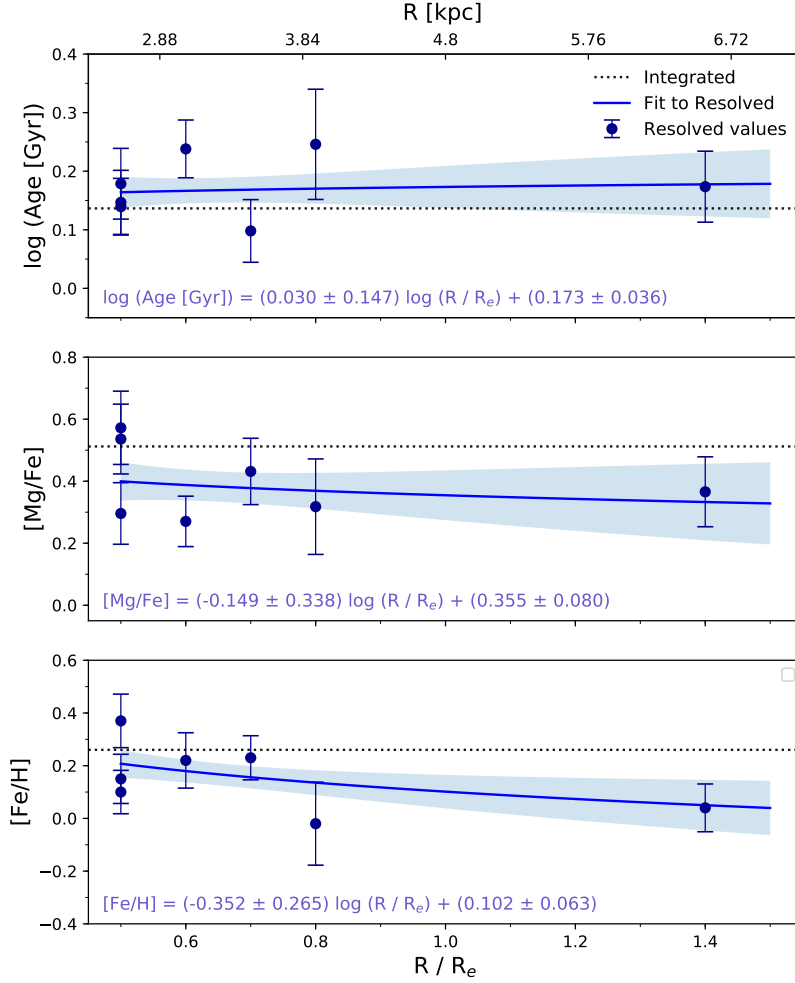


Figure 3.5: Spatially resolved age, $[\text{Mg}/\text{Fe}]$ and $[\text{Fe}/\text{H}]$ for MRG-M0138. The flux-weighted radius in each spatial bin is indicated as R/R_e . Black dotted lines represent the measured value from the integrated spectra. Solid blue line represents the fit to the resolved data in the form of $A \times \log(R/R_e) + B$, where A and B are presented in each panel. I find that age and $[\text{Mg}/\text{Fe}]$ are uniform over $0.5 - 1.4R_e$, while I detect a marginally negative gradient in $[\text{Fe}/\text{H}]$.

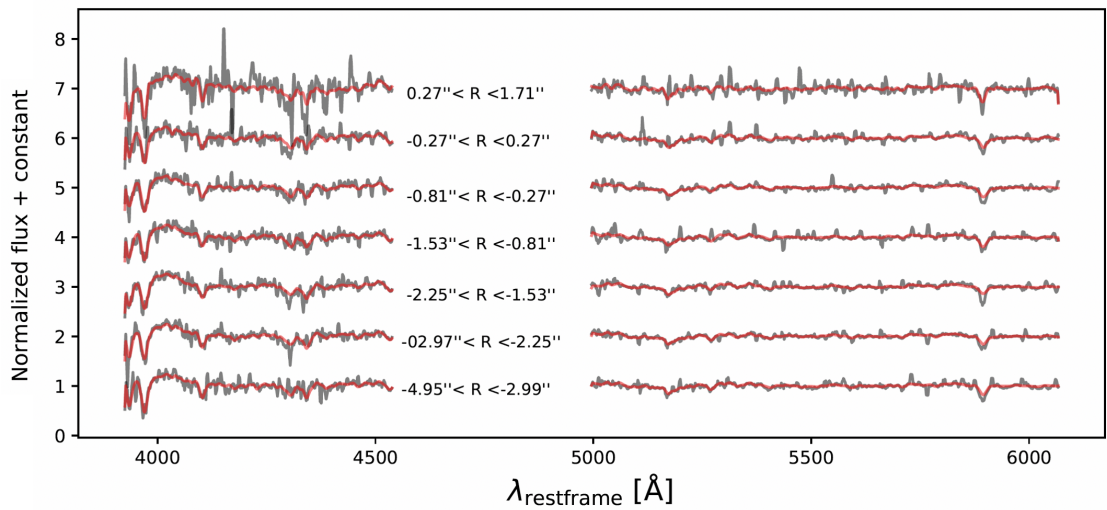


Figure 3.6: Resolved spectra of MRG-M0138 in seven bins observed with Keck/MOSFIRE (grey lines) and the best-fit model to each spectrum which are shown in red. Extraction aperture (R) for each bin is specified in arcsec along the slit relative to the position of peak flux. For display purposes, all spectra are smoothed to 370 km s^{-1} by taking the inverse variance weighted mean.

$5.02 \pm 0.12 \text{ \AA}$. Now we can simply assume that the excess absorption is due to the ISM, $\text{EW}(\text{NaD})_{\text{ISM}} = 1.45 \text{ \AA}$, and then assuming an unsaturated interstellar absorption line, we can estimate a lower limit for the column density of the sodium, $N(\text{Na}) > 5 \times 10^{12} \text{ cm}^{-2}$, using the relation from Spitzer 1978 and the oscillator strength from Morton 1991.

Using the linear relation between the neutral sodium column density and neutral atomic and molecular hydrogen column density $N(\text{H})$ in the diffuse ISM from Ferlet et al. 1985, we can estimate $N(\text{H}) \sim 9 \times 10^{20} \text{ cm}^{-2}$. If we assume the neutral hydrogen is distributed within the effective radius ($R_{e,\text{maj}} = 4.8 \text{ kpc}$, axis ratio $b/a = 0.26$; Newman et al. 2018a) with this column density, we find a lower limit for the neutral hydrogen mass within $1 R_e$ of $\sim 10^8 M_{\odot}$. This is small compared to the stellar mass of the galaxy ($M_{\text{HI}+\text{H}_2}/M_{*} > 3 \times 10^{-4}$), indicating that although quenching did not completely remove the ISM, our observations would be consistent with a very small gaseous reservoir remaining. I note this is a very conservative lower limit on the gas mass of the MRG-M0138, which is far below the current detectable range of the deepest radio observations targeting dust continuum or CO line emission. Therefore, it is complementary to radio observations that detect or place an upper limit on the ISM mass of this galaxy, which would better provide insight into the processes that quenched its star formation.

3.5 Discussion

I have obtained an extremely high S/N spectrum of MRG-M0138, a lensed quiescent galaxy at $z = 2$. I measured the stellar age, $[\text{Fe}/\text{H}]$, and abundance ratios $[\text{X}/\text{Fe}]$ for 7 species for the first time in a $z \sim 2$ galaxy. Interestingly the abundance ratio pattern

(Figure 3.3) seems compatible with massive local ETGs for most elements, with the major exception of Mg. This is striking, since Mg is produced exclusively in core-collapse SNe and so is a pure tracer of massive stars. The very high [Mg/Fe] ratio I find is particularly remarkable when coupled with the high [Fe/H] (Figure 3.4), which renders MRG-M0138 dissimilar from the centers of local ETGs.

The chemical abundances of MRG-M0138 and COSMOS-11494, the only two quiescent galaxies at $z \sim 2$ with precise abundance measurements, suggest that even the centers of today’s massive ETGs have not evolved passively. If further observations show that these two systems are typical of $z \sim 2$ quiescent galaxies, it will require a significant mixing of stars into the centers of massive galaxies over time. This cannot be explained solely by inside-out growth, a paradigm that is supported largely by the observed modest evolution in the central density compared to the dramatic evolution seen in the outskirts of massive galaxies (e.g., Patel et al. 2013). Instead these first two observations suggest that the central chemical abundances evolve substantially, which implies that although mergers may have the largest effect on the galaxy outskirts, they are nonetheless able to pollute the galaxy centers significantly. More work is needed to address the question of whether cosmologically motivated merger histories can explain the apparent chemical evolution.

The α -enhancement is a common method of estimating formation timescale (t_f) of low-redshift quiescent galaxies, for example, using the Thomas et al. 2005 relation: $[\alpha/\text{Fe}] \approx \frac{1}{5} - \frac{1}{6} \log(t_f)$. Applying this linear relation to MRG-M0138 results in unrealistically short formation timescale of ~ 0.05 Gyr. This suggests that the assumptions in the Thomas et al. 2005 model, such as closed box chemical evolution, a Salpeter slope for the initial

mass function (IMF), or constant SFHs, are too simplistic to be able to explain these observations. Alternatively the adopted SNe yields may not be valid, particularly at high metallicity. Also, t_f may depend not only on $[\alpha/\text{Fe}]$, but also on other parameters such as total metallicity (e.g., Yan et al. 2019).

Moreover, for the case of MRG-M0138, the high α -enhancement is observed simultaneously with a high $[\text{Fe}/\text{H}]$. It is a long-standing problem to reproduce both high metallicities and high $[\alpha/\text{Fe}]$ simultaneously in models, as simply truncating the star formation (e.g., with AGN feedback) produces a high $[\alpha/\text{Fe}]$ but a low $[\text{Fe}/\text{H}]$ (e.g., Okamoto et al. 2017; De Lucia et al. 2017). MRG-M0138 makes this problem even worse, as it has even higher $[\text{Fe}/\text{H}]$ and $[\alpha/\text{Fe}]$ than local galaxies. Simple chemical evolution models that only vary the star-formation timescale, such as the line shown in the lower panel of Figure 3.4, cannot match my measurements. One possible solution to this problem, though not necessarily a unique one, is to alter the initial mass function (IMF): a top-heavy IMF results in more massive stars and therefore more α -elements.

The possible need for a top-heavy IMF in high- z dusty star-forming galaxies has been suggested in some observations and models (e.g., Zhang et al. 2018; Cai et al. 2020). For example, Zhang et al. 2018 inferred a top-heavy IMF based on observations of isotopologue ratios of CO in sub-millimeter galaxies at $z \sim 2-3$. These dusty, highly star-forming galaxies are plausible progenitors of massive quiescent galaxies at $z \sim 2$ like MRG-M0138. However, the CO ratios are sensitive to the rotation speeds of massive stars, which depend on metallicity and possibly on ISM properties in ways that are not well understood Romano et al. 2019. The stellar abundance pattern I have measured may provide a complementary

diagnostic of the high-mass IMF, but detailed galactic chemical evolution modeling is needed to derive such constraints and assess their robustness. I plan to perform such modeling in future work.

In summary, MRG-M0138 is a massive, disk-dominated quiescent galaxy with a formation redshift of $z_{\text{form}} \sim 3.3$. The star formation history of this galaxy seems to have been very short across the whole disk, based on the uniformly high [Mg/Fe], though star formation may have begun earlier in the central regions based on the marginal detection of a negative [Fe/H] gradient. Quantitatively reproducing the high [Mg/Fe] of this galaxy, especially coupled with its high [Fe/H], is challenging and may require alterations to standard galactic chemical evolution models such as a top-heavy IMF. The fact that MGR-M0138 has distinct chemical abundances from local analogs and also from its only well-studied counterpart at $z \sim 2$, COSMOS-11494, motivates the need for deep spectroscopy of a larger sample of high- z quiescent galaxies, which will become feasible with next-generation facilities such as *JWST* and 30-m class telescopes.

Chapter 4

The stellar populations and star formation histories of quiescent galaxies at $z \sim 2$

4.1 Introduction

Despite significant advances made towards understanding galaxy formation and evolution, there are still many fundamental questions that remain unanswered. Among them is the process of galaxy quenching that can be studied from different perspectives using different probes and galaxy populations. To address this question, one needs to rebuild the formation history of quiescent galaxies. One way to explore this is to investigate their stellar chemical abundance using diagnostics such as α -enhancement (α -element-to-iron ratio, $[\alpha/\text{Fe}]$) which is a widely used diagnostic. $[\alpha/\text{Fe}]$ is believed to be sensitive to the

star formation timescale because core-collapse supernovae (SN) produce mostly α -elements (e.g., oxygen, magnesium, silicon, etc. Woosley and Weaver 1995) in a short timescale whereas longer lived SN Type Ia mostly release iron peak elements. This diagnostic has been extensively used to deduce the star formation history (SFH) of local early-type galaxies (ETGs) (e.g., Thomas et al. 2003b; Greene et al. 2019).

However, galaxies undergo minor and major mergers throughout their history, therefore by only studying old quiescent galaxies which their mergers history is not fully understood, we could have a biased view of the star formation and quenching mechanisms. This suggests that we need to also look at quiescent galaxies at high redshifts around the time they experienced quenching. However, these systems are rare, and hard to observe with current instruments due to being compact and faint. In fact, to this date, there are only two quiescent galaxies at $z \sim 2$ for which α -enhancement and iron abundance have been measured precisely (~ 0.1 dex precision): COSMOS-11494 (Kriek et al. 2016), and MRG-M0138 (Jafariyazani et al. 2020). The latter is the brightest quiescent galaxy detected in the near infrared (NIR) thanks to the power of strong gravitational lensing. This galaxy was among a unique sample of five lensed, massive, quiescent systems at $1.95 < z < 2.64$ found by Newman et al. (2018a). COSMOS-11494 and MRG-M0138 both had unusual abundances compared to their local counterparts and specifically their very high $[\text{Mg}/\text{Fe}]$ (0.59 ± 0.11 for COSMOS-11494 and 0.51 ± 0.05 for MRG-M0138), suggested a very short formation timescale based on simple chemical evolution models. Therefore, understanding the typical stellar chemical composition of this population of galaxies requires more observations and possibly modified models.

In this chapter, I first investigate the stellar population of the other four high- z quiescent galaxies introduced in Newman et al. 2018a. Given that these are strongly lensed systems, we can also measure the age, $[\alpha/\text{Fe}]$ and $[\text{Fe}/\text{H}]$ gradients for three of these galaxies which put further constraints on their evolutionary path. Also, I further investigate the evolutionary path of these galaxies with a complementary approach. This technique is to reconstruct the formation histories of galaxies by fitting stellar population synthesis models to their multi-band photometric and/or spectroscopic data (see Conroy 2013 for a comprehensive review). This is also a widely used method to study star formation histories at different redshifts; however, at higher redshifts, we face the challenge of extending spectroscopic observations to near-infrared wavelengths (e.g., Pacifici et al. 2016; Belli et al. 2019; Akhshik et al. 2020; Estrada-Carpenter et al. 2020). For this work, I recover the star formation history of the galaxies in the sample by taking advantage of fitting their photometry and spectra simultaneously using Prospector (Johnson et al. 2019; Leja et al. 2017; Foreman-Mackey et al. 2013). This will enable us to investigate whether the star formation timescales suggested by stellar abundances are consistent with the reconstructed star formation histories.

The chapter is organized as follows. In Section 4.2 I briefly describe my data. In Section 4.3 I explain the procedure and assumptions to measure chemical abundances from spectra and present my measurements. Section 4.4 presents spatially resolved chemical abundance measurements and Section 4.5 describes the reconstruction of star formation histories. I discuss my results and their implication in Section 4.6. I assume a flat Λ CDM cosmology with $\Omega_m = 0.3$, $\Omega_\Lambda = 0.7$ and $H_0 = 70 \text{ km s}^{-1}$.

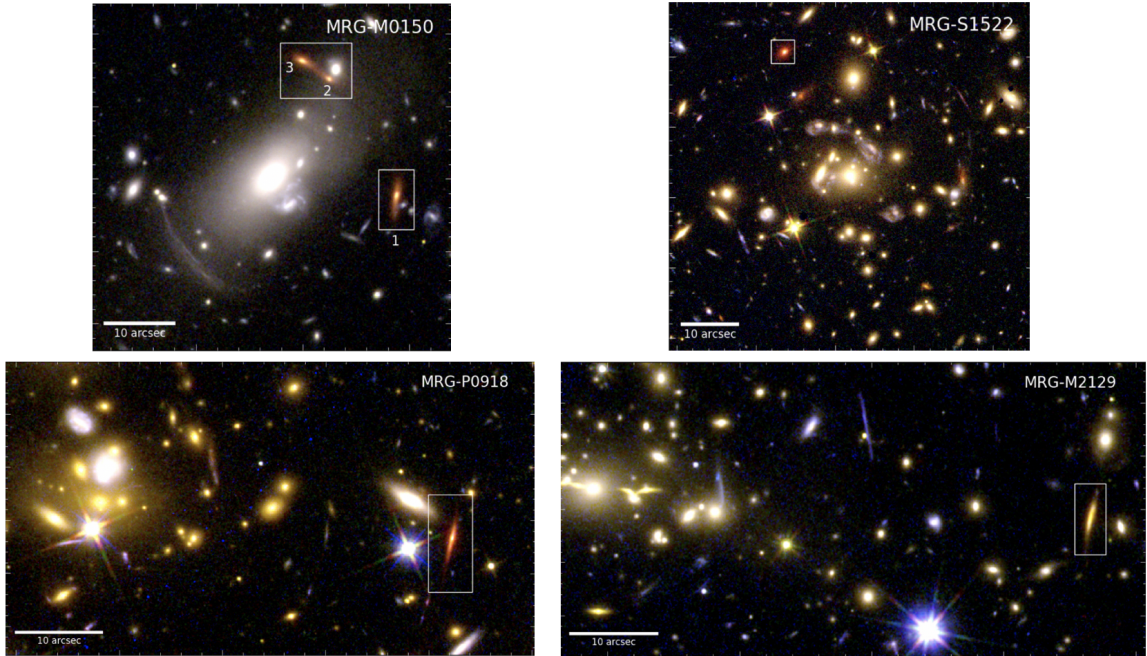


Figure 4.1: Composite *HST* images of the four galaxies in the sample. The lensed quiescent galaxies are shown in boxes. MRG-M0150 has multiple images which are numbered. The images are adopted from Newman et al. 2018a.

4.2 Data

In chapter 3 (Jafariyazani et al. 2020), I presented a comprehensive study of MRG-M0138 using Keck/MOSFIRE (McLean et al. 2010, 2012) and Magellan/FIRE (Simcoe et al. 2013) spectra. In this chapter, I investigate the stellar chemical abundances, their gradient and the star formation history of four other lensed galaxies which are shown in Figure 4.1 (MRG-2129, MRG-M0150, MRG-P0918 and MRG-S1522; Newman et al. 2018a). The full description of observation of each galaxy and their lensing configurations were presented in Newman et al. 2018a. These galaxies have been observed with a variety of ground and

Instrument	Filter	AB Magnitude
MRG-M0150		
WFPC2	F606W	23.89 ± 0.16
ACS	F814W	22.87 ± 0.06
WFC3-IR	F110W	21.52 ± 0.04
WFC3-IR	F125W	21.17 ± 0.03
WFC3-IR	F140W	20.43 ± 0.03
WFC3-IR	F160W	19.90 ± 0.03
FourStar	J	21.27 ± 0.08
FourStar	H	19.63 ± 0.06
FourStar	K _s	19.16 ± 0.06
IRAC	Ch. 1	18.79 ± 0.07
IRAC	Ch. 2	18.33 ± 0.06
MRG-M2129		
ACS	F435W	25.13 ± 0.74
ACS	F475W	24.53 ± 0.29
ACS	F555W	24.53 ± 0.21
ACS	F606W	24.16 ± 0.22
ACS	F625W	23.91 ± 0.23
ACS	F775W	23.22 ± 0.15
ACS	F814W	23.16 ± 0.08
ACS	F850LP	22.55 ± 0.13
WFC3-IR	F105W	21.90 ± 0.05
WFC3-IR	F110W	21.14 ± 0.04
WFC3-IR	F125W	20.78 ± 0.03
WFC3-IR	F140W	20.31 ± 0.03
WFC3-IR	F160W	20.06 ± 0.03
FourStar	K _s	19.59 ± 0.06
IRAC	Ch. 1	19.11 ± 0.05
IRAC	Ch. 2	19.02 ± 0.05
MRG-P0918		
ACS	F555W	23.59 ± 0.14
ACS	F814W	22.36 ± 0.05
WFC3-IR	F105W	21.41 ± 0.04
WFC3-IR	F160W	19.54 ± 0.03
FourStar	J ₁	21.22 ± 0.09
FourStar	J ₂	20.87 ± 0.08
FourStar	J ₃	20.38 ± 0.08
FourStar	H	19.36 ± 0.06
FourStar	K _s	19.17 ± 0.06
IRAC	Ch. 1	19.05 ± 0.07
MRG-S1522		
WFC3-UVIS	F606W	23.91 ± 0.05
LDSS	z	22.65 ± 0.12
WFC3-IR	F105W	21.95 ± 0.04
WFC3-IR	F160W	19.96 ± 0.03
FourStar	J ₁	21.80 ± 0.07
FourStar	J ₂	21.64 ± 0.08
FourStar	J ₃	20.90 ± 0.09
FourStar	H	19.75 ± 0.06
FourStar	K _s	19.41 ± 0.06
IRAC	Ch. 1	19.14 ± 0.06
IRAC	Ch. 2	18.99 ± 0.06

Table 4.1: Available photometric data for galaxies in my sample. Total fluxes for MRG-M0150 are normalized to its Image 1. Data are adopted from Newman et al. 2018a.

	Instrument	Exposure time (Hour)	Slit position angle (Degree)	Seeing (Arcsecond)
MRG-M2129	Magellan/FIRE	16.7	-13	49
MRG-M0150	Magellan/FIRE	6.5	-7.5	55
MRG-P0918	Magellan/FIRE	7	176	42
MRG-S1522	Magellan/FIRE	9	136	57

Table 4.2: Spectroscopic observation information for galaxies in my sample, adopted from Newman et al. 2018a. Spectrum of MRG-M0150 is from its Image 1.

space based instruments in optical and NIR wavelength. Table 4.1 lists all photometric measurements, and Table 4.2 presents information about their spectroscopic observations.

In summary, I use Magellan/FIRE spectra of these galaxies to infer their stellar chemical abundances, and all the available photometric bands to simultaneously fit the spectra and photometry. I also have resolved spectra in a series of five bins along the slit for three of these galaxies (MRG-S1522 is unresolved). I use these spatially resolved data to infer age and metallicity gradients across these objects (see Newman et al. 2018b for details about resolved spectra).

In section 4.5, I also reconstruct star formation history for MRG-M0138 which its detailed chemical abundances were presented in Chapter 3. For this galaxy, I use its Keck/MOSFIRE spectroscopy (presented in previous chapter) along with its multi-band photometric measurements which are shown in Table 4.3.

Instrument	Filter	AB Magnitude
MRG-M0138		
ACS	F555W	22.26 ± 0.20
LDSS	g	22.61 ± 0.19
LDSS	r	21.49 ± 0.15
LDSS	i	20.80 ± 0.13
LDSS	z	19.64 ± 0.12
WFC3-IR	F105W	18.93 ± 0.04
WFC3-IR	F160W	17.28 ± 0.03
FourStar	J ₁	19.06 ± 0.07
FourStar	J ₂	18.40 ± 0.07
FourStar	J ₃	17.76 ± 0.06
FourStar	H	17.08 ± 0.06
FourStar	K _s	16.67 ± 0.06
IRAC	Ch. 1	16.21 ± 0.05
IRAC	Ch. 2	16.00 ± 0.05

Table 4.3: Photometric data for MRG-M0138. Total fluxes are normalized to its Image 1.

Data are adopted from Newman et al. 2018a.

4.3 Chemical abundances

To infer stellar chemical abundances, I fit models to the spectra using `alf` (Conroy and van Dokkum 2012; Conroy et al. 2018) consistent with my previous work on MRG-M0138 (chapter 3 of this thesis, Jafariyazani et al. 2020). `Alf` is a full spectral fitting code which uses Markov Chain Monte Carlo (MCMC) algorithm to fit the spectra to empirical and synthetic stellar libraries (Sánchez-Blázquez et al. 2006; Choi et al. 2016; Villaume et al. 2017). It can be run in three different modes depending on the quality of data and the number of desired output parameters. Although these spectra do not have sufficient signal-to-noise (S/N) to constrain all the parameters included in the full fitting mode, I choose this mode for this analysis to take into account the emission lines and re-scale errors by a jitter term, which is only available in this mode. Re-scaling errors for near-infrared data, where systematic errors associated with the data reduction process are significant, ensure that errors are realistic.

Table 4.4: Age, [Mg/Fe] and [Fe/H] derived from alf

	Age (Gyr)	[Mg/Fe]	[Fe/H]
MRG-M2129	1.05 ± 0.2	0.58 ± 0.21	-0.29 ± 0.21
MRG-M0150	1.28 ± 0.34	N/A*	-0.56 ± 0.33
MRG-P0918	0.65 ± 0.07	0.40 ± 0.15	-0.49 ± 0.12
MRG-S1522	1.08 ± 0.17	0.19 ± 0.23	-0.62 ± 0.22

*Mg b lines are not covered in the spectra of this galaxy to ensure a reliable [Mg/Fe] measurement.

Basic assumptions are a Kroupa Initial Mass Function (IMF, Kroupa 2001) and the following range for the stellar abundance of individual elements: $-0.3 < [X/H] < +1$. My final results are based on a single age population model; however, I also performed the fit assuming a two component star formation history model, and the resulting values showed convergence to a single component model and therefore did not change desired output parameters significantly.

My results including measured age, [Mg/Fe] and [Fe/H] and their uncertainties are listed in Table 4.4. I did not include the [Mg/Fe] measurement for MRG-M0150 in my analysis since its spectra does not cover magnesium b lines (Mg b at 5167, 5172 and 5183 Å). Also, I caution that the lower limit of age in stellar population models is 1 Gyr, and for ages between 0.5 to 1 Gyr, the models are extrapolated to estimate the age. Therefore, the uncertainties for ages below 1 Gyr are underestimated, which is the case for MRG-P0918, the youngest galaxy in the sample, with the estimated age of 0.65 ± 0.07 Gyr.

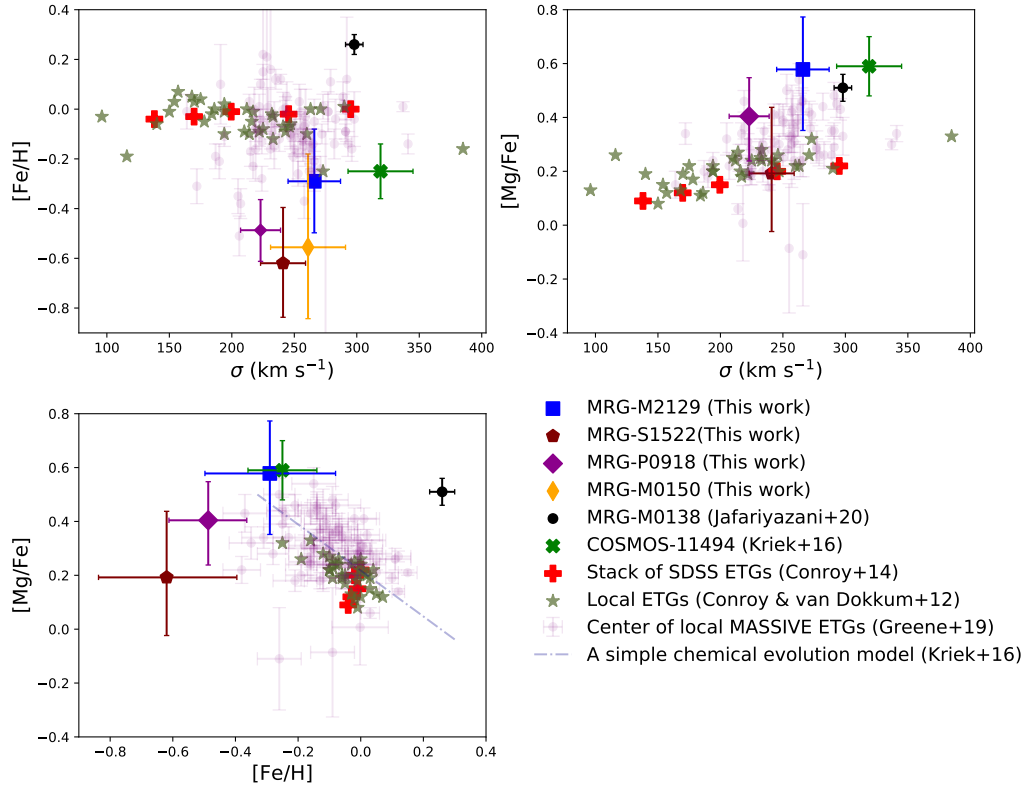


Figure 4.2: Abundance patterns of high- z quiescent galaxies compared to local counterparts. Top left: $[\text{Fe}/\text{H}]$ versus velocity dispersion (σ), top right: $[\text{Mg}/\text{Fe}]$ versus velocity dispersion, lower left: $[\text{Mg}/\text{Fe}]$ versus $[\text{Fe}/\text{H}]$. High- z quiescent galaxy sample include 4 galaxies from this work: MRG-M2129 (blue square), MRG-S1522 (maroon pentagon), MRG-M0918 (purple diamond) and MRG-M0150 (yellow-thin diamond, with only $[\text{Fe}/\text{H}]$ measured due to lack of Mg-line in its spectrum), two galaxies from the literature: MRG-M0138 (black circle; Jafariyazani et al. 2020) and COSMOS-11494 (green filled-x; Kriek et al. 2016). Local sample include local ETGs from Conroy and van Dokkum 2012 (green stars), stacks of SDSS ETGs (red pluses; Conroy et al. 2014) and centers of local MASSIVE ETGs (light purple circles; Greene et al. 2019).

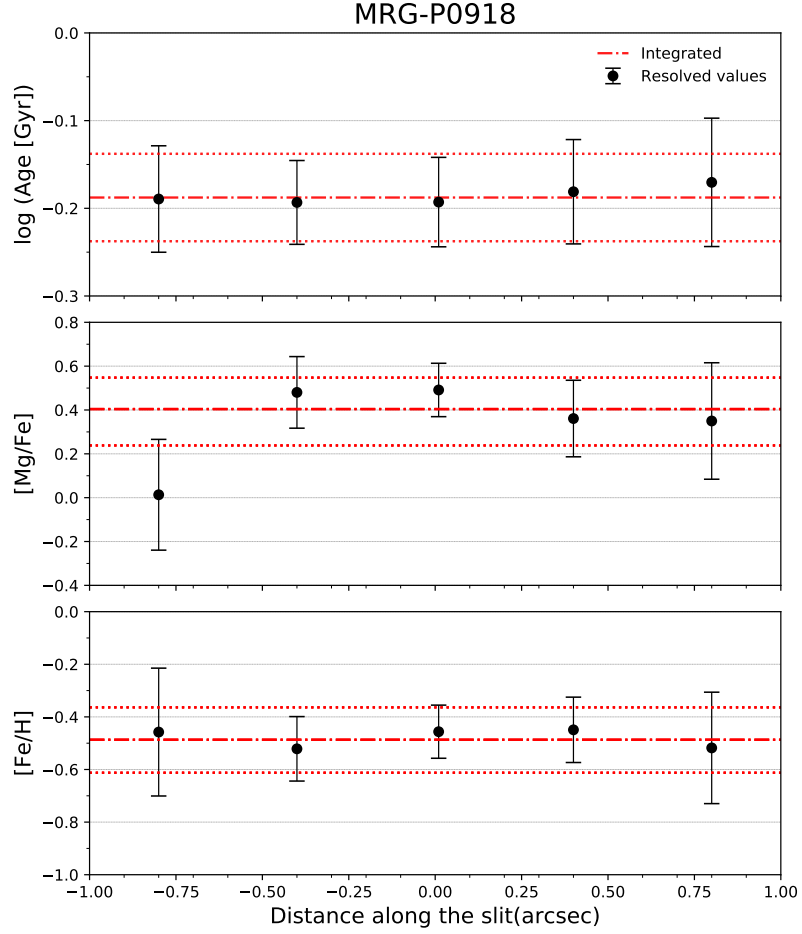


Figure 4.3: Stellar population gradients for MRG-P0918. Red dash-dotted lines are based on the integrated spectra, and red dotted lines represent their 1σ errorbar. Physical radius cannot be measured for this galaxy due to lack of lens model. There is no detectable gradient in age, $[\text{Mg}/\text{Fe}]$ and $[\text{Fe}/\text{H}]$ in this galaxy.

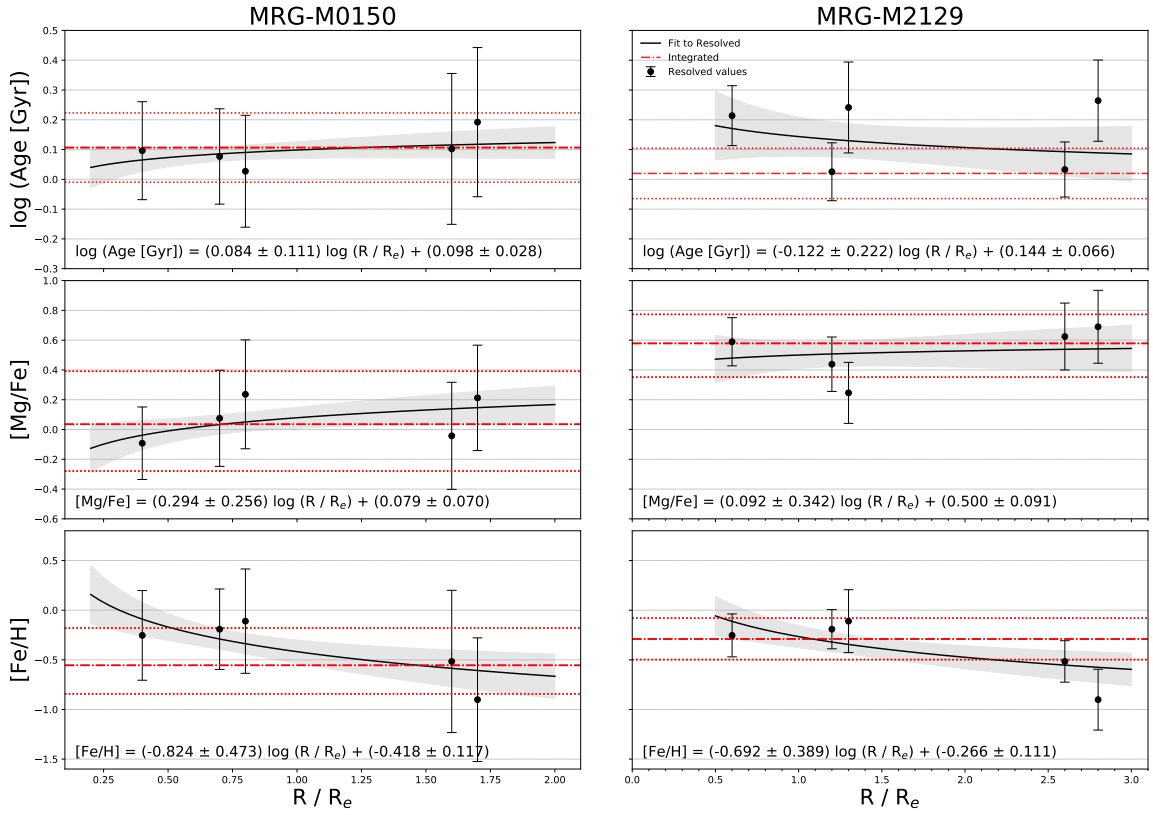


Figure 4.4: Stellar population gradients for MRG-M0150 and MRG-M2129. Red dash-dotted lines are based on the integrated spectra, and red dotted lines represent their 1σ errorbar. Solid black lines and their surrounding shaded regions are the fit to the resolved data in the form of $A \times \log(R/R_e) + B$, where A and B are presented in each panel. Both galaxies show a relatively flat age and $[\text{Mg/Fe}]$ gradients and a negative $[\text{Fe/H}]$ gradient.

Figure 4.2 compares these new measurements with the existing data for the only two counterparts of these galaxies (COSMOS-11494, Kriek et al. 2016 and MRG-M0138, Jafariyazani et al. 2020) at $z \sim 2$ as well with three different samples of local early-type galaxies from Conroy and van Dokkum (2012); Conroy et al. (2014) and Greene et al. (2019). The top panels show $[\text{Fe}/\text{H}]$ and $[\text{Mg}/\text{Fe}]$ values versus velocity dispersion (σ). In agreement with previous works, $[\text{Fe}/\text{H}]$ does not tend to have a strong dependence on velocity dispersion, but $[\text{Mg}/\text{Fe}]$ has a positive correlation with velocity dispersion in local galaxies (e.g., Trager et al. 2000b,a; Johansson et al. 2012). All of these 4 galaxies have low $[\text{Fe}/\text{H}]$ even compared to local ETGs, consistent with low metallicity of COSMOS-11494 but completely different from the high $[\text{Fe}/\text{H}]$ of MRG-M0138. On the $[\text{Mg}/\text{Fe}]$ vs. σ parameter space, MRG-M2129 and MRG-P0918 are similar to both of their $z \sim 2$ counterparts and are Mg-enhanced even compared to the local ETG populations. MRG-S1522 is also considered to be Mg-enhanced but with a value more comparable to its local counterparts with similar velocity dispersion; however, its large errorbar makes the interpretation hard.

These measurements confirm that high- z quiescent galaxies have high $[\text{Mg}/\text{Fe}]$ and low $[\text{Fe}/\text{H}]$ relative to local ETGs with comparable velocity dispersion. The high $[\text{Mg}/\text{Fe}]$ values can be indicative of a short formation timescale of ~ 0.1 Gyr according to common closed box chemical evolution models where short-lived core-collapse SN produced most of α -elements, but longer lived SN Type Ia were not yet able to increase the iron abundance in the galaxy (Thomas et al. 2005; Kriek et al. 2016). In Section 4.5, I will evaluate this statement by reconstructing the star formation history of the present sample by fitting stellar population models to their spectra and their multi-band photometry.

4.4 Stellar Population Gradients

I follow the same procedure as for integrated spectra to measure the spatially resolved age, [Mg/Fe] and [Fe/H] for three out of four galaxies in the sample. MRG-S1522 has not a resolved spectra and therefore is omitted for this part of the analysis. Also, we do not have a lens model for MRG-P0918 due to unknown redshift of the lensing cluster, and therefore I report its gradients as a function of distance along the spectroscopy slit instead of the physical radius which is shown in Figure 4.3. I fit the radial gradients in MRG-M0150 and MRG-2129 with a functional form of $A \times \log (R/R_e) + B$ which are presented in Figure 4.4.

Interestingly, I do not detect any significant age gradient or a gradient in [Mg/Fe] similar to what I found for MRG-M0138 which is consistent with a fairly uniform stellar mass assembly history across these galaxies. I find a negative [Fe/H] gradient for MRG-M0150 and MRG-M2129 and although I am not able to quantify the gradient for MRG-P0918 due to lack of lens model, it seems to have a flat [Fe/H] profile. A nearly flat metallicity gradient suggests the presence of efficient feedback mechanisms during the star-forming phase which redistribute the metals produced in central regions towards the external region of the galaxy. Nevertheless, a significant negative metallicity gradient is consistent with more conservative feedback models (e.g., Pilkington et al. 2012; Gibson et al. 2013; Ma et al. 2017).

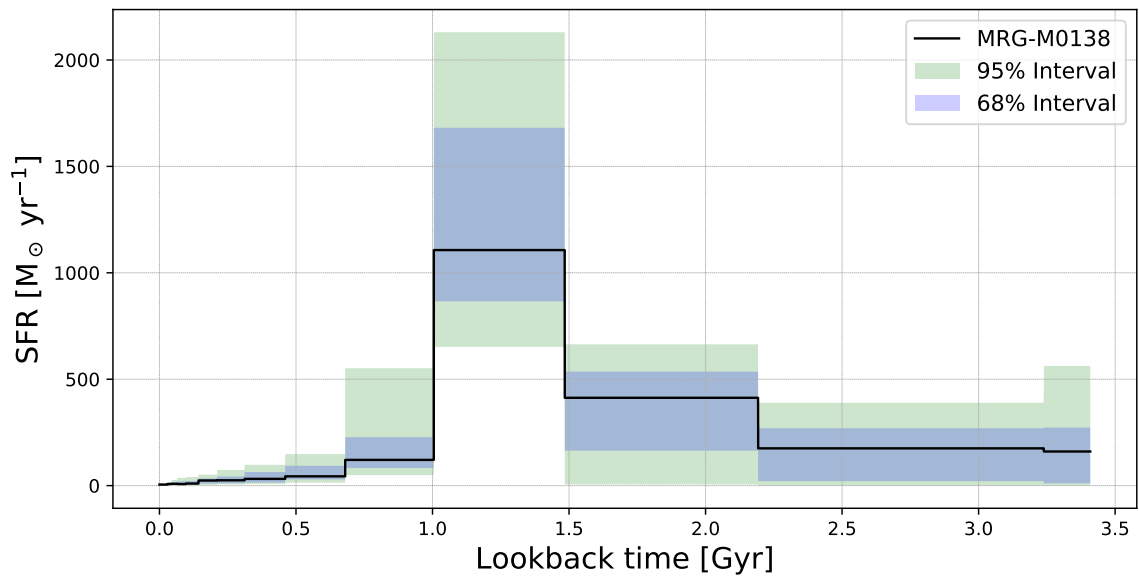


Figure 4.5: Reconstructed star formation history for MRG-M0138. Best-fit SFH model as well as the 68% and 95% Bayesian credible intervals derived from posterior distributions are presented. SFRs are demagnified by a factor of 12.5, derived from its constructed lens model.

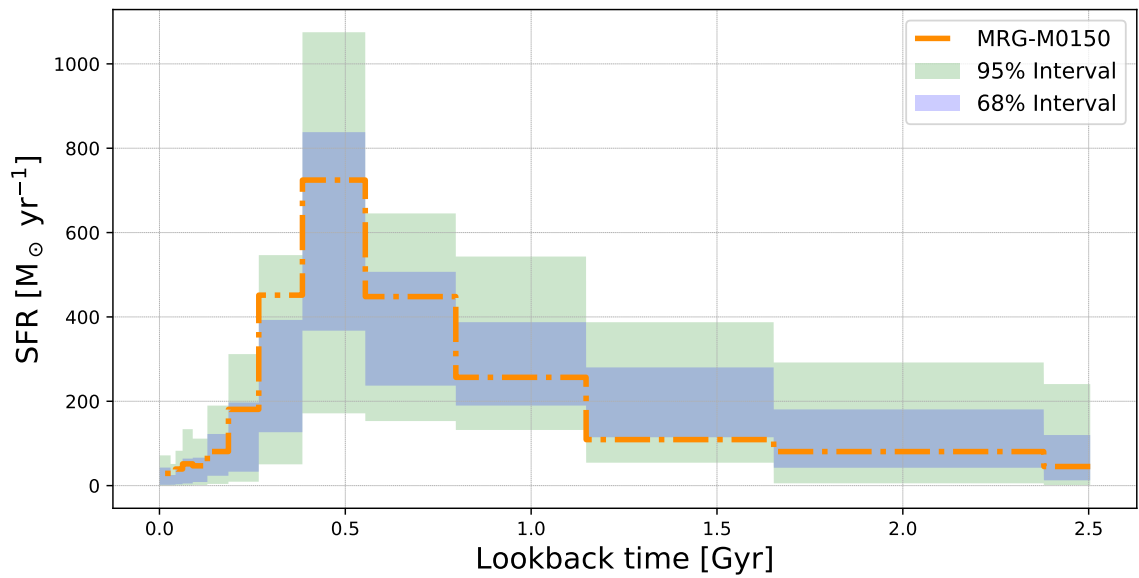


Figure 4.6: Reconstructed star formation history for MRG-M0150. Best-fit SFH model as well as the 68% and 95% Bayesian credible intervals derived from posterior distributions are presented. SFRs are demagnified by a factor of 4.4, derived from its constructed lens model.

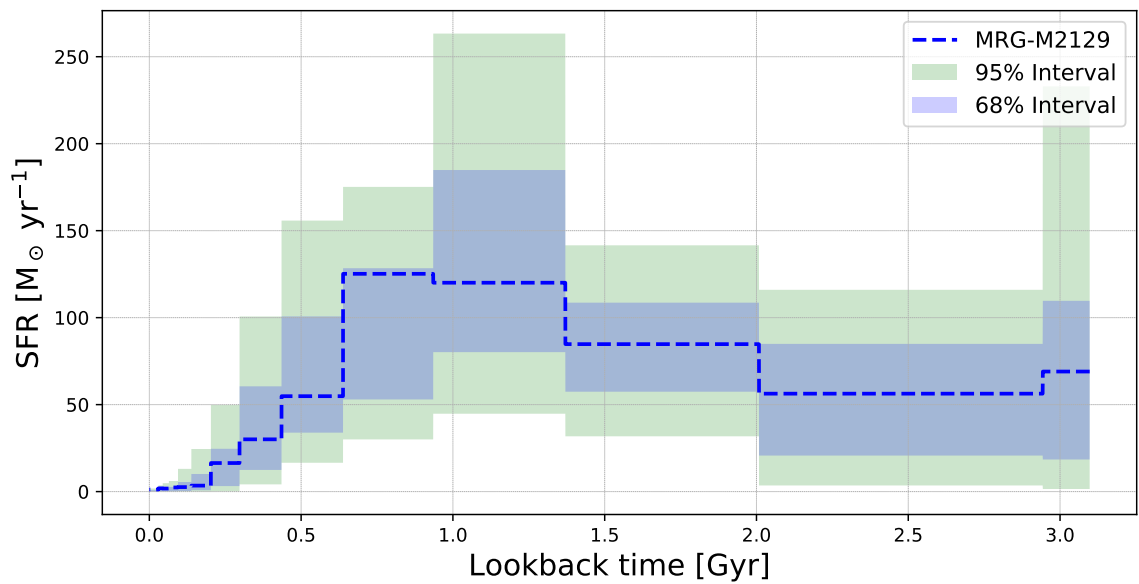


Figure 4.7: Reconstructed star formation history for MRG-M2129. Best-fit SFH model as well as the 68% and 95% Bayesian credible intervals derived from posterior distributions are presented. SFRs are demagnified by a factor of 4.4, derived from its constructed lens model.

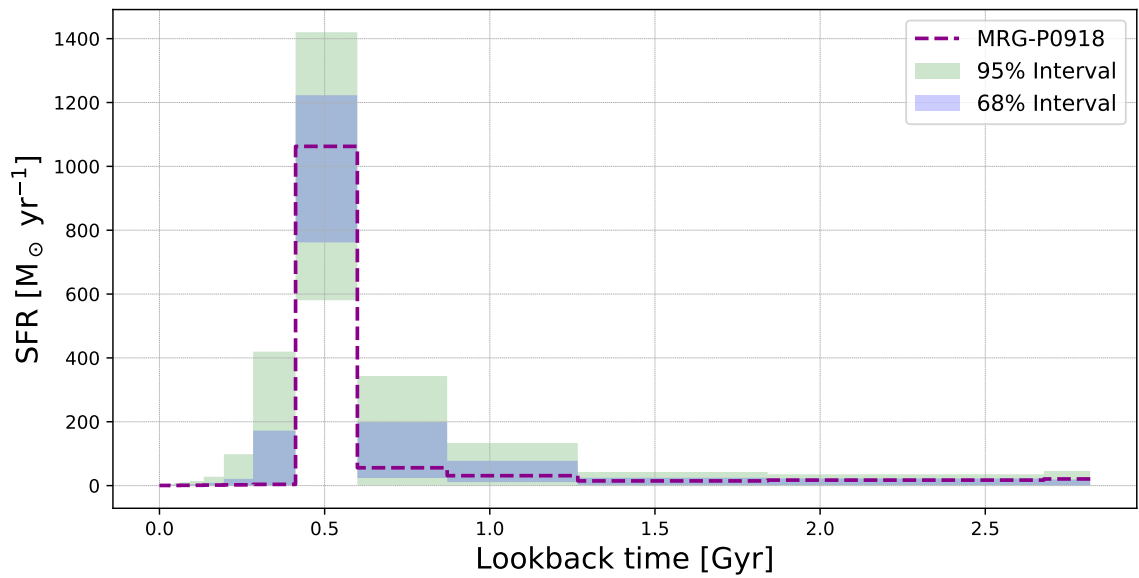


Figure 4.8: Reconstructed star formation history for MRG-P0918. Best-fit SFH model as well as the 68% and 95% Bayesian credible intervals derived from posterior distributions are presented. SFRs are demagnified by a fiducial magnification factor of 4 due to lack of lens model.

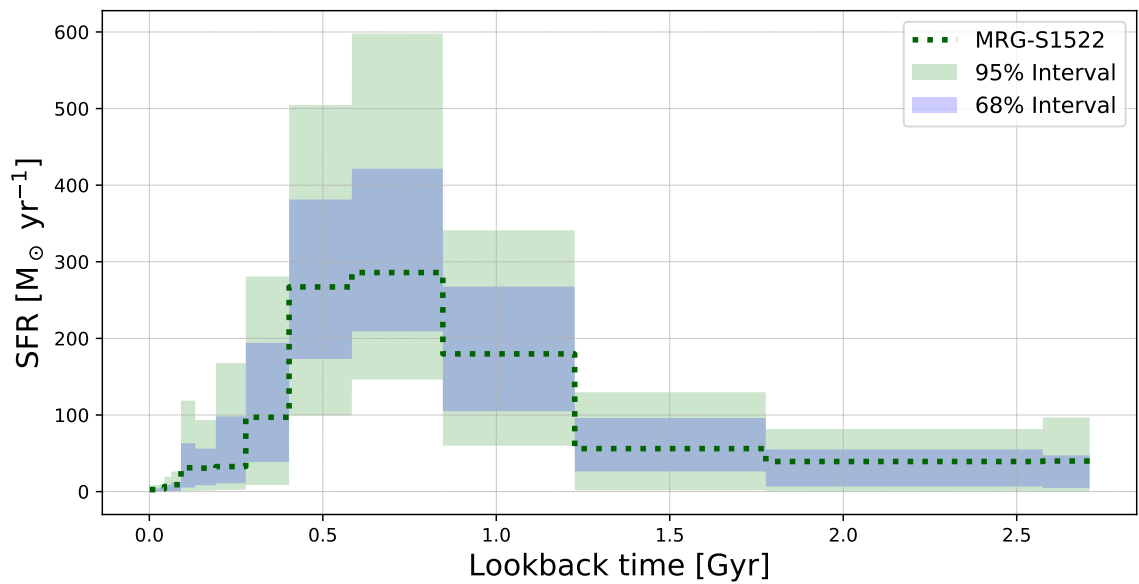


Figure 4.9: Reconstructed star formation history for MRG-S1522. Best-fit SFH model as well as the 68% and 95% Bayesian credible intervals derived from posterior distributions are presented. SFRs are demagnified by a fiducial magnification factor of 4 due to lack of lens model.

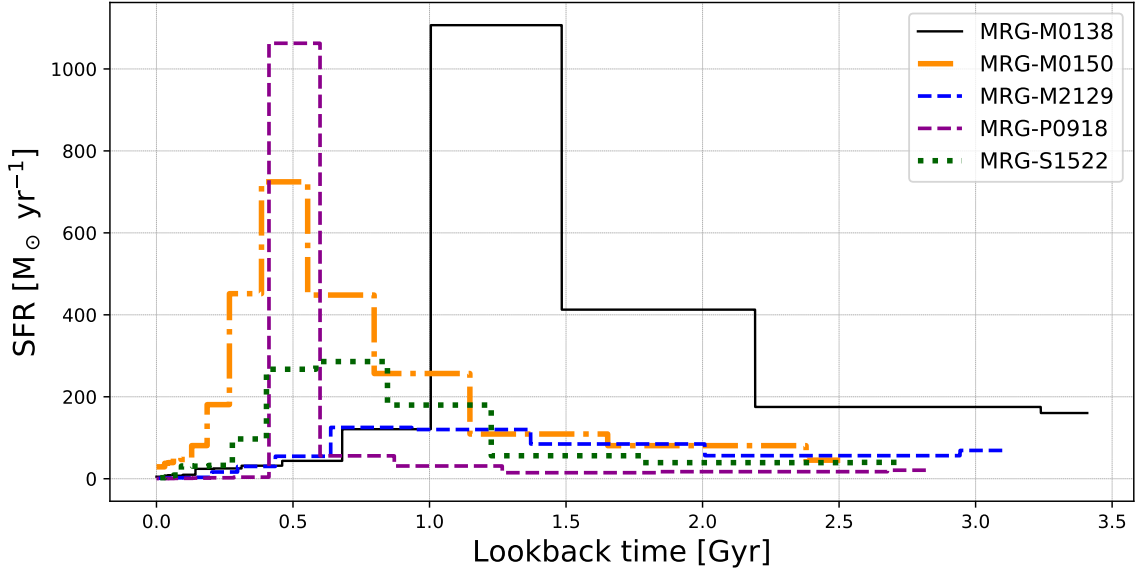


Figure 4.10: Reconstructed star formation histories of all galaxies in the sample. All SFRs are demagnified as described in above figures.

4.5 Star Formation Histories

To better understand the formation processes of these galaxies, we infer their star formation histories by fitting synthetic templates to their spectra and all of their available photometric data (mentioned in section 4.2) simultaneously. Our templates are from the Flexible Stellar Population Synthesis library (FSPS; Conroy et al. 2009; Conroy and Gunn 2010). The fitting process is done by running Prospector (Foreman-Mackey et al. 2013; Johnson et al. 2019, 2021), a fully Bayesian framework to infer stellar population properties from photometric and/or spectroscopic data, together with dynesty (Speagle 2020) which is a nested sampling package to sample the multi-dimensional parameter space efficiently. An important feature of this tool is its flexible spectroscopic calibration model which allows combining photometric and spectroscopic data from infrared to ultraviolet with taking into

account the spectrophotometric calibration errors. We use Prospector- α (Leja et al. 2017) for our physical model framework which includes contribution of stars, dust, and systematic effects to the observed emission.

The stellar population properties include redshift, velocity dispersion, mass, metallicity, etc. and a non-parametric star formation history which consists of 14 independent logarithmically spaced age bins. we assume a continuity prior (Leja et al. 2019) to get a smooth behavior in star formation rate (SFR) as a function of time. This prior fits for $\Delta\log(\text{SFR})$ between adjacent time bins and explicitly weights against sharp changes in $\text{SFR}(t)$. For the dust absorption, we use three-parameter model from Kriek and Conroy 2013. In Prospector, we adopted this model by setting a uniform prior between 0 and 3 for `dust2`, a Gaussian prior centered on 0, with $\sigma=0.3$, and clipped at -1.5 and +0.4 for `dust_index`; and a Gaussian prior centered on 0, with $\sigma=0.3$, and clipped at 0 and 2 for `dust1_fraction` (`dust1/dust2`). The polynomial used to remove the continuum has 1 order per 100 rest-frame angstrom. We note that we masked Mg b line in the spectra, where present, as my chemical abundance analysis shows Mg-enhancement in galaxies; however, Mg-enhanced models are not yet included in templates.

The non-parametric star formation histories provide full flexibility to recover possible multi-bursts or rejuvenation episodes. I present reconstructed SFHs for individual galaxies in Figure 4.5 through 4.9 where the best-fit model and the 68% and 95% credible intervals of the SFHs are shown. All SFRs are demagnified with the corresponding magnification factors (μ) adopted from Newman et al. 2018a. Magnification factors are 12.5, 4.5 and 4.4 for MRG-M0138, MRG-M2129 and MRG-M0150 respectively. For MRG-S1522

and MRG-P0918 where lens models could not be constructed, I assume a fiducial μ of 4 for consistency.

Figure 4.10 present the best fit SFH models for all of the galaxies in the sample to enable visual comparison. The resulting star formation histories show a diverse range of distributions. MRG-M0138 and MRG-P0918 had a more bursty star formation activity before quenching, but the star formation history of the other three galaxies are more extended. This is not exactly consistent with my chemical abundance analysis where they suggest a short formation timescale assuming widely used chemical evolution models developed based on local galaxies. To better address this contradiction, I define a star-formation timescale based on the reconstructed SFH as the time takes for the galaxy to increase its stellar mass from 10% to 90% of its total mass ($t_{90\%} - t_{10\%}$).

I present these formation timescales along with metallicity and Mg-abundance and a simple relation based on closed-box chemical evolution models in Figure 4.11. I acknowledge that the definition of the formation timescale in these studies are not the same, but still give us a general framework for comparison. Thomas et al. (2005) used the width of Gaussian star formation histories (Δt) as formation timescale compared to our $t_{90\%} - t_{10\%}$ from non-parametric star formation histories. Thomas et al. (2005) model cannot explain more Mg-enhanced galaxies in this sample. I discuss the implications of these results in the next section.

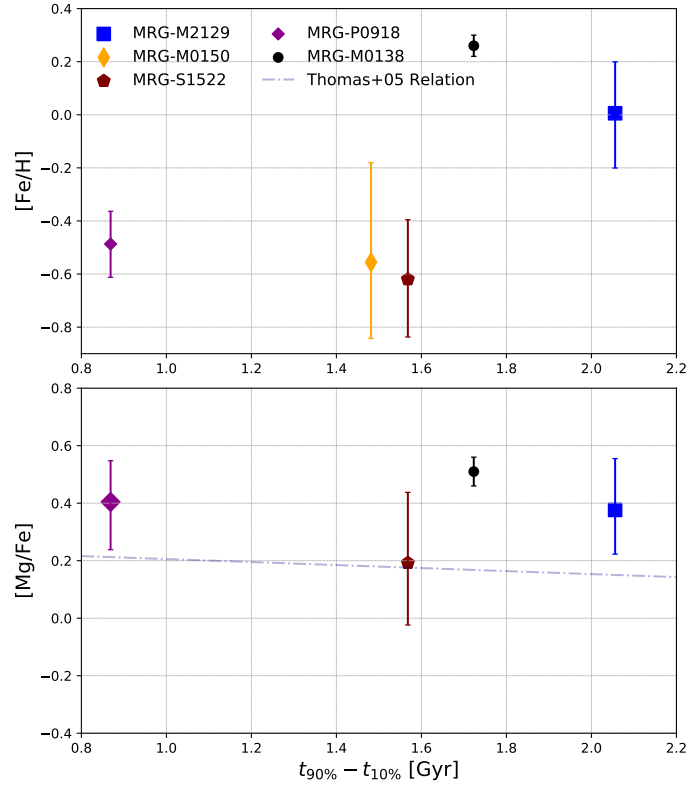


Figure 4.11: Metallicity and Mg-abundance versus star-formation timescale which is defined as the duration of time in which the a galaxy increases its stellar mass from 10% to 90% of its total mass ($t_{90\%} - t_{10\%}$). The grey line represents Thomas et al. 2005 relation between $[\alpha/\text{Fe}]$ and formation timescale. I acknowledge that these two formation timescales are not exactly similar as Thomas et al. 2005 reported the width of Gaussian star formation histories as formation timescale.

4.6 Discussion

In this section, I discuss the implication of my measurements. The measured abundances for the local ETGs can be generally explained by star formation timescales of 1-2 Gyr assuming simple chemical evolution models (e.g., Thomas et al. 2005). For the sample of high- z quiescent galaxies studied here, reconstructed non-parametric star formation histories are consistent with formation timescale of 1-2 Gyr, but surprisingly, the chemical abundances, specifically large Mg-enhancement in some of these galaxies requires lower (and somehow unrealistic) star formation timescales.

In fact, chemical abundances shortly after the quenching do not appear to be consistent with the extended star formation histories computed for these galaxies, at least using a simple chemical evolution model. This could imply the presence of post-quenching merger-driven evolution which would likely affect the locally measured abundances. The abundances of the other two galaxies, MRG-P0918 and MRG-S1522 are comparable to the center of local MASSIVE ETGs with highest Mg-enhancement and lowest [Fe/H] which supports a very short formation timescale that happened before $z \sim 2$. Therefore, these two galaxies could have evolved into today's ETGs with less or even no need for merger-driven evolution. However, we caution that the abundances of the two samples were not measured using the same technique, making the comparison more uncertain.

In either case, these results suggest that coupling SFHs with more elaborate chemical evolution models are needed to explain the evolution of these galaxies more consistently. Such models can constrain different parameters affecting the evolution including different core-collapse supernova yields, different SN Type Ia delay time distributions, slope of the

IMF or inflows (which can lower $[\text{Fe}/\text{H}]$ relative to a closed box model). Specifically, a flatter high-mass slope of the IMF might be required to produce more massive stars and therefore higher α -enhancement in these galaxies.

Chapter 5

Conclusions

5.1 Spatially resolved properties of star-forming galaxies

In the first part of my thesis research (chapter 2 of this thesis, Jafariyazani et al. 2019), I studied the spatially resolved properties of star-forming galaxies at intermediate-redshifts ($0.1 < z < 0.42$) aiming to understand the internal processes which govern their formation and evolution. I investigated the spatial distribution of $H\alpha$ star formation rate ($SFR_{H\alpha}$) and the Balmer decrement (i.e., $H\alpha / H\beta$), using integral field spectroscopic data from the MUSE-Wide Survey. I also derived spatially resolved mass, SFR and dust maps from pixel-by-pixel spectral energy distribution fitting on seven band photometric data from the Cosmic Assembly Near-infrared Deep Extragalactic Legacy Survey (CANDELS).

Combining my spectroscopic and photometric measurements, I measured a significant increase in the median specific ($SFR_{H\alpha}$) from the center to outer radii which implied that inside-out growing is a possible scenario for the evolution of these galaxies. I also found that the radial profile of stellar and nebular color excess is strongly dependent on the inte-

grated specific SFR of the galaxy. Furthermore, I showed that the slope and normalization of the resolved main sequence of star-forming galaxies are highly dependent on the SFR diagnostics (SFR_{SED} vs. $\text{SFR}_{H\alpha}$). Also, the position of different regions of galaxies on this parameter space is determined by the radial distance from the center which suggests that inner parts of the galaxies formed their stars before the outer parts as another piece of evidence for inside-out growth of these galaxies.

In this project, I developed the methodology of studying resolved properties of galaxies with combined photometric and integral field unit spectroscopic data. This opens new avenues for future works including to incorporate the upcoming data from the completed MUSE Wide Survey to build upon this analysis by quadrupling the sample size explored in this work. Furthermore, this methodology can be tuned to address more diverse science questions, for example, to explore gas-phase metallicity distribution and how it is related to the internal physical properties and possibly to the environment of the galaxies.

This is the subject of my new research project where I use photometric data from CANDELS and public data available from 44 out of 100 total fields of MUSE Wide Survey (Urrutia et al. 2019b) to study the gas-phase metallicity distribution in intermediate redshift galaxies ($0.2 < z < 0.9$). This will tell us about the evolutionary path of these galaxies, and enable us to test different growth models in this population. Metallicity distributions are important diagnostics of galaxy evolution, because they record the history of events happened in a galaxy including mergers, gas flows, and star formation activity; however, they are still not well understood even for local galaxies. For example, a recent analysis based on high-resolution observations with MUSE/VLT showed that a simple scenario where

the oxygen abundance distribution of spiral galaxies can be explained with a single negative gradient (e.g. Sánchez-Menguiano et al. 2016) is not a complete picture (Sánchez-Menguiano et al. 2018). But an abundance drop in the inner regions of the discs and flattening in the outer regions are very common in these galaxies which need to be explained. This is an example emphasizing that high spatial-resolution observation of metallicity distribution in galaxies at different epochs are crucial to reveal a complete picture of the evolution of galaxies.

Although we are still limited by the resolution limit of our instruments, and we may not be able to measure metallicity diagnostic emission lines including [OIII], [OII], etc. at resolution scales of the MUSE instrument for a statistically large sample of non-local galaxies, my preliminary analysis showed that by decomposing galaxies into bulge and disk components using *HST* imaging data, I can measure these diagnostic emission lines for each component, for a statistically large sample at $0.2 < z < 0.9$. Also, by measuring stellar mass, SFR, and reddening of these two components from CANDELS data, I would be able to constraint the mass-metallicity and fundamental metallicity relations for bulge and disk components at this redshift range.

Combining spatially resolved photometry and spectroscopy is also very much needed as we are waiting for the JWST and 30-40-meter class telescopes that have resolved galaxy formation studies as one of their key science cases. Investigations based on current facilities will be a pathfinder for such observations and to combine high spatial resolution ground and space-based data to tackle fundamental questions about the growth of galaxies.

5.2 High- z quiescent galaxies

In the second part of my thesis work (chapter 3 and 4, Jafariyazani et al. 2020 & Jafariyazani et al. in prep), I first analyzed, by taking advantage of full spectral fitting, Keck/MOSFIRE and FIRE/Magellan spectra of MRG-M0138, the brightest quiescent galaxy detected at $z \sim 2$ so far. Using this spectra, which the former is by far the highest quality spectrum ever obtained for a high-redshift quiescent galaxy, I performed novel measurements of magnesium-enhancement $[\text{Mg}/\text{Fe}]$ (only the second $[\text{Mg}/\text{Fe}]$ measurement at $z \sim 2$ after COSMOS-11494 (Kriek et al. 2016)), iron abundance $[\text{Fe}/\text{H}]$ and, for the first time, the gradient in each of these abundances. I also measured the stellar abundances of six other elements in this galaxy with 0.1 dex precision.

These measurements show that both MRG-M0138 and COSMOS-11494 are very Mg-enhanced compared to the centers of local massive early type galaxies. These dissimilar abundances between high and low redshift quiescent galaxies suggest that even the inner regions of massive galaxies could have experienced significant mixing of stars in mergers, in contrast to a purely inside-out growth model. More interestingly, MRG-M0138 not only is Mg-enhanced, but also is very iron rich ($[\text{Fe}/\text{H}] = 0.26 \pm 0.04$) in contrast to COSMOS-11494. This points to the long-standing problem of reproducing high metallicities and high $[\alpha/\text{Fe}]$ simultaneously in chemical evolution models. The abundance pattern observed in MRG-M0138 challenges simple galactic chemical evolution models and casts doubt on the accuracy and completeness of our assumptions and models which significantly affect our results but are not yet well understood and indicates the need for more elaborate models.

Additionally, for the first time in a high redshift quiescent galaxy, I measure the age and metallicity gradients thanks to the gravitational lensing. These gradients put further constraints on the formation history of this galaxy and suggest that star formation must have stopped abruptly and relatively uniformly across this system. These detailed information are currently available to us merely due to the power of strong gravitational lensing which gives us spatial resolution needed to study the internal structure of high redshift compact systems. Still, even higher resolution measurements are needed to study the stellar populations of the very center of this galaxy (e.g., bulge) which can offer us the information necessary to test and rule out different quenching scenarios. This can be achieved by future JWST observations which thankfully we have guaranteed time to observe this unique object, MRG-M0138, with the JWST Near Infrared Spectrograph (NIRSpec) and Near Infrared Camera(NIRCam).

The unusual abundances of these two high redshift quiescent galaxies motivated my next project on this interesting population where I investigate the stellar populations and star formation histories of four other high- z lensed quiescent galaxies. By measuring age, $[\text{Mg}/\text{Fe}]$, $[\text{Fe}/\text{H}]$, and gradients in each of these parameters for these galaxies, I found that Mg-enhancement is common in this population, but in contrast to MRG-M0138, all other galaxies in my sample have low $[\text{Fe}/\text{H}]$.

I also reconstruct non-parametric star formation histories for all five galaxies in my sample which shown to have diverse shapes, and they generally have formation timescale of 1-2 Gyr which is inconsistent with very short formation timescales inferred from Mg-enhancement based on closed-box simple chemical evolution models. This inconsistency

between chemical abundances shortly after quenching and extended reconstructed star formation histories could suggest some post-quenching merger-driven evolution that affected the locally measured abundances or the need for modifying simple chemical evolution models to be able to explain this population. In either case, coupling the SFHs with more elaborate chemical evolution models is a key to understanding this population.

These results provoked my ongoing research project which is to model chemical abundances by assuming different star formation histories and adopt different models for parameters affecting them. This enables me to test different models including for core-collapse supernova yields, SN Type Ia delay time distributions, inflows and outflows, and the slope of the IMF. My preliminary results suggest that a flatter high-mass slope of the IMF might be required to produce more massive stars and therefore higher α -enhancement in this population of galaxies to match observations.

On the observational side, we still need more data and larger samples from this population of galaxies. Considering current available facilities, this can be achieved by searching for magnified high redshift quiescent galaxy candidates in recent archival observations of galaxy clusters conducted after 2015 (after the search by Newman et al. 2018a).

Also, in future, the upcoming Euclid (Laureijs et al. 2011) and Nancy Grace Roman surveys (Green et al. 2012) will provide us with thousands of lensed systems, and we will find the unique opportunity to identify and study quiescent galaxies even at spatially resolved scales for statistically large samples of galaxies in the young universe.

This will enable us to understand, for the first time, the true conditions of the early period of intense star formation in massive galaxies close to the epoch of their quenching, before they get polluted by galaxy mergers.

Bibliography

- Akhshik, M., Whitaker, K. E., Brammer, G., Mahler, G., Sharon, K., Leja, J., Bayliss, M. B., Bezanson, R., Gladders, M. D., Man, A., Nelson, E. J., Rigby, J. R., Rizzo, F., Toft, S., Wellons, S., and Williams, C. C. (2020). REQUIEM-2D Methodology: Spatially Resolved Stellar Populations of Massive Lensed Quiescent Galaxies from Hubble Space Telescope 2D Grism Spectroscopy. , 900(2):184.
- Aravena, M., Spilker, J. S., Bethermin, M., Bothwell, M., Chapman, S. C., de Breuck, C., Furstenau, R. M., González-López, J., Greve, T. R., Litke, K., Ma, J., Malkan, M., Marrone, D. P., Murphy, E. J., Stark, A., Strandet, M., Vieira, J. D., Weiss, A., Welikala, N., Wong, G. F., and Collier, J. D. (2016). A survey of the cold molecular gas in gravitationally lensed star-forming galaxies at $z \gtrsim 2$. , 457(4):4406–4420.
- Arnouts, S., Cristiani, S., Moscardini, L., Matarrese, S., Lucchin, F., Fontana, A., and Giallongo, E. (1999). Measuring and modelling the redshift evolution of clustering: the Hubble Deep Field North. , 310:540–556.
- Belfiore, F., Maiolino, R., Bundy, K., Masters, K., Bershady, M., Oyarzún, G. A., Lin, L., Cano-Diaz, M., Wake, D., Spindler, A., Thomas, D., Brownstein, J. R., Drory, N., and Yan, R. (2018). SDSS IV MaNGA - sSFR profiles and the slow quenching of discs in green valley galaxies. , 477:3014–3029.
- Belli, S., Newman, A. B., and Ellis, R. S. (2019). MOSFIRE Spectroscopy of Quiescent Galaxies at $1.5 \lesssim z \lesssim 2.5$. II. Star Formation Histories and Galaxy Quenching. , 874(1):17.
- Bruzual, G. and Charlot, S. (2003). Stellar population synthesis at the resolution of 2003. *Monthly Notices of the Royal Astronomical Society*, 344(4):1000–1028.
- Bundy, K., Bershady, M. A., Law, D. R., Yan, R., Drory, N., MacDonald, N., Wake, D. A., Cherinka, B., Sánchez-Gallego, J. R., Weijmans, A.-M., Thomas, D., Tremonti, C., Masters, K., Cocato, L., Diamond-Stanic, A. M., Aragón-Salamanca, A., Avila-Reese, V., Badenes, C., Falcón-Barroso, J., Belfiore, F., Bizyaev, D., Blanc, G. A., Bland-Hawthorn, J., Blanton, M. R., Brownstein, J. R., Byler, N., Cappellari, M., Conroy, C., Dutton, A. A., Emsellem, E., Etherington, J., Frinchaboy, P. M., Fu, H., Gunn, J. E., Harding, P., Johnston, E. J., Kauffmann, G., Kinemuchi, K., Klaene, M. A., Knapen, J. H., Leauthaud, A., Li, C., Lin, L., Maiolino, R., Malanushenko, V., Malanushenko, E.,

- Mao, S., Maraston, C., McDermid, R. M., Merrifield, M. R., Nichol, R. C., Oravetz, D., Pan, K., Parejko, J. K., Sanchez, S. F., Schlegel, D., Simmons, A., Steele, O., Steinmetz, M., Thanjavur, K., Thompson, B. A., Tinker, J. L., van den Bosch, R. C. E., Westfall, K. B., Wilkinson, D., Wright, S., Xiao, T., and Zhang, K. (2015). Overview of the SDSS-IV MaNGA Survey: Mapping nearby Galaxies at Apache Point Observatory. , 798:7.
- Cai, Z.-Y., Zotti, G. D., and Bonato, M. (2020). High-z Dusty Star-forming Galaxies: A Top-heavy Initial Mass Function? , 891(1):74.
- Calzetti, D. (1997). Reddening and Star Formation in Starburst Galaxies. , 113:162–184.
- Calzetti, D., Armus, L., Bohlin, R. C., Kinney, A. L., Koornneef, J., and Storchi-Bergmann, T. (2000). The Dust Content and Opacity of Actively Star-forming Galaxies. , 533:682–695.
- Casey, C. M., Narayanan, D., and Cooray, A. (2014a). Dusty star-forming galaxies at high redshift. , 541(2):45–161.
- Casey, C. M., Scoville, N. Z., Sanders, D. B., Lee, N., Cooray, A., Finkelstein, S. L., Capak, P., Conley, A., De Zotti, G., Farrah, D., Fu, H., Le Floch, E., Ilbert, O., Ivison, R. J., and Takeuchi, T. T. (2014b). Are Dusty Galaxies Blue? Insights on UV Attenuation from Dust-selected Galaxies. , 796:95.
- Chabrier, G. (2003). Galactic stellar and substellar initial mass function. *Publications of the Astronomical Society of the Pacific*, 115(809):763.
- Charlot, S. and Fall, S. M. (2000). A Simple Model for the Absorption of Starlight by Dust in Galaxies. , 539:718–731.
- Choi, J., Dotter, A., Conroy, C., Cantiello, M., Paxton, B., and Johnson, B. D. (2016). Mesa Isochrones and Stellar Tracks (MIST). I. Solar-scaled Models. , 823(2):102.
- Conroy, C. (2013). Modeling the Panchromatic Spectral Energy Distributions of Galaxies. , 51:393–455.
- Conroy, C., Graves, G. J., and van Dokkum, P. G. (2014). Early-type Galaxy Archeology: Ages, Abundance Ratios, and Effective Temperatures from Full-spectrum Fitting. , 780(1):33.
- Conroy, C. and Gunn, J. E. (2010). The Propagation of Uncertainties in Stellar Population Synthesis Modeling. III. Model Calibration, Comparison, and Evaluation. , 712(2):833–857.

- Conroy, C., Gunn, J. E., and White, M. (2009). The Propagation of Uncertainties in Stellar Population Synthesis Modeling. I. The Relevance of Uncertain Aspects of Stellar Evolution and the Initial Mass Function to the Derived Physical Properties of Galaxies. , 699(1):486–506.
- Conroy, C. and van Dokkum, P. (2012). Counting Low-mass Stars in Integrated Light. , 747(1):69.
- Conroy, C., Villaume, A., van Dokkum, P. G., and Lind, K. (2018). Metal-rich, Metal-poor: Updated Stellar Population Models for Old Stellar Systems. , 854(2):139.
- Croom, S. M., Lawrence, J. S., Bland-Hawthorn, J., Bryant, J. J., Fogarty, L., Richards, S., Goodwin, M., Farrell, T., Mizziarski, S., Heald, R., Jones, D. H., Lee, S., Colless, M., Brough, S., Hopkins, A. M., Bauer, A. E., Birchall, M. N., Ellis, S., Horton, A., Leon-Saval, S., Lewis, G., López-Sánchez, Á. R., Min, S.-S., Trinh, C., and Trowland, H. (2012). The Sydney-AAO Multi-object Integral field spectrograph. , 421:872–893.
- Dalcanton, J. J., Williams, B. F., Lang, D., Lauer, T. R., Kalirai, J. S., Seth, A. C., Dolphin, A., Rosenfield, P., Weisz, D. R., Bell, E. F., Bianchi, L. C., Boyer, M. L., Caldwell, N., Dong, H., Dorman, C. E., Gilbert, K. M., Girardi, L., Gogarten, S. M., Gordon, K. D., Guhathakurta, P., Hodge, P. W., Holtzman, J. A., Johnson, L. C., Larsen, S. S., Lewis, A., Melbourne, J. L., Olsen, K. A. G., Rix, H.-W., Rosema, K., Saha, A., Sarajedini, A., Skillman, E. D., and Stanek, K. Z. (2012). The Panchromatic Hubble Andromeda Treasury. , 200:18.
- De Lucia, G., Fontanot, F., and Hirschmann, M. (2017). AGN feedback and the origin of the α enhancement in early-type galaxies - insights from the GAFA model. , 466(1):L88–L92.
- Dekel, A. and Burkert, A. (2014). Wet disc contraction to galactic blue nuggets and quenching to red nuggets. , 438(2):1870–1879.
- Elbaz, D., Dickinson, M., Hwang, H. S., Díaz-Santos, T., Magdis, G., Magnelli, B., Le Borgne, D., Galliano, F., Pannella, M., Chantal, P., Armus, L., Charmandaris, V., Daddi, E., Aussel, H., Popesso, P., Kartaltepe, J., Altieri, B., Valtchanov, I., Coia, D., Dannerbauer, H., Dasyra, K., Leiton, R., Mazzarella, J., Alexander, D. M., Buat, V., Burgarella, D., Chary, R.-R., Gilli, R., Ivison, R. J., Juneau, S., Le Floc'h, E., Lutz, D., Morrison, G. E., Mullaney, J. R., Murphy, E., Pope, A., Scott, D., Brodwin, M., Calzetti, D., Cesarsky, C., Charlot, S., Dole, H., Eisenhardt, P., Ferguson, H. C., Förster Schreiber, N., Frayer, D., Giavalisco, M., Huynh, M., Koekemoer, A. M., Papovich, C., Reddy, N., Surace, C., Teplitz, H., Yun, M. S., and Wilson, G. (2011). GOODS-Herschel: an infrared main sequence for star-forming galaxies. , 533:A119.
- Ellison, S. L., Sánchez, S. F., Ibarra-Medel, H., Antonio, B., Mendel, J. T., and Barrera-Ballesteros, J. (2018). Star formation is boosted (and quenched) from the inside-out: radial star formation profiles from MaNGA. , 474:2039–2054.

- Emami, N., Siana, B., Weisz, D. R., Johnson, B. D., Ma, X., and El-Badry, K. (2019). A Closer Look at Bursty Star Formation with $L_{H\alpha}$ and L_{UV} Distributions. , 881(1):71.
- Estrada-Carpenter, V., Papovich, C., Momcheva, I., Brammer, G., Simons, R., Bridge, J., Cleri, N. J., Ferguson, H., Finkelstein, S. L., Giavalisco, M., Jung, I., Matharu, J., Trump, J. R., and Weiner, B. (2020). CLEAR. II. Evidence for Early Formation of the Most Compact Quiescent Galaxies at High Redshift. , 898(2):171.
- Ferlet, R., Vidal-Madjar, A., and Gry, C. (1985). NA I as a tracer of H I in the diffuse interstellar medium. , 298:838–843.
- Foreman-Mackey, D., Hogg, D. W., Lang, D., and Goodman, J. (2013). emcee: The MCMC Hammer. , 125(925):306.
- Galametz, A., Grazian, A., Fontana, A., Ferguson, H. C., Ashby, M. L. N., Barro, G., Castellano, M., Dahlen, T., Donley, J. L., Faber, S. M., Grogin, N., Guo, Y., Huang, K.-H., Kocevski, D. D., Koekemoer, A. M., Lee, K.-S., McGrath, E. J., Peth, M., Willner, S. P., Almaini, O., Cooper, M., Cooray, A., Conselice, C. J., Dickinson, M., Dunlop, J. S., Fazio, G. G., Foucaud, S., Gardner, J. P., Giavalisco, M., Hathi, N. P., Hartley, W. G., Koo, D. C., Lai, K., de Mello, D. F., McLure, R. J., Lucas, R. A., Paris, D., Pentericci, L., Santini, P., Simpson, C., Sommariva, V., Targett, T., Weiner, B. J., Wuyts, S., and the CANDELS Team (2013). CANDELS Multiwavelength Catalogs: Source Identification and Photometry in the CANDELS UKIDSS Ultra-deep Survey Field. , 206:10.
- Gibson, B. K., Pilkington, K., Brook, C. B., Stinson, G. S., and Bailin, J. (2013). Constraining sub-grid physics with high-redshift spatially-resolved metallicity distributions. , 554:A47.
- Graves, G. J., Faber, S. M., and Schiavon, R. P. (2010). Dissecting the Red Sequence. IV. The Role of Truncation in the Two-dimensional Family of Early-type Galaxy Star Formation Histories. , 721(1):278–296.
- Green, J., Schechter, P., Baltay, C., Bean, R., Bennett, D., Brown, R., Conselice, C., Donahue, M., Fan, X., Gaudi, B. S., Hirata, C., Kalirai, J., Lauer, T., Nichol, B., Padmanabhan, N., Perlmutter, S., Rauscher, B., Rhodes, J., Roellig, T., Stern, D., Sumi, T., Tanner, A., Wang, Y., Weinberg, D., Wright, E., Gehrels, N., Sambruna, R., Traub, W., Anderson, J., Cook, K., Garnavich, P., Hillenbrand, L., Ivezić, Z., Kerins, E., Lunine, J., McDonald, P., Penny, M., Phillips, M., Rieke, G., Riess, A., van der Marel, R., Barry, R. K., Cheng, E., Content, D., Cutri, R., Goullioud, R., Grady, K., Helou, G., Jackson, C., Kruk, J., Melton, M., Peddie, C., Rioux, N., and Seiffert, M. (2012). Wide-Field InfraRed Survey Telescope (WFIRST) Final Report. *arXiv e-prints*, page arXiv:1208.4012.
- Greene, J. E., Janish, R., Ma, C.-P., McConnell, N. J., Blakeslee, J. P., Thomas, J., and Murphy, J. D. (2015). The MASSIVE Survey. II. Stellar Population Trends Out to Large Radius in Massive Early-type Galaxies. , 807(1):11.

- Greene, J. E., Veale, M., Ma, C.-P., Thomas, J., Quenneville, M. E., Blakeslee, J. P., Walsh, J. L., Goulding, A., and Ito, J. (2019). The MASSIVE Survey. XII. Connecting Stellar Populations of Early-type Galaxies to Kinematics and Environment. , 874(1):66.
- Grogin, N. A., Kocevski, D. D., Faber, S. M., Ferguson, H. C., Koekemoer, A. M., Riess, A. G., Acquaviva, V., Alexander, D. M., Almaini, O., Ashby, M. L. N., Barden, M., Bell, E. F., Bournaud, F., Brown, T. M., Caputi, K. I., Casertano, S., Cassata, P., Castellano, M., Challis, P., Chary, R.-R., Cheung, E., Cirasuolo, M., Conselice, C. J., Roshan Cooray, A., Croton, D. J., Daddi, E., Dahlen, T., Davé, R., de Mello, D. F., Dekel, A., Dickinson, M., Dolch, T., Donley, J. L., Dunlop, J. S., Dutton, A. A., Elbaz, D., Fazio, G. G., Filippenko, A. V., Finkelstein, S. L., Fontana, A., Gardner, J. P., Garnavich, P. M., Gawiser, E., Giavalisco, M., Grazian, A., Guo, Y., Hathi, N. P., Häussler, B., Hopkins, P. F., Huang, J.-S., Huang, K.-H., Jha, S. W., Kartaltepe, J. S., Kirshner, R. P., Koo, D. C., Lai, K., Lee, K.-S., Li, W., Lotz, J. M., Lucas, R. A., Madau, P., McCarthy, P. J., McGrath, E. J., McIntosh, D. H., McLure, R. J., Mobasher, B., Moustakas, L. A., Mozena, M., Nandra, K., Newman, J. A., Niemi, S.-M., Noeske, K. G., Papovich, C. J., Pentericci, L., Pope, A., Primack, J. R., Rajan, A., Ravindranath, S., Reddy, N. A., Renzini, A., Rix, H.-W., Robaina, A. R., Rodney, S. A., Rosario, D. J., Rosati, P., Salimbeni, S., Scarlata, C., Siana, B., Simard, L., Smidt, J., Somerville, R. S., Spinrad, H., Straughn, A. N., Strolger, L.-G., Telford, O., Teplitz, H. I., Trump, J. R., van der Wel, A., Villforth, C., Wechsler, R. H., Weiner, B. J., Wiklind, T., Wild, V., Wilson, G., Wuyts, S., Yan, H.-J., and Yun, M. S. (2011). CANDELS: The Cosmic Assembly Near-infrared Deep Extragalactic Legacy Survey. , 197:35.
- Guo, Y., Ferguson, H. C., Giavalisco, M., Barro, G., Willner, S. P., Ashby, M. L. N., Dahlen, T., Donley, J. L., Faber, S. M., Fontana, A., Galametz, A., Grazian, A., Huang, K.-H., Kocevski, D. D., Koekemoer, A. M., Koo, D. C., McGrath, E. J., Peth, M., Salvato, M., Wuyts, S., Castellano, M., Cooray, A. R., Dickinson, M. E., Dunlop, J. S., Fazio, G. G., Gardner, J. P., Gawiser, E., Grogin, N. A., Hathi, N. P., Hsu, L.-T., Lee, K.-S., Lucas, R. A., Mobasher, B., Nandra, K., Newman, J. A., and van der Wel, A. (2013). CANDELS Multi-wavelength Catalogs: Source Detection and Photometry in the GOODS-South Field. , 207:24.
- Guo, Y., Rafelski, M., Bell, E. F., Conselice, C. J., Dekel, A., Faber, S. M., Giavalisco, M., Koekemoer, A. M., Koo, D. C., Lu, Y., Mandelker, N., Primack, J. R., Ceverino, D., de Mello, D. F., Ferguson, H. C., Hathi, N., Kocevski, D., Lucas, R. A., Pérez-González, P. G., Ravindranath, S., Soto, E., Straughn, A., and Wang, W. (2018). Clumpy Galaxies in CANDELS. II. Physical Properties of UV-bright Clumps at $0.5 \leq z < 3$. , 853 : 108.
- Hemmati, S., Miller, S. H., Mobasher, B., Nayyeri, H., Ferguson, H. C., Guo, Y., Koekemoer, A. M., Koo, D. C., and Papovich, C. (2014). Kiloparsec-scale Properties of Emission-line Galaxies. , 797:108.
- Hemmati, S., Mobasher, B., Darvish, B., Nayyeri, H., Sobral, D., and Miller, S. (2015). Nebular and Stellar Dust Extinction Across the Disk of Emission-line Galaxies on Kiloparsec Scales. , 814:46.
- Herenz, E. C., Urrutia, T., Wisotzki, L., Kerutt, J., Saust, R., Werhahn, M., Schmidt, K. B., Caruana, J., Diener, C., Bacon, R., Brinchmann, J., Schaye, J., Maseda, M., and Weilbacher, P. M. (2017). The MUSE-Wide survey: A first catalogue of 831 emission line

- galaxies. , 606:A12.
- Hodge, J. A., Carilli, C. L., Walter, F., de Blok, W. J. G., Riechers, D., Daddi, E., and Lentati, L. (2012). Evidence for a Clumpy, Rotating Gas Disk in a Submillimeter Galaxy at $z = 4$. , 760(1):11.
- Ilbert, O., Arnouts, S., McCracken, H. J., Bolzonella, M., Bertin, E., Le Fèvre, O., Mellier, Y., Zamorani, G., Pellò, R., Iovino, A., Tresse, L., Le Brun, V., Bottini, D., Garilli, B., Maccagni, D., Picat, J. P., Scaramella, R., Scoddeggio, M., Vettolani, G., Zanichelli, A., Adami, C., Bardelli, S., Cappi, A., Charlot, S., Ciliegi, P., Contini, T., Cucciati, O., Foucaud, S., Franzetti, P., Gavignaud, I., Guzzo, L., Marano, B., Marinoni, C., Mazure, A., Meneux, B., Merighi, R., Paltani, S., Pollo, A., Pozzetti, L., Radovich, M., Zucca, E., Bondi, M., Bongiorno, A., Busarello, G., de La Torre, S., Gregorini, L., Lamareille, F., Mathez, G., Merluzzi, P., Ripepi, V., Rizzo, D., and Vergani, D. (2006). Accurate photometric redshifts for the CFHT legacy survey calibrated using the VIMOS VLT deep survey. , 457:841–856.
- Jafariyazani, M., Mobasher, B., Hemmati, S., Fetherolf, T., Khostovan, A. A., and Chartab, N. (2019). Spatially Resolved Properties of Galaxies from CANDELS+MUSE: Radial Extinction Profile and Insights on Quenching. , 887(2):204.
- Jafariyazani, M., Newman, A. B., Mobasher, B., Belli, S., Ellis, R. S., and Patel, S. G. (2020). Resolved Multi-element Stellar Chemical Abundances in the Brightest Quiescent Galaxy at $z \sim 2$. , 897(2):L42.
- Jiménez-Andrade, E. F., Zavala, J. A., Magnelli, B., Casey, C. M., Liu, D., Romano-Díaz, E., Schinnerer, E., Harrington, K., Aretxaga, I., Karim, A., Staguhn, J., Burnham, A. D., Montaña, A., Smolčić, V., Yun, M., Bertoldi, F., and Hughes, D. (2020). The Redshift and Star Formation Mode of AzTEC2: A Pair of Massive Galaxies at $z = 4.63$. , 890(2):171.
- Johansson, J., Thomas, D., and Maraston, C. (2012). Chemical element ratios of Sloan Digital Sky Survey early-type galaxies. , 421(3):1908–1926.
- Johnson, B. D., Leja, J., Conroy, C., and Speagle, J. S. (2021). Stellar Population Inference with Prospector. , 254(2):22.
- Johnson, B. D., Leja, J. L., Conroy, C., and Speagle, J. S. (2019). Prospector: Stellar population inference from spectra and SEDs.
- Kennicutt, Jr., R. C. (1998). Star formation in galaxies along the Hubble sequence. *Ann. Rev. Astron. Astrophys.*, 36:189–231.
- Kennicutt, Jr., R. C. (1998). Star Formation in Galaxies Along the Hubble Sequence. , 36:189–232.

- Koekemoer, A. M., Faber, S. M., Ferguson, H. C., Grogin, N. A., Kocevski, D. D., Koo, D. C., Lai, K., Lotz, J. M., Lucas, R. A., McGrath, E. J., Ogaz, S., Rajan, A., Riess, A. G., Rodney, S. A., Strolger, L., Casertano, S., Castellano, M., Dahlen, T., Dickinson, M., Dolch, T., Fontana, A., Giavalisco, M., Grazian, A., Guo, Y., Hathi, N. P., Huang, K.-H., van der Wel, A., Yan, H.-J., Acquaviva, V., Alexander, D. M., Almaini, O., Ashby, M. L. N., Barden, M., Bell, E. F., Bournaud, F., Brown, T. M., Caputi, K. I., Cassata, P., Challis, P. J., Chary, R.-R., Cheung, E., Cirasuolo, M., Conselice, C. J., Roshan Cooray, A., Croton, D. J., Daddi, E., Davé, R., de Mello, D. F., de Ravel, L., Dekel, A., Donley, J. L., Dunlop, J. S., Dutton, A. A., Elbaz, D., Fazio, G. G., Filippenko, A. V., Finkelstein, S. L., Frazer, C., Gardner, J. P., Garnavich, P. M., Gawiser, E., Gruetzbauch, R., Hartley, W. G., Häussler, B., Herrington, J., Hopkins, P. F., Huang, J.-S., Jha, S. W., Johnson, A., Kartaltepe, J. S., Khostovan, A. A., Kirshner, R. P., Lani, C., Lee, K.-S., Li, W., Madau, P., McCarthy, P. J., McIntosh, D. H., McLure, R. J., McPartland, C., Mobasher, B., Moreira, H., Mortlock, A., Moustakas, L. A., Mozena, M., Nandra, K., Newman, J. A., Nielsen, J. L., Niemi, S., Noeske, K. G., Papovich, C. J., Pentericci, L., Pope, A., Primack, J. R., Ravindranath, S., Reddy, N. A., Renzini, A., Rix, H.-W., Robaina, A. R., Rosario, D. J., Rosati, P., Salimbeni, S., Scarlata, C., Siana, B., Simard, L., Smidt, J., Snyder, D., Somerville, R. S., Spinrad, H., Straughn, A. N., Telford, O., Teplitz, H. I., Trump, J. R., Vargas, C., Villforth, C., Wagner, C. R., Wandro, P., Wechsler, R. H., Weiner, B. J., Wiklind, T., Wild, V., Wilson, G., Wuyts, S., and Yun, M. S. (2011). CANDELS: The Cosmic Assembly Near-infrared Deep Extragalactic Legacy Survey The Hubble Space Telescope Observations, Imaging Data Products, and Mosaics. , 197:36.
- Koyama, Y., Shimakawa, R., Yamamura, I., Kodama, T., and Hayashi, M. (2019). On the different levels of dust attenuation to nebular and stellar light in star-forming galaxies. , 71:8.
- Kriek, M. and Conroy, C. (2013). The Dust Attenuation Law in Distant Galaxies: Evidence for Variation with Spectral Type. , 775(1):L16.
- Kriek, M., Conroy, C., van Dokkum, P. G., Shapley, A. E., Choi, J., Reddy, N. A., Siana, B., van de Voort, F., Coil, A. L., and Mobasher, B. (2016). A massive, quiescent, population II galaxy at a redshift of 2.1. , 540(7632):248–251.
- Kriek, M., Price, S. H., Conroy, C., Suess, K. A., Mowla, L., Pasha, I., Bezanson, R., van Dokkum, P., and Barro, G. (2019). Stellar Metallicities and Elemental Abundance Ratios of $z \sim 1.4$ Massive Quiescent Galaxies. , 880(2):L31.
- Kroupa, P. (2001). On the variation of the initial mass function. , 322(2):231–246.
- Laureijs, R., Amiaux, J., Arduini, S., Auguères, J. L., Brinchmann, J., Cole, R., Cropper, M., Dabin, C., Duvet, L., Ealet, A., Garilli, B., Gondoin, P., Guzzo, L., Hoar, J., Hoekstra, H., Holmes, R., Kitching, T., Maciaszek, T., Mellier, Y., Pasian, F., Percival, W., Rhodes, J., Saavedra Criado, G., Sauvage, M., Scaramella, R., Valenziano, L., Warren, S., Bender, R., Castander, F., Cimatti, A., Le Fèvre, O., Kurki-Suonio, H., Levi, M., Lilje, P., Meylan, G., Nichol, R., Pedersen, K., Popa, V., Rebolo Lopez, R., Rix, H. W., Rottgering, H., Zeilinger, W., Grupp, F., Hudelot, P., Massey, R., Meneghetti, M., Miller, L., Paltani, S., Paulin-Henriksson, S., Pires, S., Saxton, C., Schrabback, T., Seidel, G., Walsh, J., Aghanim, N., Amendola, L., Bartlett, J., Baccigalupi, C., Beaulieu, J. P., Benabed, K., Cuby, J. G., Elbaz, D., Fosalba, P., Gavazzi, G., Helmi, A., Hook,

- I., Irwin, M., Kneib, J. P., Kunz, M., Mannucci, F., Moscardini, L., Tao, C., Teyssier, R., Weller, J., Zamorani, G., Zapatero Osorio, M. R., Boulade, O., Foumond, J. J., Di Giorgio, A., Guttridge, P., James, A., Kemp, M., Martignac, J., Spencer, A., Walton, D., Blümchen, T., Bonoli, C., Bortoletto, F., Cerna, C., Corcione, L., Fabron, C., Jahnke, K., Ligorì, S., Madrid, F., Martin, L., Morgante, G., Pamplona, T., Prieto, E., Riva, M., Toledo, R., Trifoglio, M., Zerbi, F., Abdalla, F., Douspis, M., Grenet, C., Borgani, S., Bouwens, R., Courbin, F., Delouis, J. M., Dubath, P., Fontana, A., Frailis, M., Grazian, A., Koppenhöfer, J., Mansutti, O., Melchior, M., Mignoli, M., Mohr, J., Neissner, C., Noddle, K., Poncet, M., Scodreggio, M., Serrano, S., Shane, N., Starck, J. L., Surace, C., Taylor, A., Verdoes-Kleijn, G., Vuerli, C., Williams, O. R., Zacchei, A., Altieri, B., Escudero Sanz, I., Kohley, R., Oosterbroek, T., Astier, P., Bacon, D., Bardelli, S., Baugh, C., Bellagamba, F., Benoist, C., Bianchi, D., Biviano, A., Branchini, E., Carbone, C., Cardone, V., Clements, D., Colombi, S., Conselice, C., Cresci, G., Deacon, N., Dunlop, J., Fedeli, C., Fontanot, F., Franzetti, P., Giocoli, C., Garcia-Bellido, J., Gow, J., Heavens, A., Hewett, P., Heymans, C., Holland, A., Huang, Z., Ilbert, O., Joachimi, B., Jennins, E., Kerins, E., Kiessling, A., Kirk, D., Kotak, R., Krause, O., Lahav, O., van Leeuwen, F., Lesgourgues, J., Lombardi, M., Magliocchetti, M., Maguire, K., Majerotto, E., Maoli, R., Marulli, F., Maurogordato, S., McCracken, H., McLure, R., Melchiorri, A., Merson, A., Moresco, M., Nonino, M., Norberg, P., Peacock, J., Pello, R., Penny, M., Pettorino, V., Di Porto, C., Pozzetti, L., Quercellini, C., Radovich, M., Rassat, A., Roche, N., Ronayette, S., Rossetti, E., Sartoris, B., Schneider, P., Semboloni, E., Serjeant, S., Simpson, F., Skordis, C., Smadja, G., Smartt, S., Spano, P., Spiro, S., Sullivan, M., Tilquin, A., Trotta, R., Verde, L., Wang, Y., Williger, G., Zhao, G., Zoubian, J., and Zucca, E. (2011). Euclid Definition Study Report. *arXiv e-prints*, page arXiv:1110.3193.
- Lee, N., Sanders, D. B., Casey, C. M., Toft, S., Scoville, N. Z., Hung, C.-L., Le Floch, E., Ilbert, O., Zahid, H. J., Aussel, H., Capak, P., Kartaltepe, J. S., Kewley, L. J., Li, Y., Schawinski, K., Sheth, K., and Xiao, Q. (2015). A Turnover in the Galaxy Main Sequence of Star Formation at $M_* \sim 10^{10} M_\odot$ for Redshifts $z \sim 1.3$. , 801:80.
- Leethochawalit, N., Jones, T. A., Ellis, R. S., Stark, D. P., Richard, J., Zitrin, A., and Auger, M. (2016). A Keck Adaptive Optics Survey of a Representative Sample of Gravitationally Lensed Star-forming Galaxies: High Spatial Resolution Studies of Kinematics and Metallicity Gradients. , 820(2):84.
- Leja, J., Carnall, A. C., Johnson, B. D., Conroy, C., and Speagle, J. S. (2019). How to Measure Galaxy Star Formation Histories. II. Nonparametric Models. , 876(1):3.
- Leja, J., Johnson, B. D., Conroy, C., van Dokkum, P. G., and Byler, N. (2017). Deriving Physical Properties from Broadband Photometry with Prospector: Description of the Model and a Demonstration of its Accuracy Using 129 Galaxies in the Local Universe. , 837:170.
- Liu, F. S., Jia, M., Yesuf, H. M., Faber, S. M., Koo, D. C., Guo, Y., Bell, E. F., Jiang, D., Wang, W., and Koekemoer, A. M. (2018). On the Transition of the Galaxy Quenching Mode at $0.5 < z < 1$ in CANDELS. , 860(1):60.
- Lonoce, I., Longhetti, M., Maraston, C., Thomas, D., Mancini, C., Cimatti, A., Ciocca, F., Citro, A., Daddi, E., di Serego Alighieri, S., Gargiulo, A., Maiolino, R., Mannucci, F., Moresco, M., Pozzetti, L., Quai, S., and Saracco, P. (2015). Old age and supersolar

- metallicity in a massive $z \approx 1.4$ early-type galaxy from VLT/X-Shooter spectroscopy. , 454(4):3912–3919.
- Lonoce, I., Maraston, C., Thomas, D., Longhetti, M., Parikh, T., Guarnieri, P., and Comparat, J. (2020). Stellar population properties of individual massive early-type galaxies at $1.4 < z < 2$. , 492(1):326–351.
- Ma, C.-P., Greene, J. E., McConnell, N., Janish, R., Blakeslee, J. P., Thomas, J., and Murphy, J. D. (2014). The MASSIVE Survey. I. A Volume-limited Integral-field Spectroscopic Study of the Most Massive Early-type Galaxies within 108 Mpc. , 795(2):158.
- Ma, X., Hopkins, P. F., Feldmann, R., Torrey, P., Faucher-Giguère, C.-A., and Kereš, D. (2017). Why do high-redshift galaxies show diverse gas-phase metallicity gradients? , 466(4):4780–4794.
- Madau, P. and Dickinson, M. (2014). Cosmic Star-Formation History. , 52:415–486.
- McLean, I. S., Steidel, C. C., Epps, H., Matthews, K., Adkins, S., Konidaris, N., Weber, B., Aliado, T., Brims, G., Canfield, J., Cromer, J., Fucik, J., Kulas, K., Mace, G., Magnone, K., Rodriguez, H., Wang, E., and Weiss, J. (2010). *Design and development of MOSFIRE: the multi-object spectrometer for infrared exploration at the Keck Observatory*, volume 7735 of *Society of Photo-Optical Instrumentation Engineers (SPIE) Conference Series*, page 77351E.
- McLean, I. S., Steidel, C. C., Epps, H. W., Konidaris, N., Matthews, K. Y., Adkins, S., Aliado, T., Brims, G., Canfield, J. M., Cromer, J. L., Fucik, J., Kulas, K., Mace, G., Magnone, K., Rodriguez, H., Rudie, G., Trainor, R., Wang, E., Weber, B., and Weiss, J. (2012). *MOSFIRE, the multi-object spectrometer for infra-red exploration at the Keck Observatory*, volume 8446 of *Society of Photo-Optical Instrumentation Engineers (SPIE) Conference Series*, page 84460J.
- Mobasher, B., Dahlen, T., Ferguson, H. C., Acquaviva, V., Barro, G., Finkelstein, S. L., Fontana, A., Gruetzbauch, R., Johnson, S., Lu, Y., Papovich, C. J., Pforr, J., Salvato, M., Somerville, R. S., Wiklind, T., Wuyts, S., Ashby, M. L. N., Bell, E., Conselice, C. J., Dickinson, M. E., Faber, S. M., Fazio, G., Finlator, K., Galametz, A., Gawiser, E., Giavalisco, M., Grazian, A., Grogin, N. A., Guo, Y., Hathi, N., Kocevski, D., Koekemoer, A. M., Koo, D. C., Newman, J. A., Reddy, N., Santini, P., and Wechsler, R. H. (2015). A Critical Assessment of Stellar Mass Measurement Methods. , 808:101.
- Morton, D. C. (1991). Atomic Data for Resonance Absorption Lines. I. Wavelengths Longward of the Lyman Limit. , 77:119.
- Nayyeri, H., Hemmati, S., Mobasher, B., Ferguson, H. C., Cooray, A., Barro, G., Faber, S. M., Dickinson, M., Koekemoer, A. M., Peth, M., Salvato, M., Ashby, M. L. N., Darvish, B., Donley, J., Durbin, M., Finkelstein, S., Fontana, A., Grogin, N. A., Gruetzbauch, R., Huang, K., Khostovan, A. A., Kocevski, D., Kodra, D., Lee, B., Newman, J., Pacifici, C., Pforr, J., Stefanon, M., Wiklind, T., Willner, S. P., Wuyts, S., Castellano, M., Conselice,

- C., Dolch, T., Dunlop, J. S., Galametz, A., Hathi, N. P., Lucas, R. A., and Yan, H. (2017). CANDELS Multi-wavelength Catalogs: Source Identification and Photometry in the CANDELS COSMOS Survey Field. , 228:7.
- Nelson, E. J., van Dokkum, P. G., Förster Schreiber, N. M., Franx, M., Brammer, G. B., Momcheva, I. G., Wuyts, S., Whitaker, K. E., Skelton, R. E., and Fumagalli, M. (2016). Where Stars Form: Inside-out Growth and Coherent Star Formation from HST H α Maps of 3200 Galaxies across the Main Sequence at 0.7 z 1.5. , 828(1):27.
- Nelson, E. J., van Dokkum, P. G., Momcheva, I. G., Brammer, G. B., Wuyts, S., Franx, M., Schreiber, N. M. F., Whitaker, K. E., and Skelton, R. E. (2016). Spatially resolved dust maps from balmer decrements in galaxies at $z \sim 1.4$. *The Astrophysical Journal Letters*, 817(1):L9.
- Newman, A. B., Belli, S., Ellis, R. S., and Patel, S. G. (2018a). Resolving Quiescent Galaxies at $z \sim 2$. I. Search for Gravitationally Lensed Sources and Characterization of Their Structure, Stellar Populations, and Line Emission. , 862(2):125.
- Newman, A. B., Belli, S., Ellis, R. S., and Patel, S. G. (2018b). Resolving Quiescent Galaxies at $z \sim 2$. II. Direct Measures of Rotational Support. , 862(2):126.
- Noeske, K. G., Weiner, B. J., Faber, S. M., Papovich, C., Koo, D. C., Somerville, R. S., Bundy, K., Conselice, C. J., Newman, J. A., Schiminovich, D., Le Floch, E., Coil, A. L., Rieke, G. H., Lotz, J. M., Primack, J. R., Barmby, P., Cooper, M. C., Davis, M., Ellis, R. S., Fazio, G. G., Guhathakurta, P., Huang, J., Kassin, S. A., Martin, D. C., Phillips, A. C., Rich, R. M., Small, T. A., Willmer, C. N. A., and Wilson, G. (2007). Star Formation in AEGIS Field Galaxies since $z=1.1$: The Dominance of Gradually Declining Star Formation, and the Main Sequence of Star-forming Galaxies. , 660:L43–L46.
- Okamoto, T., Nagashima, M., Lacey, C. G., and Frenk, C. S. (2017). The metal enrichment of passive galaxies in cosmological simulations of galaxy formation. , 464(4):4866–4874.
- Onodera, M., Carollo, C. M., Renzini, A., Cappellari, M., Mancini, C., Arimoto, N., Daddi, E., Gobat, R., Strazzullo, V., Tacchella, S., and Yamada, Y. (2015). The Ages, Metallicities, and Element Abundance Ratios of Massive Quenched Galaxies at $z \geq 1.6$. , 808(2):161.
- Osterbrock, D. E. (1989). *Astrophysics of gaseous nebulae and active galactic nuclei*.
- Pacifici, C., Kassin, S. A., Weiner, B. J., Holden, B., Gardner, J. P., Faber, S. M., Ferguson, H. C., Koo, D. C., Primack, J. R., Bell, E. F., Dekel, A., Gawiser, E., Giavalisco, M., Rafelski, M., Simons, R. C., Barro, G., Croton, D. J., Davé, R., Fontana, A., Grogin, N. A., Koekemoer, A. M., Lee, S.-K., Salmon, B., Somerville, R., and Behroozi, P. (2016). The Evolution of Star Formation Histories of Quiescent Galaxies. , 832(1):79.

- Patel, S. G., van Dokkum, P. G., Franx, M., Quadri, R. F., Muzzin, A., Marchesini, D., Williams, R. J., Holden, B. P., and Stefanon, M. (2013). HST/WFC3 Confirmation of the Inside-out Growth of Massive Galaxies at $0 < z < 2$ and Identification of Their Star-forming Progenitors at $z \sim 3$. , 766(1):15.
- Peng, Y.-j., Lilly, S. J., Kovač, K., Bolzonella, M., Pozzetti, L., Renzini, A., Zamorani, G., Ilbert, O., Knobel, C., Iovino, A., Maier, C., Cucciati, O., Tasca, L., Carollo, C. M., Silverman, J., Kampczyk, P., de Ravel, L., Sanders, D., Scoville, N., Contini, T., Mainieri, V., Scodreggio, M., Kneib, J.-P., Le Fèvre, O., Bardelli, S., Bongiorno, A., Caputi, K., Coppa, G., de la Torre, S., Franzetti, P., Garilli, B., Lamareille, F., Le Borgne, J.-F., Le Brun, V., Mignoli, M., Perez Montero, E., Pello, R., Ricciardelli, E., Tanaka, M., Tresse, L., Vergani, D., Welikala, N., Zucca, E., Oesch, P., Abbas, U., Barnes, L., Bordoloi, R., Bottini, D., Cappi, A., Cassata, P., Cimatti, A., Fumana, M., Hasinger, G., Koekemoer, A., Leauthaud, A., Maccagni, D., Marinoni, C., McCracken, H., Memeo, P., Meneux, B., Nair, P., Porciani, C., Presotto, V., and Scaramella, R. (2010). Mass and Environment as Drivers of Galaxy Evolution in SDSS and zCOSMOS and the Origin of the Schechter Function. , 721:193–221.
- Pickles, A. J. (1998). A stellar spectral flux library: 1150–25000 Å. *Publications of the Astronomical Society of the Pacific*, 110(749):863.
- Pilkington, K., Gibson, B. K., Brook, C. B., Calura, F., Stinson, G. S., Thacker, R. J., Michel-Dansac, L., Bailin, J., Couchman, H. M. P., Wadsley, J., Quinn, T. R., and Maccio, A. (2012). The distribution of metals in cosmological hydrodynamical simulations of dwarf disc galaxies. , 425(2):969–978.
- Raveri, M. and Hu, W. (2019). Concordance and discordance in cosmology. , 99(4):043506.
- Reddy, N. A., Erb, D. K., Pettini, M., Steidel, C. C., and Shapley, A. E. (2010). Dust Obscuration and Metallicity at High Redshift: New Inferences from UV, H α , and 8 μ m Observations of $z \sim 2$ Star-forming Galaxies. , 712:1070–1091.
- Reddy, N. A., Kriek, M., Shapley, A. E., Freeman, W. R., Siana, B., Coil, A. L., Mobasher, B., Price, S. H., Sanders, R. L., and Shivaiei, I. (2015). The MOSDEF Survey: Measurements of Balmer Decrements and the Dust Attenuation Curve at Redshifts $z \sim 1.4$ -2.6. , 806:259.
- Renzini, A. and Peng, Y.-j. (2015). An Objective Definition for the Main Sequence of Star-forming Galaxies. , 801:L29.
- Romano, D., Matteucci, F., Zhang, Z.-Y., Ivison, R. J., and Ventura, P. (2019). The evolution of CNO isotopes: the impact of massive stellar rotators. , 490(2):2838–2854.
- Salpeter, E. E. (1955). The Luminosity Function and Stellar Evolution. , 121:161.
- Sánchez, S. F., Kennicutt, R. C., Gil de Paz, A., van de Ven, G., Vílchez, J. M., Wisotzki,

- L., Walcher, C. J., Mast, D., Aguerri, J. A. L., Albiol-Pérez, S., Alonso-Herrero, A., Alves, J., Bakos, J., Bartáková, T., Bland-Hawthorn, J., Boselli, A., Bomans, D. J., Castillo-Morales, A., Cortijo-Ferrero, C., de Lorenzo-Cáceres, A., Del Olmo, A., Dettmar, R. J., Díaz, A., Ellis, S., Falcón-Barroso, J., Flores, H., Gallazzi, A., García-Lorenzo, B., González Delgado, R., Gruel, N., Haines, T., Hao, C., Husemann, B., Iglésias-Páramo, J., Jahnke, K., Johnson, B., Jungwiert, B., Kalinova, V., Kehrig, C., Kupko, D., López-Sánchez, Á. R., Lyubenova, M., Marino, R. A., Marmol-Queraltó, E., Márquez, I., Masegosa, J., Meidt, S., Mendez-Abreu, J., Monreal-Ibero, A., Montijo, C., Mourão, A. M., Palacios-Navarro, G., Papaderos, P., Pasquali, A., Peletier, R., Pérez, E., Pérez, I., Quirrenbach, A., Relaño, M., Rosales-Ortega, F. F., Roth, M. M., Ruiz-Lara, T., Sánchez-Blázquez, P., Sengupta, C., Singh, R., Stanishhev, V., Trager, S. C., Vazdekis, A., Viironen, K., Wild, V., Zibetti, S., and Ziegler, B. (2012). CALIFA, the Calar Alto Legacy Integral Field Area survey. I. Survey presentation. , 538:A8.
- Sánchez-Blázquez, P., Peletier, R. F., Jiménez-Vicente, J., Cardiel, N., Cenarro, A. J., Falcón-Barroso, J., Gorgas, J., Selam, S., and Vazdekis, A. (2006). Medium-resolution Isaac Newton Telescope library of empirical spectra. , 371(2):703–718.
- Sánchez-Menguiano, L., Sánchez, S. F., Pérez, I., García-Benito, R., Husemann, B., Mast, D., Mendoza, A., Ruiz-Lara, T., Ascasibar, Y., Bland-Hawthorn, J., Cavichia, O., Díaz, A. I., Florido, E., Galbany, L., González Delgado, R. M., Kehrig, C., Marino, R. A., Márquez, I., Masegosa, J., Méndez-Abreu, J., Mollá, M., Del Olmo, A., Pérez, E., Sánchez-Blázquez, P., Stanishhev, V., Walcher, C. J., López-Sánchez, Á. R., and Califa Collaboration (2016). Shape of the oxygen abundance profiles in CALIFA face-on spiral galaxies. , 587:A70.
- Sánchez-Menguiano, L., Sánchez, S. F., Pérez, I., Ruiz-Lara, T., Galbany, L., Anderson, J. P., Krühler, T., Kuncharayakti, H., and Lyman, J. D. (2018). The shape of oxygen abundance profiles explored with MUSE: evidence for widespread deviations from single gradients. , 609:A119.
- Scott, N., van de Sande, J., Croom, S. M., Groves, B., Owers, M. S., Poetrodjojo, H., D’Eugenio, F., Medling, A. M., Barat, D., Barone, T. M., Bland-Hawthorn, J., Brough, S., Bryant, J., Cortese, L., Foster, C., Green, A. W., Oh, S., Colless, M., Drinkwater, M. J., Driver, S. P., Goodwin, M., Gunawardhana, M. L. P., Federrath, C., Harischandra, L., Jin, Y., Lawrence, J. S., Lorente, N. P., Mannering, E., O’Toole, S., Richards, S. N., Sanchez, S. F., Schaefer, A. L., Sealey, K., Sharp, R., Sweet, S. M., Taranu, D. S., and Varidel, M. (2018). The SAMI Galaxy Survey: Data Release Two with absorption-line physics value-added products. , 481:2299–2319.
- Shivaei, I., Kriek, M., Reddy, N. A., Shapley, A. E., Barro, G., Conroy, C., Coil, A. L., Freeman, W. R., Mobasher, B., Siana, B., Sanders, R., Price, S. H., Azadi, M., Pasha, I., and Inami, H. (2016). The MOSDEF Survey: The Strong Agreement between $H\alpha$ and UV-to-FIR Star Formation Rates for $z \sim 2$ Star-forming Galaxies. , 820(2):L23.
- Simcoe, R. A., Burgasser, A. J., Schechter, P. L., Fishner, J., Bernstein, R. A., Bigelow, B. C., Pipher, J. L., Forrest, W., McMurtry, C., Smith, M. J., and Bochanski, J. J. (2013). FIRE: A Facility Class Near-Infrared Echelle Spectrometer for the Magellan Telescopes. , 125(925):270.

- Smith, R. J., Lucey, J. R., Hudson, M. J., and Bridges, T. J. (2009). Abundance ratios in red-sequence galaxies over a wide mass range: the ‘X-planes’ for magnesium, calcium, carbon and nitrogen. , 398(1):119–132.
- Speagle, J. S. (2020). DYNESTY: a dynamic nested sampling package for estimating Bayesian posteriors and evidences. , 493(3):3132–3158.
- Speagle, J. S., Steinhardt, C. L., Capak, P. L., and Silverman, J. D. (2014). A Highly Consistent Framework for the Evolution of the Star-Forming “Main Sequence” from $z \sim 0-6$. , 214:15.
- Spitzer, L. (1978). *Physical processes in the interstellar medium*.
- Stefanon, M., Yan, H., Mobasher, B., Barro, G., Donley, J. L., Fontana, A., Hemmati, S., Koekemoer, A. M., Lee, B., Lee, S.-K., Nayyeri, H., Peth, M., Pforr, J., Salvato, M., Wiklind, T., Wuyts, S., Ashby, M. L. N., Castellano, M., Conselice, C. J., Cooper, M. C., Cooray, A. R., Dolch, T., Ferguson, H., Galametz, A., Giavalisco, M., Guo, Y., Willner, S. P., Dickinson, M. E., Faber, S. M., Fazio, G. G., Gardner, J. P., Gawiser, E., Grazian, A., Grogin, N. A., Kocevski, D., Koo, D. C., Lee, K.-S., Lucas, R. A., McGrath, E. J., Nandra, K., Newman, J. A., and van der Wel, A. (2017). CANDELS Multi-wavelength Catalogs: Source Identification and Photometry in the CANDELS Extended Groth Strip. , 229:32.
- Tacchella, S., Dekel, A., Carollo, C. M., Ceverino, D., DeGraf, C., Lapiner, S., Mandelker, N., and Primack, J. R. (2016). Evolution of density profiles in high- z galaxies: compaction and quenching inside-out. , 458(1):242–263.
- Thomas, D., Maraston, C., and Bender, R. (2003a). New clues on the calcium underabundance in early-type galaxies. , 343(1):279–283.
- Thomas, D., Maraston, C., and Bender, R. (2003b). Stellar population models of Lick indices with variable element abundance ratios. , 339(3):897–911.
- Thomas, D., Maraston, C., Bender, R., and Mendes de Oliveira, C. (2005). The Epochs of Early-Type Galaxy Formation as a Function of Environment. , 621(2):673–694.
- Toft, S., Smolčić, V., Magnelli, B., Karim, A., Zirm, A., Michalowski, M., Capak, P., Sheth, K., Schawinski, K., Krogager, J. K., Wuyts, S., Sanders, D., Man, A. W. S., Lutz, D., Staguhn, J., Berta, S., McCracken, H., Krpan, J., and Riechers, D. (2014). Submillimeter Galaxies as Progenitors of Compact Quiescent Galaxies. , 782(2):68.
- Toft, S., Zabl, J., Richard, J., Gallazzi, A., Zibetti, S., Prescott, M., Grillo, C., Man, A. W. S., Lee, N. Y., Gómez-Guijarro, C., Stockmann, M., Magdis, G., and Steinhardt, C. L. (2017). A massive, dead disk galaxy in the early Universe. , 546(7659):510–513.

- Trager, S. C., Faber, S. M., Worthey, G., and González, J. J. (2000a). The Stellar Population Histories of Early-Type Galaxies. II. Controlling Parameters of the Stellar Populations. , 120(1):165–188.
- Trager, S. C., Faber, S. M., Worthey, G., and González, J. J. (2000b). The Stellar Population Histories of Local Early-Type Galaxies. I. Population Parameters. , 119(4):1645–1676.
- Urrutia, T., Wisotzki, L., Kerutt, J., Schmidt, K. B., Herenz, E. C., Klar, J., Saust, R., Werhahn, M., Diener, C., Caruana, J., Krajnović, D., Bacon, R., Boogaard, L., Brinchmann, J., Enke, H., Maseda, M., Nanayakkara, T., Richard, J., Steinmetz, M., and Weilbacher, P. M. (2019a). The MUSE-Wide Survey: survey description and first data release. , 624:A141.
- Urrutia, T., Wisotzki, L., Kerutt, J., Schmidt, K. B., Herenz, E. C., Klar, J., Saust, R., Werhahn, M., Diener, C., Caruana, J., Krajnović, D., Bacon, R., Boogaard, L., Brinchmann, J., Enke, H., Maseda, M., Nanayakkara, T., Richard, J., Steinmetz, M., and Weilbacher, P. M. (2019b). The MUSE-Wide Survey: survey description and first data release. , 624:A141.
- Valentino, F., Tanaka, M., Davidzon, I., Toft, S., Gómez-Guijarro, C., Stockmann, M., Onodera, M., Brammer, G., Ceverino, D., Faisst, A. L., Gallazzi, A., Hayward, C. C., Ilbert, O., Kubo, M., Magdis, G. E., Selsing, J., Shimakawa, R., Sparre, M., Steinhardt, C., Yabe, K., and Zabl, J. (2020). Quiescent Galaxies 1.5 Billion Years after the Big Bang and Their Progenitors. , 889(2):93.
- Villaume, A., Conroy, C., Johnson, B., Rayner, J., Mann, A. W., and van Dokkum, P. (2017). The Extended IRTF Spectral Library: Expanded Coverage in Metallicity, Temperature, and Surface Gravity. , 230(2):23.
- Wild, V., Charlot, S., Brinchmann, J., Heckman, T., Vince, O., Pacifici, C., and Chevallard, J. (2011). Empirical determination of the shape of dust attenuation curves in star-forming galaxies. , 417:1760–1786.
- Woosley, S. E. and Weaver, T. A. (1995). The Evolution and Explosion of Massive Stars. II. Explosive Hydrodynamics and Nucleosynthesis. , 101:181.
- Worthey, G. (1998). Abundance Ratio Trends and Nucleosynthesis in Elliptical Galaxies and Spheroids. , 110(750):888–899.
- Wu, P.-F., van der Wel, A., Bezanson, R., Gallazzi, A., Pacifici, C., Straatman, C. M. S., Barišić, I., Bell, E. F., Chauke, P., D’Eugenio, F., Franx, M., Muzzin, A., Sobral, D., and van Houdt, J. (2020). The Colors and Sizes of Recently Quenched Galaxies: A Result of Compact Starburst before Quenching. , 888(2):77.
- Wuyts, S., Förster Schreiber, N. M., Genzel, R., Guo, Y., Barro, G., Bell, E. F., Dekel, A., Faber, S. M., Ferguson, H. C., Giavalisco, M., Grogin, N. A., Hathi, N. P., Huang,

- K.-H., Kocevski, D. D., Koekemoer, A. M., Koo, D. C., Lotz, J., Lutz, D., McGrath, E., Newman, J. A., Rosario, D., Saintonge, A., Tacconi, L. J., Weiner, B. J., and van der Wel, A. (2012a). Smooth(er) Stellar Mass Maps in CANDELS: Constraints on the Longevity of Clumps in High-redshift Star-forming Galaxies. , 753:114.
- Wuyts, S., Förster Schreiber, N. M., Genzel, R., Guo, Y., Barro, G., Bell, E. F., Dekel, A., Faber, S. M., Ferguson, H. C., Giavalisco, M., Grogin, N. A., Hathi, N. P., Huang, K.-H., Kocevski, D. D., Koekemoer, A. M., Koo, D. C., Lotz, J., Lutz, D., McGrath, E., Newman, J. A., Rosario, D., Saintonge, A., Tacconi, L. J., Weiner, B. J., and van der Wel, A. (2012b). Smooth(er) Stellar Mass Maps in CANDELS: Constraints on the Longevity of Clumps in High-redshift Star-forming Galaxies. , 753:114.
- Wuyts, S., Förster Schreiber, N. M., Nelson, E. J., van Dokkum, P. G., Brammer, G., Chang, Y.-Y., Faber, S. M., Ferguson, H. C., Franx, M., Fumagalli, M., Genzel, R., Grogin, N. A., Kocevski, D. D., Koekemoer, A. M., Lundgren, B., Lutz, D., McGrath, E. J., Momcheva, I., Rosario, D., Skelton, R. E., Tacconi, L. J., van der Wel, A., and Whitaker, K. E. (2013). A CANDELS-3D-HST synergy: Resolved Star Formation Patterns at $0.7 < z < 1.5$. , 779:135.
- Yan, Z., Jerabkova, T., and Kroupa, P. (2019). The star formation timescale of elliptical galaxies. Fitting [Mg/Fe] and total metallicity simultaneously. , 632:A110.
- Zhang, Z.-Y., Romano, D., Ivison, R. J., Papadopoulos, P. P., and Matteucci, F. (2018). Stellar populations dominated by massive stars in dusty starburst galaxies across cosmic time. , 558(7709):260–263.
- Zolotov, A., Dekel, A., Mandelker, N., Tweed, D., Inoue, S., DeGraf, C., Ceverino, D., Primack, J. R., Barro, G., and Faber, S. M. (2015). Compaction and quenching of high- z galaxies in cosmological simulations: blue and red nuggets. , 450(3):2327–2353.